Biophysical *Journal*
Article

Biophysical Society

Dynamics of the SARS-CoV-2 nucleoprotein N-terminal domain triggers RNA duplex destabilization

Ícaro P. Caruso,[1,2,*] Karoline Sanches,[1,2] Andrea T. Da Poian,[2] Anderson S. Pinheiro,[3] and Fabio C. L. Almeida[2,*]
[1]Multiuser Center for Biomolecular Innovation and Department of Physics, Institute of Biosciences, Letters and Exact Sciences, São Paulo State University (UNESP), São José do Rio Preto, São Paulo, Brazil; [2]Institute of Medical Biochemistry Leopoldo de Meis and National Center for Structural Biology and Bioimaging, Rio de Janeiro, Brazil; and [3]Department of Biochemistry, Institute of Chemistry, Federal University of Rio de Janeiro, Rio de Janeiro, Brazil

ABSTRACT The nucleocapsid (N) protein of betacoronaviruses is responsible for nucleocapsid assembly and other essential regulatory functions. The N protein N-terminal domain (N-NTD) interacts and melts the double-stranded transcriptional regulatory sequences (dsTRSs), regulating the discontinuous subgenome transcription process. Here, we used molecular dynamics (MD) simulations to study the binding of the severe acute respiratory syndrome coronavirus 2 N-NTD to nonspecific (NS) and TRS dsRNAs. We probed dsRNAs' Watson-Crick basepairing over 25 replicas of 100 ns MD simulations, showing that only one N-NTD of dimeric N is enough to destabilize dsRNAs, triggering melting initiation. dsRNA destabilization driven by N-NTD was more efficient for dsTRSs than dsNS. N-NTD dynamics, especially a tweezer-like motion of β2-β3 and Δ2-β5 loops, seems to play a key role in Watson-Crick basepairing destabilization. Based on experimental information available in the literature, we constructed kinetics models for N-NTD-mediated dsRNA melting. Our results support a 1:1 stoichiometry (N-NTD/dsRNA), matching MD simulations and raising different possibilities for N-NTD action: 1) two N-NTD arms of dimeric N would bind to two different RNA sites, either closely or spatially spaced in the viral genome, in a cooperative manner; and 2) monomeric N-NTD would be active, opening up the possibility of a regulatory dissociation event.

SIGNIFICANCE Coronaviruses display a unique discontinuous transcription mechanism, in which the N protein plays a major role. N-NTD promotes dsRNA melting, releasing the nascent negative strand via a poorly described mechanism. It specifically recognizes the body TRS, a conserved RNA motif located at the 5′-end of each open reading frame, catalyzing the melting of the RNA duplex and transferring of the nascent strand to the leader TRS. Here, we describe a counterintuitive mechanism of N-NTD-induced dsRNA destabilization based on MD simulation and kinetic modeling using the experimental data of its melting activity. These data impact directly in the understanding of the mechanism by which N protein acts in the cell, guiding future experiments.

INTRODUCTION

The recent pandemic of severe acute respiratory syndrome coronavirus 2 (SARS-CoV-2), the causative agent of coronavirus disease 2019, has become a global health emergency (1,2). SARS-CoV-2, a member of the Coronaviridae family, is an enveloped virus containing a large nonsegmented positive-sense single-stranded RNA genome (3,4). The 5′ two-thirds of the coronaviruses' genome, corresponding to open reading frame (ORF) 1a/b, is translated into two polyproteins (pp1a and pp1ab) that are proteolytically processed into 16 nonstructural proteins (5). These nonstructural proteins assemble in the viral replicase-transcriptase complex at the endoplasmic reticulum membrane, being responsible for genome replication and transcription (6). Conversely, the 3′ one-third of the genome is translated into accessory proteins as well as the four structural proteins—spike (S), membrane (M), envelope (E), and nucleocapsid (N)—through a unique process of subgenomic mRNA (sgmRNA) transcription (7,8).

N is one of the most abundant viral proteins in the infected cell. It is a 46 kDa multifunctional RNA-binding protein that packs the viral RNA in a helical nucleocapsid (9). In addition, N localizes at the replicase-transcriptase complex at early stages of infection and plays a central role in the regulation

Submitted December 25, 2020, and accepted for publication June 3, 2021.
*Correspondence: icaro.caruso@unesp.br or falmeida@bioqmed.ufrj.br
Editor: Chris Chipot.
https://doi.org/10.1016/j.bpj.2021.06.003

of RNA synthesis (10–12). It is composed of two functionally distinct folded domains, which are interspersed by an intrinsically disordered linker region enriched in arginine and serine residues. Both the two domains and the linker region contribute individually to RNA binding (13). The N protein N-terminal domain (N-NTD) has been shown to interact with regulatory RNA sequences during subgenome transcription, whereas its C-terminal domain is responsible for N protein dimerization, which is crucial for nucleocapsid assembly (14,15). The recently reported solution structure of SARS-CoV-2 N-NTD reveals a right hand-like fold, composed of a five-stranded central β-sheet flanked by two short α-helices, arranged in a $\beta4$-$\beta2$-$\beta3$-$\beta1$-$\beta5$ topology (16). The β-sheet core is referred to as the hand's palm, and the long $\beta2$-$\beta3$ hairpin, mostly composed of basic amino acid residues, corresponds to the basic finger. The positively charged cleft between the basic finger and the palm has been suggested as a putative RNA-binding site (16).

Genome replication is a continuous process in coronaviruses. In contrast, transcription is discontinuous and involves the production of sgmRNAs (17). Regulation of sgmRNA synthesis is dependent on transcriptional regulatory sequences (TRSs) located either at the 5′-end of the positive-strand RNA genome, known as the leader TRS (TRS-L), or at the 5′-end of each viral gene coding for structural and accessory proteins, called the body TRS (TRS-B). The TRS-L and TRS-B share a similar core sequence, which allows for a template switch during sgmRNA synthesis. Once the TRS-B has been copied, the nascent negative-strand RNA is transferred to the TRS-L, and transcription is terminated (17,18). Multiple well-orchestrated factors, including TRS secondary structure and RNA-RNA and RNA-protein interactions, influence sgmRNA transcription (17). Coronaviruses' N-NTD specifically interacts with the TRS and efficiently melts an RNA duplex formed between TRS and its complementary strand (cTRS), facilitating template switch and playing a pivotal role in the regulation of discontinuous transcription (10,16,17,19). Despite its relevance for the viral replication cycle, the molecular basis underlying the specificity of interaction of the SARS-CoV-2 N-NTD with the TRS remains elusive. Thus, understanding the mechanism by which SARS-CoV-2 N-NTD specifically recognizes TRS RNA at atomic detail is paramount for the rational development of new antiviral strategies.

Here, we present a hypothesis for the molecular mechanism by which SARS-CoV-2 N-NTD destabilizes double-stranded (ds) RNA, the initial step of the dsRNA melting process. We showed by molecular dynamics (MD) simulations (25 replicas of 100 ns) that N-NTD destabilizes dsRNA's Watson-Crick (WC) basepairing by decreasing the number of the RNA-RNA hydrogen bonds and perturbing the local rigid-body geometric parameters of dsRNA. The destabilization is more significant for TRS than for a nonspecific (NS) dsRNA sequence. Moreover, a tweezer-like motion between $\beta2$-$\beta3$ and $\Delta2$-$\beta5$ loops of N-NTD seems to be a key dynamic feature for selectivity and, consequently, dsRNA destabilization. We also constructed kinetic models for characterizing the melting activity of the dimeric N protein assuming 1:1 and 2:1 (N-NTD/dsRNA) stoichiometries, revealing that only one N-NTD is sufficient for dsRNA melting.

MATERIALS AND METHODS

Molecular docking

To perform the docking, we took advantage of experimental data previously published (16), in which SARS-CoV-2 N-NTD interaction with an NS dsRNA (5′-CACUGAC-3′ and 5′-GUCAGUG-3′) was monitored by chemical shift perturbation (CSP) titration experiments. Structural models for the N-NTD/dsNS complex were constructed using the HADDOCK server (version 2.2) (20). The coordinates used as input were obtained from the solution NMR structure of SARS-CoV-2 N-NTD (Protein Data Bank (PDB): 6YI3) (16), and the x-ray structure of a synthetic 7-mer dsRNA (PDB: 4U37) (21) mutated using the w3DNA server (version 2.0) (22) to generate the same NS dsRNA sequence as that used in the CSP titration experiments (5′-CACUGAC-3′ and 5′-GUCAGUG-3′). In addition, histidine protonation states at pH 7.0 were set according to the PROPKA server (23). In total, 2000 complex structures of rigid-body docking were calculated by using the standard HADDOCK protocol with an optimized potential for liquid simulation parameter (24). The final 200 lowest-energy structures were selected for subsequent explicit solvent (water) and semiflexible simulated annealing refinement (first step: 2000 K and 8 ps; second step: 1000 K and 16 ps; third step: 1000 K and 16 ps; and final solvated refinement step: 300 K and 2.5 ps), to optimize side chain constants. The final structures were clustered using the backbone root mean-square deviation (RMSD) with a cutoff of 7.5 Å (25).

Next, the structural model of the N-NTD/dsTRS (5′-UCUAAAC-3′ and 5′-AGAUUUG-3′; sense and antisense sequences) complex was generated from the lowest-energy structure of the N-NTD/dsNS complex, derived from the cluster with the lowest HADDOCK score, by mutating the dsRNA sequence using w3DNA (22). Therefore, both complexes have identical geometries, varying only the dsRNA sequence. Structural conformation of the constructed model for N-NTD/dsTRS complex was displayed using the web application http://skmatic.x3dna.org for easy creation of Dissecting the Spatial Structure of RNA-PyMOL schematics (26).

MD simulation

MD calculations for N-NTDs, dsRNAs, and N-NTD/dsRNA complexes were performed using GROMACS (version 5.0.7) (27). The molecular systems were modeled with the corrected AMBER14 package, including the ff14sb protein (28) and ff99bsc0χOL3 RNA (29) force fields, as well as the TIP3P water model (30). The ff99bsc0χOL3 force field parameterizes the glycosidic torsion angle χ of the AMBER package for RNA, removing the destabilization of the anti-configuration and preventing formation of the ladder-like structural distortions in RNA simulations (29). The structural models of N-NTD (PDB: 6YI3), dsRNAs (mutated PDB: 4U37), and N-NTD/dsRNA complexes (from molecular docking) were placed in the center of a cubic box solvated by a solution of 50 mM NaCl in water. The protonation state of ionizable residues at pH 7.0 was set according to the PROPKA server (23). Periodic boundary conditions were used, and all simulations were performed in an isothermal-isobaric (NPT) ensemble, keeping the system at 298 K and 1.0 bar using the Nosé-Hoover thermostat (τ_T = 2 ps) and Parrinello-Rahman barostat (τ_P = 2 ps and compressibility = 4.5×10^{-5} bar^{-1}). A cutoff of 12 Å for both Lennard-Jones and Coulomb potentials was used. The long-range electrostatic interactions were calculated using the particle mesh Ewald algorithm. In every MD simulation, a time step of 2.0 fs was used and all covalent bonds involving hydrogen atoms were constrained to their equilibrium distance.

A conjugate gradient minimization algorithm was used to relax the superposition of atoms generated in the box construction process. Energy minimizations were carried out with the steepest descent integrator and conjugate gradient algorithm, using 1000 kJ $mol^{-1} \cdot nm^{-1}$ as the maximal force criterion. 100,000 steps of MD were performed for each canonical (NVT) and NPT ensemble equilibration, applying force constants of 1000 kJ mol^{-1} nm^{-2} to all heavy atoms of N-NTD, dsRNAs, and N-NTD:dsRNA complexes. At the end of preparation, 25 replicas of 100 ns MD simulation of each molecular system with different seeds of the random number generator were carried out for data acquisition, totalizing 2.5 μs. All the MD simulations started from the same set of coordinates. Following dynamics, the trajectories of each molecular system were firstly concatenated individually and analyzed according to the RMSD, number of contacts, number of hydrogen bonds, and local basepair parameters of the dsRNAs. RMSDs were calculated for the backbone atoms of protein and nucleic acid. The number of contacts for distances lower than 0.6 nm were quantified between pairs of atoms of the N-NTD and dsRNAs. The occurrence of RNA-RNA, protein-nitrogenous base, and protein-RNA hydrogen bonds were calculated between the heavy atoms using a cutoff distance of 3.5 Å and maximal angle of 30°. The local basepair parameters (angles (°): buckle, opening, and propeller; distances (nm): stretch, stagger, and shear) for free and N-NTD-bound dsNSs and dsTRSs were determined by using the *do_x3dna* tool (31) along with the 3DNA package (32). These local basepair parameters of each of the 25 runs and of selected replicas were analyzed together as histogram plots exhibiting population distributions. The percentage of persistency of protein-RNA hydrogen bonds was obtained from the plot_hbmap_generic.pl script (33). The number of protein-RNA hydrogen bonds with a persistence higher than 10% was counted with respect to amino acid and nucleotide residues for each 25 replicas. After individual analysis of each simulation, the last 50 ns of the 25 trajectories of free and dsRNA-bound N-NTD were concatenated in single files, and these new trajectories were used to evaluate the root mean-square fluctuation (RMSF) of the C_α atoms and principal component analysis (PCA). PCA scatter plots were generated for free and dsRNA-bound N-NTDs, as well as conformational motions being filtered (30 frames) from the eigenvectors of the first and second principal components (PC1 and PC2, respectively). We also concatenated (pooled) the trajectories of all 25 replicas of the MD simulations of free N-NTD with its bound states (N-NTD/dsNS and N-NTD/dsTRS) and generated PCA scatter plots. The conformational space was quantified by fitting an elliptical shell with 95% (confidence) of the density for each scatter plot and making its extent proportional to the area (S_{el}) of this shell. This strategy guarantees that the same eigenvectors are used for all systems. The structural representations of the motions from PC1 and PC2 were prepared using PyMol (34).

Kinetic simulations

The Kinetiscope program (version 1.1.956.x6; http://hinsberg.net/kinetiscope/) was used to simulate the kinetics of dsRNA melting by the SARS-CoV-2 N-NTD. This software is based on a stochastic algorithm developed by Bunker et al. (35) and Gillespie (36). Simulations were performed under constant volume, pressure, and temperature (298.15 K). An initial concentration of 50 nM dsTRS was used, and a total of 2439 initial numbers of particles were calculated. N-NTD concentration ranged from 0 to 2 μM for model 1 and from 0 to 4.5 μM for model 2. The maximal number of events was set to 10 million, and simulations lasted for at least 100 s.

RESULTS

Structural models of the N-NTD/dsRNA complexes and their validation from MD simulations

In this work, we probed the dynamical behavior of SARS-CoV-2 N-NTD interaction with an NS and a biologically relevant RNA sequence (TRS). During discontinuous transcription, N-NTD acts on the TRS-B duplex, promoting its melting and delivering the nascent negative-strand RNA to the TRS-L (template switch). This template switch enables the transcription of subgenomic RNAs. To guide the selection of the TRS-specific sequence, we aligned the nucleotide sequences of TRS-Bs from each SARS-CoV-2 ORF (NCBI reference sequence: NC_045512.3) with the TRS-L sequence (Fig. S1). Remarkably, there is no consensus among the TRS-B sequences. Even the triple adenine motif, which was previously identified as essential for N-NTD binding, is not present in the TRS-Bs of ORF E and ORF6. The closest to a consensus sequence is the triple adenine flanked by pyrimidine residues. Thus, we chose the core sequence 5′-UCUAAAC-3′ (antisense 5′-AGAUUUG-3′) as representative of TRS, as it is identical among the TRS-Bs of ORFs N and M as well as TRS-L.

To choose the optimal size of the dsRNA and pursue the computational simulations, we considered the previous experimental data available for SARS-CoV-2 N-NTD and the mechanical properties of dsRNAs. The only experimentally validated structural information available for the N-NTD/dsRNA interaction was performed with the 7-mer NS oligonucleotide used in this work (16). Differently from DNA structure, which favors long stretches of the double helix, the most frequent RNA sequences occurring in nature exhibit short canonical helices, generally containing no more than 12 consecutive basepairs (37). A possible explanation for this structural feature may be related to the mechanical properties of dsRNA, which stretches ~3 times more than dsDNA under an external force, unwinding upon elongation, whereas DNA overwinds when stretched. Interestingly, the formation of tertiary RNA structures frequently involves contacts between canonical dsRNA helices (38). It is worth mentioning that dsRNA-binding domains are small, around 100 amino acids long, and thus, they specifically recognize short dsRNA segments (39,40). For the reasons above, we decided to perform the computational simulations with the experimentally supported 7-mer dsRNA.

We calculated the structural model of the N-NTD/dsTRS complex based on the experimental data for the N-NTD interaction with an NS dsRNA (5′-CACUGAC-3′ and 5′-GUCAGUG-3′; sense and antisense, dsNS) (16) using the HADDOCK 2.2 server (20). The structural restraints of the N-NTD/dsNS complex were defined from CSPs titration by NMR spectroscopy (16). The lowest-energy structure of the N-NTD/dsNS complex from the cluster with the lowest HADDOCK score (fraction of common contacts = 0.8 ± 0.1 Å, interface-RMSD = 1.0 ± 0.6 Å, and ligand-RMSD = 2.2 ± 1.2 Å) was used to mutate the dsNS molecule to obtain the TRS sequence (sense 5′-UCUAAAC-3′ and antisense 5′-AGAUUUG-3′) and, therefore, to generate the N-NTD/dsTRS complex structure. Fig. 1, *A and B* show the structural model of the N-NTD/dsTRS complex,

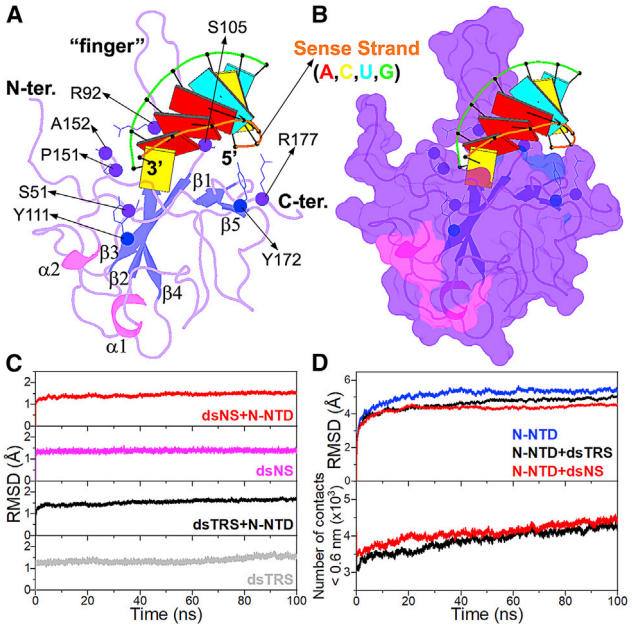

FIGURE 1 Structural model of the N-NTD/dsRNA complex and its validation from MD simulations. (*A*) Structural model of the N-NTD/dsTRS complex determined by molecular docking calculations and mutation of dsNS nucleotide sequence. N-NTD is presented as a cartoon, and dsTRS is denoted as a ribbon model with basepairing as colored rectangles. The color of the rectangles corresponds to the nitrogenous base of the dsRNA sense strand, namely A: red, C: yellow, U: cyan, and G: green. The large protruding $\beta2$-$\beta3$ loop is referred to as the finger. The residues involved in polar contacts with the dsTRS are presented as sphere (α-carbon) and lines (side chain). The α-helix and β-sheet secondary structures are colored in magenta and blue, respectively. (*B*) Surface representation of the structural model of the N-NTD/dsTRS complex. (*C*) Average RMSD values for dsNS and dsTRS in their free and N-NTD-bound states. (*D*) Average RMSD values for N-NTD in its free and dsRNA-bound state (*top*) and average number of contacts between N-NTD and dsRNA atoms (distance <0.6 nm) (*bottom*). The average values correspond to 25 MD simulations with the same starting point. To see this figure in color, go online.

in which the TRS RNA is inserted in a cleft located between the large protruding $\beta2$-$\beta3$ loop, named the finger, and the central β-sheet of N-NTD, referred to as the palm. The structural model also revealed that residues S51, R92, S105, Y111, P151, A152, Y172, and R177 are involved in polar contacts with the dsTRS (Fig. 1 *A*). Analysis of the electrostatic surface potential of N-NTD revealed that the dsRNA-binding pocket is positively charged, with the finger being the highest charged region (Fig. S2). This result is consistent with the charge complementarity of the nucleic acid phosphate groups that exhibit negative charge.

We performed 25 calculations of 100 ns MD simulations to investigate the stability of the structural models of N-NTD in complex with either a dsNS or dsTRS, as well as each of the biomolecules separately (dsNS, dsTRS, and N-NTD). Fig. 1 *C* shows the average RMSD values of the backbone atoms (C5′, C4′, C3′, O3′, P, and O5′) from the starting structure (refined HADDOCK model) for the dsNS and dsTRS in their free and N-NTD-bound states, which were significantly stable along the 100 ns MD simulations. Similar results are observed for the average RMSD values of the backbone atoms for free and dsRNA-bound N-NTD over the simulations (Fig. 1 *D*, *top*). Evaluation of the average number of contacts between N-NTD and dsRNAs (distance $<$ 0.6 nm) revealed that the dsNS and dsTRS are in close interaction with N-NTD throughout the 100 ns MD simulations (Fig. 1 *D*, *bottom*). These parameters (RMSD and contacts) validate the structural models generated for the N-NTD/dsRNA complexes as well as the molecular structures of the investigated biomolecules (dsNS, dsTRS, and N-NTD). The nonaveraged values of the analyzed parameters for each of the 25 MD simulations are provided in Figs. S3–S11.

Stability of dsNS and dsTRS basepairing upon N-NTD binding

To gain further insights into the molecular events that trigger dsRNA destabilization as part of the N-NTD melting activity, we used the MD simulations to probe the stability of the free and N-NTD-bound dsRNA. It is worth mentioning that these simulations do not probe the dsRNA melting activity per se but the initial steps of the melting reaction, as the whole process happens on a timescale of seconds.

To estimate the stability of the WC basepairing of dsNS and dsTRS complexed with N-NTD, we evaluated the RNA-RNA hydrogen bonds formed between sense and antisense strands of the dsRNA bound to N-NTD. The RNA-RNA hydrogen bonds of the free RNA molecules were investigated as a control parameter. The MD simulations of the free dsRNAs reflect transient hydrogen bonds typical of A-type dsRNA, with the expected average number of hydrogen bonds (18 for dsNS and 16 for dsTRS), maintained throughout the 100 ns simulations for all 25 replicas. Fig. 2 shows the number of RNA-RNA hydrogen bonds for 25 replicas of MD simulations of the free and N-NTD-bound dsTRS. It is possible to note that the score profile of RNA-RNA hydrogen bonds for free dsTRS (Fig. 2 *A*) was different than that of N-NTD-bound dsTRS (Fig. 2 *B*). This difference is mainly due to a considerable reduction in the number of RNA-RNA hydrogen bonds in at least four replicas of the set of 25 MD simulations (runs 5, 8, 17, and 25), suggesting that dsTRS WC basepairing was destabilized by interaction with the N-NTD. The score profile of the RNA-RNA hydrogen bonds for the N-NTD-bound dsNS (Fig. 2 *C*) was also reduced, especially for runs 15 and 23 (Fig. 2 *D*). Note that the reduction of the number of hydrogen bonds is more pronounced for the N-NTD-bound dsTRS than for dsNS. For runs 5, 8, 17, and 25 of the bound dsTRS, the number of hydrogen bonds dropped to a range between 2 and 11 (from *dark blue* to *cyan*, Fig. 2 *B*), whereas for the bound dsNS, this number dropped

to a range of 11–17 (from *light green* to *dark green*, Fig. 2 *D*). It is important to highlight that the color scale is the same for all MD simulations, being that the difference between the predominant color observed for dsTRS (mostly *green*) and dsNS (mostly *yellow*) is due to the maximal number of WC hydrogen bonds in each dsRNA.

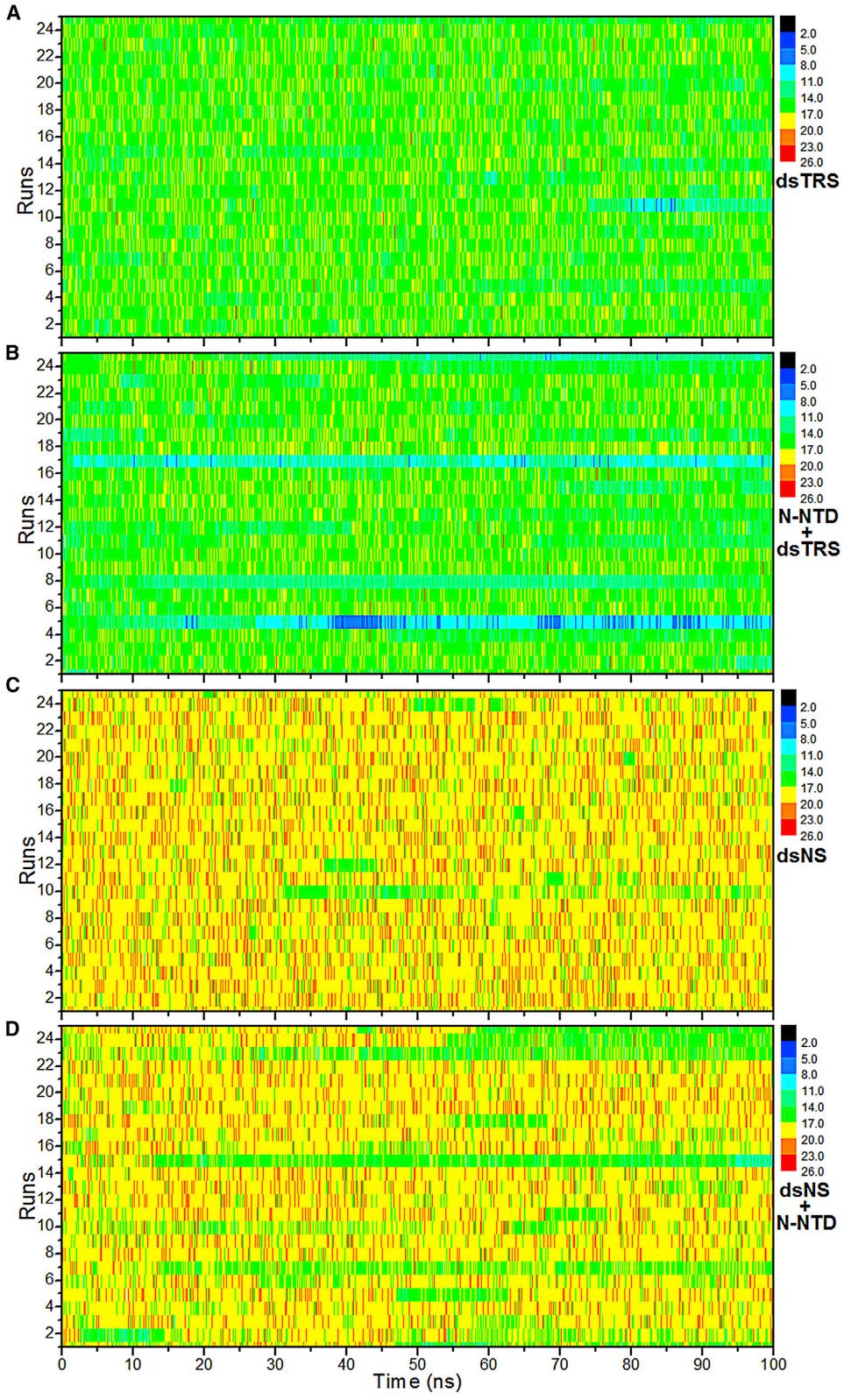

FIGURE 2 Stability of the WC basepairing via RNA-RNA hydrogen bonds of dsRNAs. The number of RNA-RNA hydrogen bonds formed between the sense and antisense strands of dsNS and dsTRS in their free states (*A* and *C*) and in complex with N-NTD (*B* and *D*) over the 100 ns simulations for the 25 MD replicas (runs) is shown. The plot takes into consideration the canonical WC basepairing, which represents the majority of hydrogen bonds (18 for dsNS and 16 for dsTRS), and noncanonical transient hydrogen bonds. The color bar denotes the correspondence between the color code and the number of RNA-RNA hydrogen bonds.

We also performed a quantitative analysis of WC basepairing by calculating the average number of RNA-RNA hydrogen bonds throughout the 100 ns MD simulations for each of the 25 replicas. For the free dsRNAs, the average numbers of RNA-RNA hydrogen bonds were constant for the 25 runs (Fig. 3 *A*) with an overall average value of 18.2 ± 0.2 and 15.5 ± 0.3 for dsNS and dsTRS, respectively. It is worth noting that the expected value of WC hydrogen bonds for dsNS and dsTRS are 18 and 16, respectively, and that the MD simulations reproduced the dynamic break-and-formation fluctuations of WC hydrogen bonds for free dsRNAs.

For most runs, the behavior of N-NTD-bound dsRNAs was similar to that of their free states, in which dynamic break-and-formation fluctuations of the RNA-RNA hydrogen bonds were observed. In the case of dsTRSs, there was a significant decrease in the average number of RNA-RNA hydrogen bonds for the runs 5, 8, 17, and 25 due to a long-lasting break of these bonds over 100 ns simulations, which resulted in partial (runs 8, 17, and 25) or total (run 5) RNA strand separation. For dsNS, runs 15 and 23 also showed a long-lasting break of RNA-RNA hydrogen bonds along the 100 ns MD simulations, leading to a partial RNA strand separation (Fig. 3 *A*). The N-NTD-bound dsTRS showed more events of partial and total strand separation than the protein-bound dsNS. Fig. 3 *B* shows a total separation event of the WC basepairing observed in run 5 for dsTRS, whereas a similar behavior with partial strand separation occurred in runs 8, 17, and 25 (Fig. S12). For the runs with only transient breaks of RNA-RNA hydrogen bonds (Fig. S13), the presence of N-NTD also promoted more pronounced dynamic break-and-formation fluctuations of these hydrogen bonds. Excluding the runs with long-lasting breaks of WC hydrogen bonds, we calculated the overall average number of RNA-RNA hydrogen bonds of 17.6 ± 0.8 and 15.5 ± 0.4 for the N-NTD-bound states of the dsNS and dsTRS, respectively. Note that increased dynamic break-and-formation fluctuations were more noticeable for dsNS.

We also analyzed the protein-RNA interaction along the MD simulations. The hydrogen bonds formed between the nitrogenous bases of dsRNA and N-NTD exhibited a transient nature. For most runs, these transient interactions displayed periods with a high number of protein-nitrogenous base hydrogen bonds (up to 13 for dsTRS and up to 9 for dsNS), followed by periods with no hydrogen bonds. These periods are typically of tens of nanoseconds (Fig. S14). To quantify the presence of protein-nitrogenous base hydrogen bonds along the 100 ns MD simulations, we analyzed the distribution of their frequency of occurrence. When all 25 replicas are considered, the distribution plot showed the highest occurrence of two hydrogen bonds for N-NTD/dsTRS and three for N-NTD/dsNS (Fig. 3 *B*, *top*). This can be explained by the fact that the dsNS has more hydrogen bond-forming sites (acceptor and donor) than the dsTRS. The distribution plot for the N-NTD/dsNS complex is more symmetric in reference to the maximal occurrence frequency, whereas the plot for the N-NTD/dsTRS complex is asymmetric, leaning toward the

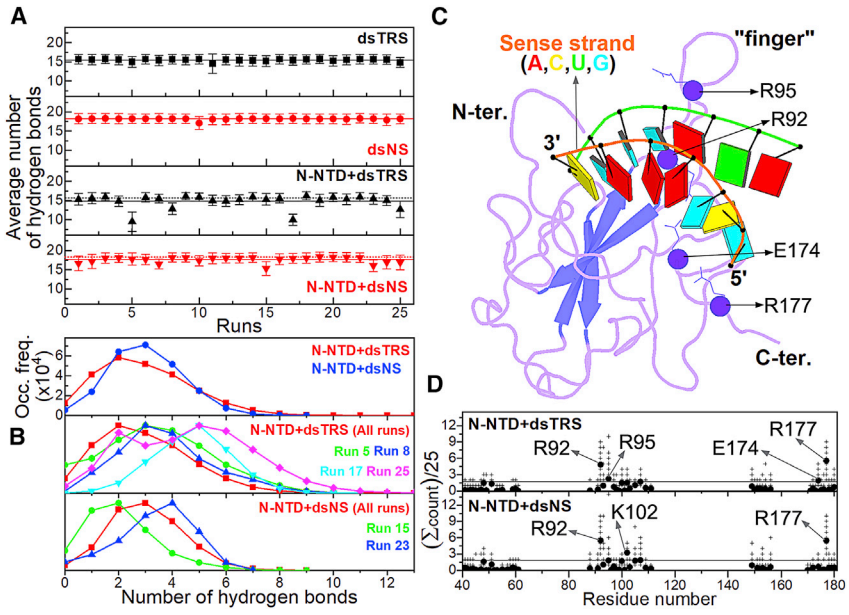

FIGURE 3 Analysis of the RNA-RNA and protein-RNA hydrogen bonds. (*A*) The average number of RNA-RNA hydrogen bonds between the sense and antisense strands of dsNS (*red*) and dsTRS (*black*) in their free states (*squares* and *circles*) and in complex with N-NTD (*up* and *down triangles*, respectively) for each of the 25 replicas of 100 ns MD simulation. The black and red solid lines denote the overall average values for the 25 runs, which are also presented numerically with their respective SDs. The dotted line shows the overall average values for the 25 runs for the free dsRNA. The standard deviation along the MD simulation for each replica is denoted by the error bars. (*B*, *top*) Distribution of the occurrence frequency of the number of hydrogen bonds between the nitrogenous bases of dsRNA (dsTRS in *red* and dsNS in *blue*) and N-NTD for the 25 replicas along the 100 ns MD simulations. (*Middle*) Normalized distribution of occurrence frequency of the number of protein-nitrogenous base hydrogen bonds for all 25 replicas (*red*) and runs 5 (*green*), 8 (*blue*), 17 (*cyan*), and 25 (*magenta*) of the N-NTD/dsTRS complex. (*Bottom*) Normalized distribution of the number of protein-nitrogenous base hydrogen bonds for all 25 replicas (*red*) and runs 15 (*green*) and 23 (*blue*) of the N-NTD/dsNS complex. (*C*) Structural model of the N-NTD/dsTRS complex representative of the MD simulation for run 5. The protein is shown in a purple cartoon, and dsTRS is denoted as a ribbon model with nitrogenous bases and basepairing as colored squares and rectangles, respectively. The color of the squares corresponds to the type of nitrogenous base, namely A: red, C: yellow, U: cyan, and G: green, and the rectangles refer to the nitrogenous base color of the dsRNA sense strand. (*D*) Average counts per replica of protein-RNA hydrogen bonds with percentage of persistence higher than 10% as a function of the residue number (*solid circle*). The crosses show the counts for each replica. The horizontal line shows the threshold of the average counts averaged over all residues plus one SD. To see this figure in color, go online.

occurrence of a higher number of protein-nitrogenous base hydrogen bonds. This profile aspect indicates that the transient nature of these interactions is more pronounced for the simulations of the N-NTD-bound dsTRS than dsNS (Fig. 3 *B*, *top*).

Next, we analyzed the distribution plots of individual replicas for which we observed destabilization of RNA-RNA hydrogen bonds of the dsRNAs. For dsTRS, runs 5, 8, 17, and 25 displayed distribution curves with higher occurrence frequencies of frames containing a higher number of protein-nitrogenous base hydrogen bonds when compared to the curve with all replicas (shifted to the *right*, Fig. 3 *B*, *middle*). In contrast, replicas 15 and 23 for dsNS showed a conflicting behavior (Fig. 3 *B*, *bottom*). Run 15 exhibited a distribution plot with higher occurrence frequencies of frames with a lower number of protein-nitrogenous base hydrogen bonds (shifted to the *left*) when compared to the entire distribution, considering all 25 replicas, whereas run 23 displayed an opposite behavior (shifted to the *right*). These results suggest that the breaking down of RNA-RNA hydrogen bonds in runs 5, 8, 17, and 25 for dsTRS possibly leads to an increase in occurrence frequencies of a higher number of protein-nitrogenous base hydrogen bonds. In contrast, the same cannot be suggested for dsNS. However, we cannot claim that the formation of protein-RNA hydrogen bonds between N-NTD and the nitrogenous bases of TRSs (single strand and/or duplex) is replacing the RNA-RNA hydrogen bonds of the dsRNA because we observed transient increases in occurrence frequencies of a higher number of protein-nitrogenous base hydrogen bonds for runs without a significant break in the RNA-RNA hydrogen bonds (Figs. S15 and S16). Nevertheless, this last observation indicates that the transient protein-nitrogenous base hydrogen bonds can compete with WC basepairing and consequently increase the propensity of dsRNA destabilization.

To identify the main amino acid residues participating in the hydrogen bonds between N-NTD and all atoms of dsRNAs, we counted the number of protein-RNA hydrogen bonds with a percentage of persistence higher than 10% for the 25 runs (Tables S1–S50) and plotted the average count as a function of the residue number (Fig. 3 *D*). Most counts were observed for the N-terminal region (residues 40–61), the finger (β2-β3 loop, residues 88–111), α2-β5 loop (residues 149–156), and the β5 and C-terminal region (residues 170–180). The identified regions are the same observed in the CSP titration by NMR, the only N-NTD-dsRNA data available experimentally (16). For dsTRS, a significant count (higher than average plus standard deviation (SD)) of protein-RNA hydrogen bonds was observed for R92, R95, E174, and R177. Most of these hydrogen bonds involving arginine residues occur with dsRNA phosphate groups, making them also a salt bridge. We also observed a minor count of protein-RNA hydrogen bonds between the arginine residues and the ribose. The significant count for E174 is remarkable because it is unique for dsTRS, and it is characterized by the formation of protein-RNA hydrogen bonds with the nitrogenous bases. For dsNS, significant counts were identified for R92, K102, and R177. As for dsTRS, R92 and R177 are involved in hydrogen bonds with dsRNA phosphate groups. In contrast, K102 makes hydrogen bonds with the nitrogenous base. We also counted the protein-RNA hydrogen bonds from the perspective of the dsRNAs. Interestingly, the higher counts were observed for the 5′-end of the negative-sense strand (Fig. S17).

To further understand the stability of the WC basepairing for N-NTD-bound dsNS and dsTRS, we used the *do_x3dna* tool (31) along with the 3DNA package (32) to analyze the local basepair parameters (angles: buckle, opening, and propeller; distances: stretch, stagger, and shear) from the MD simulations. Fig. 4 shows the population distributions of these local basepair parameters for runs 5, 8, 17, and 25 (for dsTRS), and runs 15 and 23 (for dsNS), both free and complexed with N-NTD, as well as the difference between the distributions of the free and N-NTD-bound states. These replicas were selected based on the results presented in Fig. 3 *A*, as their average numbers of RNA-RNA hydrogen bonds were significantly lower than the overall average values. From Fig. 4, it is clear that N-NTD perturbs the population distributions of the local basepair parameters of dsRNAs, most notably for dsTRS.

The distribution of dsTRS buckle angles revealed a reduction in the population at $\sim$0° (basepairing planarity) and increase in subpopulations at $\sim\pm$30° due to the interaction with the N-NTD. This can be clearly seen by the difference in distributions between the N-NTD-bound and free states (*inset* in *buckle plot* of Fig. 4). A similar but less intense effect was observed for the population distribution of dsNS buckle angles. For the opening angles, one can note a higher perturbation of population distribution for dsTRS than for dsNS upon binding to N-NTD. For dsTRS, the opening angle population at $\sim$0° (basepairing closure) decreased significantly, whereas subpopulations emerged for angles higher than 50°, remarkably at $\sim$90°. The distribution of the propeller angles showed a reduction in the equilibrium populations at $-$12.6 and $-$13.8° for dsTRS and dsNS, respectively, after interaction with N-NTD, with an increase in subpopulations around 0° (less twist), which was significantly larger for dsNS. However, we observed an extra subpopulation of propeller angles at approximately $-$30° for dsTRS after binding to N-NTD, which was not seen for dsNS (see the *inset* in *propeller plot* in Fig. 4).

Investigation of the stretch, stagger, and shear distances for dsNS and dsTRS showed that the equilibrium population at $\sim$0 Å decreased for both dsRNAs as a result of N-NTD binding. However, this reduction is more drastic for dsTRS than dsNS, as can be seen in the inset for the respective plots in Fig. 4. In addition to this reduction effect, we also verified that N-NTD-bound dsTRS exhibited clear subpopulations at $\sim$1, $\sim\pm$1.5, and $\sim$3 Å for the stretch, stagger, and shear distances, respectively.

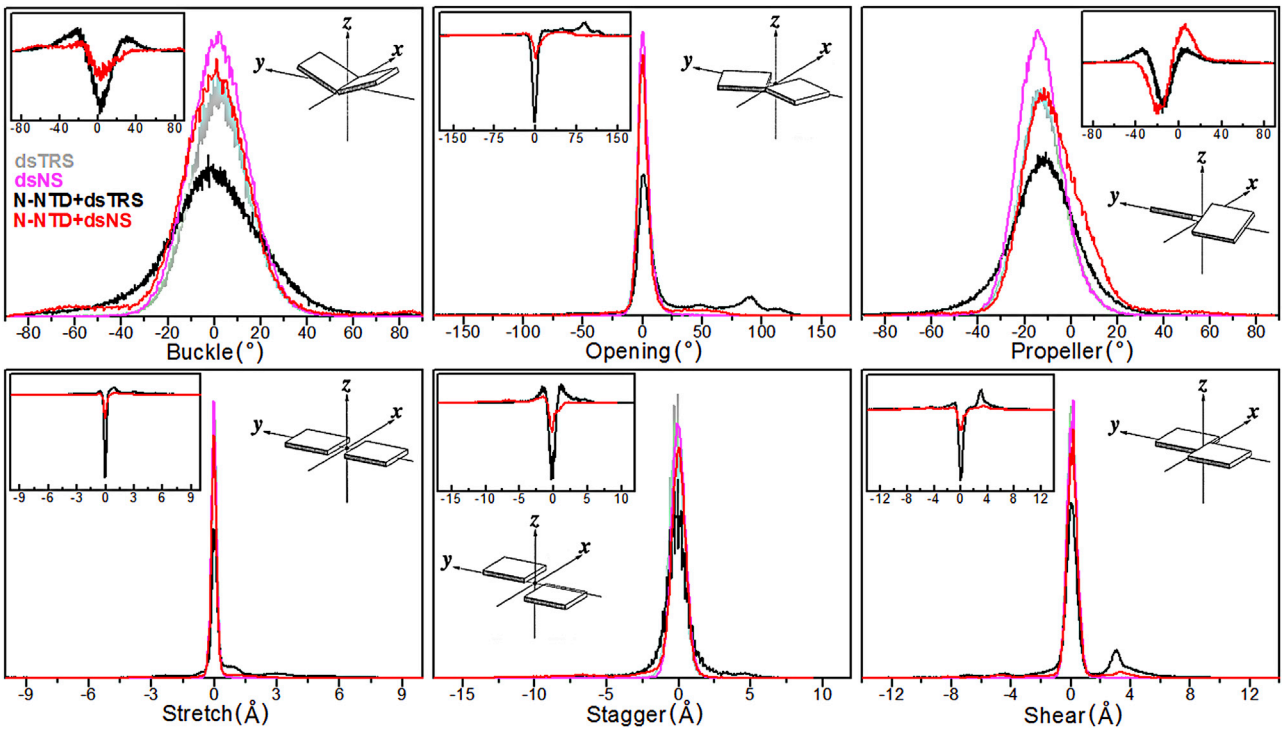

FIGURE 4 Normalized population distributions of the local basepair parameters. Normalized population distributions of local basepair parameters (angles: buckle, opening, and propeller; distances: stretch, stagger, and shear) for runs 5, 8, 17, and 25 of dsTRS and runs 15 and 23 of dsNS in their free form (dsTRS in *light gray* and dsNS in *magenta*, respectively) and complexed with N-NTD are shown (N-NTD + dsTRS in *black* and N-NTD + dsNS in *red*). The normalization was defined with respect to the highest distribution curse for each basepair parameter. The plot insets correspond to the difference between the population distributions of N-NTD-bound dsRNA minus its free state for dsNS (*red*) and dsTRS (*black*). The scheme insets illustrate the geometrical definition of each local basepair parameter (41). To see this figure in color, go online.

N-NTD-induced perturbations in the population distributions of angle and distance basepair parameters (buckle, opening, propeller, stretch, stagger, and shear) of dsRNAs for the selected replicates (runs 5, 8, 17, and 25 for dsTRS and runs 15 and 23 for dsNS) indicate that both dsRNAs suffered WC basepairing destabilization upon N-NTD binding. However, this destabilization effect is more evident for the N-NTD/dsTRS complex, as the above analysis of angle and distance parameters suggests an impairment of basepairing planarity accompanied by an increase in the separation between the nitrogenous bases of the complementary dsRNA strands upon N-NTD binding. This result agrees well with the analysis of the RNA-RNA hydrogen bonds formed between the sense and antisense dsRNA strands (see Fig. 3 *A*). It is worth mentioning that, even though basepairing destabilization was more pronounced for dsTRS than dsNS, dsNS suffered a greater reduction in the RNA duplex twist, as suggested by the N-NTD-induced perturbation of the propeller angles.

Conformational flexibility of free and dsRNA-bound N-NTD

To further understand how dsRNA binding changes the conformational dynamics of N-NTD, we concatenated the last 50 ns (stable RMSD values) of the 25 replicas for both free and dsRNA-bound N-NTD and performed an analysis of RMSF and PCA of the MD trajectories (Fig. 5). Fig. 5 *A* shows that both free and dsRNA-bound N-NTD exhibited significantly increased values of RMSF for residues in the N- and C-terminal regions as well as the β2-β3 loop (finger), suggesting large conformational flexibility. In addition to these regions, the N-terminal portions of the β1-Δ1 loop (residues 58–65) and β3-β4 loop are especially noteworthy. The β1-Δ1 and β3-β4 loops displayed an increase in their dynamics in the N-NTD/dsTRS complex when compared to free N-NTD and N-NTD/dsNS complex, even though they are not directly involved in the interaction. The conformational flexibility of the basic finger is similar for free and dsTRS-bound N-NTD, with a tendency of a slight gain in flexibility for the dsTRS-bound N-NTD, whereas dsNS-bound N-NTD became more rigid. In general, we observed an increase in flexibility of N-NTD loop regions when bound to dsTRS. Remarkably, conformational dynamics of the N-NTD/dsNS complex was similar to that of the free state, with the exception of the N-terminal region and basic finger, in which conformational dynamics decreased upon dsNS binding.

The PCA scatter plot generated for free and dsRNA-bound N-NTD revealed a significant difference between

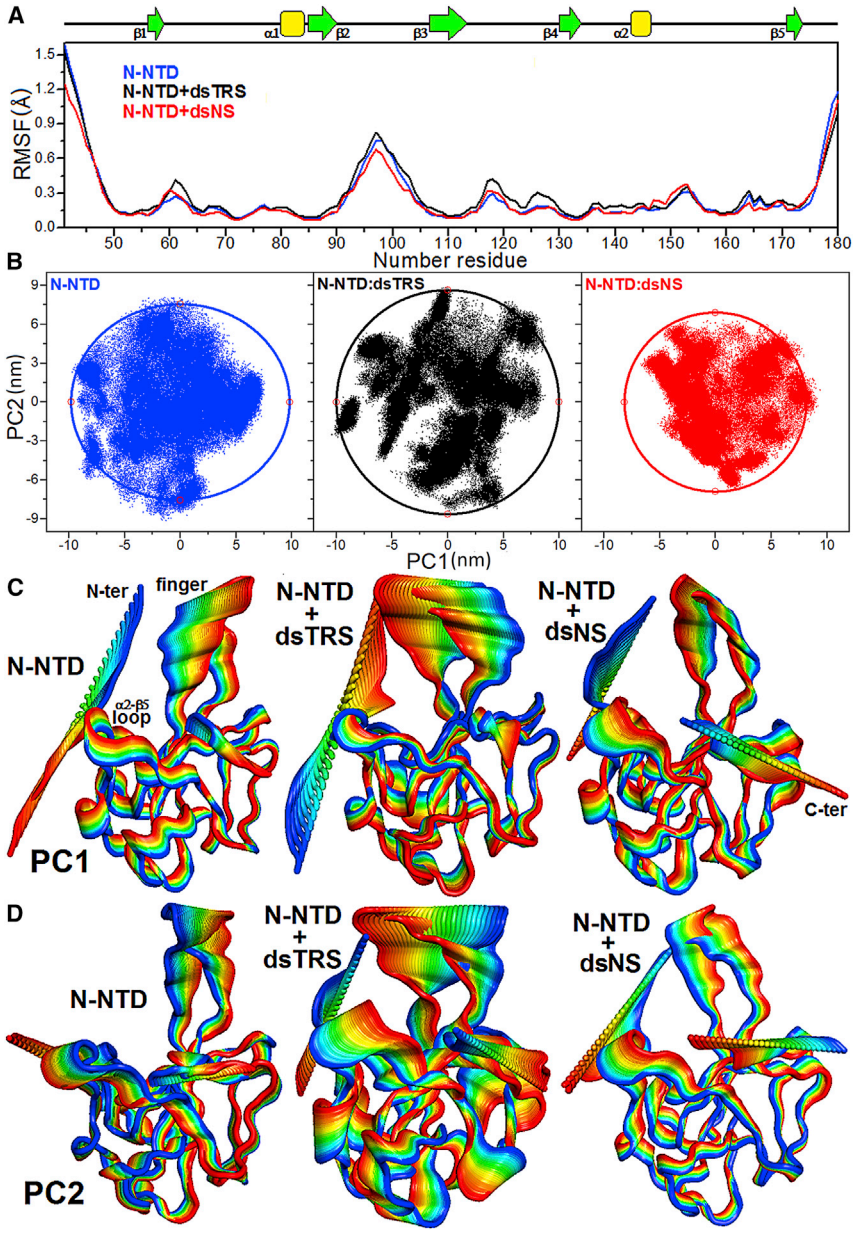

FIGURE 5 Analysis of N-NTD conformational flexibility in its free and dsRNA-bound states. (*A*) RMSF values as a function of residue number for N-NTD in its free state (*blue line*) and complexed with either dsTRS (*black*) or dsNS (*red*). The secondary structures along the sequence are indicated at the top. (*B*) PCA scatter plots PC1 and PC2 for free N-NTD (*blue dots*, *left*) and for N-NTD complexed with either TRS (*black dots*, *middle*) or NS (*red dots*, *right*) dsRNAs. The extent of the conformational space for each scatter plot was measured by fitting an elliptical shell (*solid lines*) that contains 95% of the density. (*C* and *D*) Motions filtered from the eigenvectors of PC1 (*C*) and PC2 (*D*) for the dynamics data of N-NTD in its free form and complexed with either dsTRS or dsNS. The motion direction is indicated by the color variation from blue to red. To perform the RMSF and PCA calculations, the last 50 ns of trajectories of the 25 replicates were concatenated for each of the molecular systems (free or dsRNA-bound N-NTD), resulting in MD simulations of 1.25 μs. To see this figure in color, go online.

the free domain and the complexes, as evident from the characteristic structures plotted along the direction of the first and second principal components (PC1 and PC2, respectively). 25 replicas of the MD simulations using different seeds of the random number generator provided a great exploration of the conformational space for free and dsRNA-bound N-NTD, resulting in trajectories of 1.25 μs. We analyzed the conformational space by fitting an elliptical shell that contains 95% (confidence) of the density for each scatter plot. The extent of the conformational space is proportional to area (S_{el}) of the elliptical shell. Despite the already wide conformational space of N-NTD (S_{el} = 929 nm^2), the interaction with dsTRS made it even wider (S_{el} = 1083 nm^2), whereas binding to dsNS made it more constrained (S_{el} = 708 nm^2; Fig. 5 *B*). We also analyzed the conformational space for trajectories of all 25 replicas of free N-NTD concatenated with its bound states (N-NTD/dsNS and N-NTD/dsTRS). By doing so, we guaranteed that the eigenvectors are the same used for all systems. The PCA scatter plots from this last analysis (Fig. S18) showed a similar profile with a wide conformational space for free NTD (S_{el} = 833 nm^2), even wider for dsTRS-bound N-NTD (S_{el} = 1002 nm^2), and constrained for dsNS-bound N-NTD (S_{el} = 616 nm^2).

An investigation of the motions filtered from the eigenvectors of PC1 and PC2 revealed that dsTRS-bound N-NTD exhibited the largest conformational dynamics when compared to free and dsNS-bound N-NTD, which

were similar (Fig. 5, *C and D*). We highlight that the most evident motions took place in the N- and C-termini as well as the basic finger ($\beta2$-$\beta3$ loop) for both free and dsRNA-bound N-NTD. However, the eigenvectors of PC1 and PC2 for the N-NTD/dsTRS complex suggested a wide motion between the basic finger and the $\Delta2$-$\beta5$ loop located at the palm, similar to a tweezer. Interestingly, this tweezer-like motion was intrinsic to the residues located at the dsRNA-binding cleft in N-NTD (Fig. 1 *A*).

Our results of conformational flexibility from RMSF and PCA for free and dsRNA-bound N-NTD corroborated each other and suggest a significant contribution of the N- and C-termini and the basic finger ($\beta2$-$\beta3$ loop) to N-NTD dynamics. They also revealed that N-NTD interaction with dsTRS led to a general gain in protein conformational flexibility when compared to its free state. We suggest that this flexibility gain of dsTRS-bound N-NTD over 25 replicas of concatenated simulations may be a key structural factor to promote dsTRS WC basepairing destabilization upon N-NTD binding, as determined by the break of RNA-RNA hydrogen bonds (Figs. 2 *B* and 3 *A*) and perturbation of the local basepair parameters (Fig. 4).

Modeling the dsRNA melting activity

Based on the MD simulations performed herein, we suggest that one molecule of N-NTD is enough to destabilize the WC basepairing of one RNA duplex, which is possibly the first step for dsRNA melting. To investigate the stoichiometry of the dsRNA melting, we simulated the experimental data obtained by Grossoehme et al. (10) using two contrasting kinetic models: 1) assuming that melting activity is the result of binding of one N-NTD to one dsRNA and 2) assuming that two N-NTD molecules bind to one dsRNA (sandwich model). The simulation strategy is detailed in the Supporting materials and methods.

In their work, Grossoehme et al. (10) measured dsRNA melting activity of N-NTD using fluorescent resonance energy transfer (FRET) from 5′ Cy3-labeled sense RNA strand (TRS) and 3′ Cy5-labeled antisense RNA strand (cTRS). In those experiments, the highest FRET efficiency (~0.9) was obtained for dsRNA in the absence of N-NTD. Increasing the N-NTD concentration led to the dsRNA melting curve, which is characterized by an exponential decay of FRET efficiency as a function of N-NTD concentration. The melting curves reached either zero for an N-NTD construct that contains the C-terminal serine/arginine-rich motif or a plateau for N-NTD itself (10).

Because the FRET efficiency is a measure of the molar fraction of dsRNA, in the simulated kinetic models presented here, we report the molar fraction of dsRNA as a function of N-NTD concentration, simulating the dsRNA melting curve (Fig. 6). We used the elementary rate constants for individual chemical steps to produce an absolute time base (Fig. 6 *A*). The starting condition mimics exactly

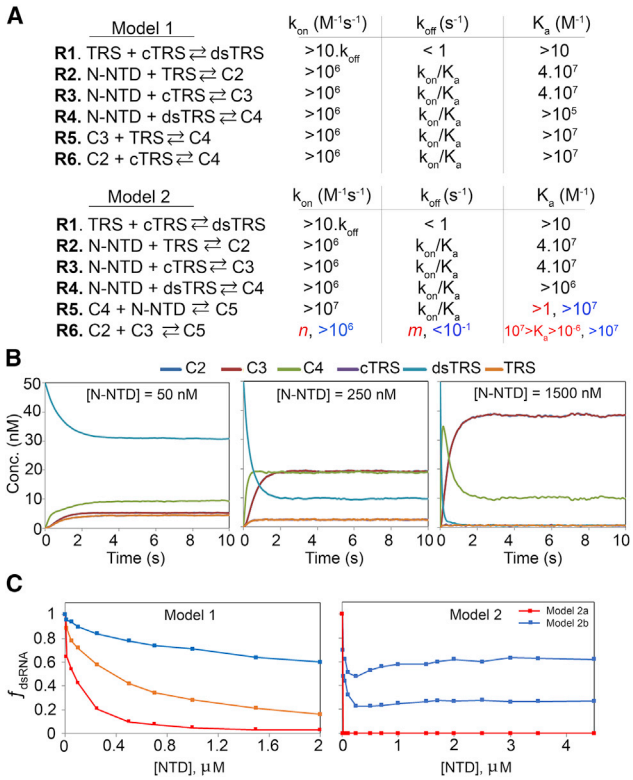

FIGURE 6 Simulation of the kinetics of dsRNA-melting activity. (*A*) Reactions R1–R6 for models 1 and 2. Model 1 implies the melting activity with stoichiometry of 1 N-NTD for 1 dsRNA (C4), and model 2 implies the formation of a sandwich with a stoichiometry two N-NTDs and one dsRNA (C5). At the right of each reaction are the ranges of k_{on}, k_{off}, and K_a in which the simulation produces a dsRNA-melting curve, respecting the boundaries described in the text. For reaction R6 of model 2, the color code refers to the color of the simulated melting curves for model 2. (*B*) Illustration of the kinetics of dsRNA-melting for model 1 in three different concentrations of N-NTD (50, 250, and 1500 nM). (*C*) Simulated dsRNA-melting curve for model 1 and 2. We used the starting concentration of 50 nM of dsRNA for all simulations. For model 1 simulations, we used the following reaction rates: k_{on} (R1) = 4×10^{-1} M^{-1} s^{-1} and $k_{off} = 8 \times 10^{-4}$ s^{-1}; k_{on} (R2, R3) = 4×10^{7} M^{-1} s^{-1} and $k_{off} = 1$ s^{-1}; k_{on} (R4) = 1×10^{7} M^{-1} s^{-1} and $k_{off} = 1$ s^{-1}; k_{on} (R5, R6) = 4×10^{7} M^{-1} s^{-1} and $k_{off} = 1$ s^{-1} (*red*); k_{on} (R5, R6) = 4×10^{8} M^{-1} s^{-1} and $k_{off} = 1$ s^{-1} (*orange*); and k_{on} (R5, R6) = 6×10^{8} M^{-1} s^{-1} and $k_{off} = 1 \times 10^{-1}$ s^{-1} (*blue*). For model 2 simulations, we used the following reaction rates: k_{on} (R1) = 4×10^{-1} M^{-1} s^{-1} and $k_{off} = 8 \times 10^{-4}$ s^{-1}; k_{on} (R2, R3) = 4×10^{7} M^{-1} s^{-1} and $k_{off} = 1$ s^{-1}; k_{on} (R4) = 1×10^{7} M^{-1} s^{-1} and $k_{off} = 1$ s^{-1}; k_{on} (R5) = 1×10^{8} M^{-1} s^{-1} and $k_{off} = 1$ s^{-1} (*red*); k_{on} (R6) = 1×10^{-1} M^{-1} s^{-1} and $k_{off} = 1 \times 10^{8}$ s^{-1} (*red*); k_{on} (R6) = 1×10^{6} M^{-1} s^{-1} and $k_{off} = 1 \times 10^{-1}$ s^{-1} (*blue*, *bottom*); and k_{on} (R6) = 1×10^{7} M^{-1} s^{-1} and $k_{off} = 1 \times 10^{-1}$ s^{-1} (*blue*, *top*). To see this figure in color, go online.

the experimental condition, varying the concentration of N-NTD over 50 nM dsRNA (dsTRS). The predictions were validated by direct comparison to the experimental data (10).

To simulate the melting curve, we had to constrain the kinetic space, which is large because each model is composed of six reactions and 12 individual rate constants, assuming the following boundaries: (B1) the kinetic model must be

complete, complying with all possible reactions for a given mechanism; (B2) the presence of N-NTD must lead to catalysis, with the melting of dsRNA being faster than the annealing reaction; (B3) the equilibrium of the annealing is shifted toward the dsRNA; and (B4) the equilibrium for the melting activity must be reached in less than 133 s (10).

The criterion for choosing the rate constants for the annealing reaction (R1; Fig. 6) was that it must be significantly slower than the melting activity (catalysis). To yield an equilibrium shifted toward the dsRNA, we used $k_{on} = 4 \times 10^{-1}$ $M^{-1} \cdot s^{-1}$, which is true below the melting temperature of the dsRNA, values measured for the almost inactive mutant Y127A (10). Any values of $k_{off} < 1$ s^{-1}, with an association constant K_a, gives the same molar fraction of dsRNA. We constrained the binding reactions R2 and R3 of N-NTD to the sense (TRS) and antisense (cTRS) single-stranded RNA (ssRNA) (Fig. 6 *A*) based on the published experimental values for these association constants (10,42). For dsRNA (dsTRS) binding, there were no experimental data to constrain the simulation. However, simulations unambiguously showed that K_a for reaction R4 must be of the same order of that for ssRNAs, leading to the allowed ranges depicted in Fig. 6 *A*. We also determined k_{on} based on the simulations.

The simulated melting curves for model 1 resembled the near-exponential decay observed experimentally (Figs. 6 *C*, *left*, and S19). Remarkably, melting curves that either decayed to zero or reached a plateau were observed experimentally. There are no experimental data available to constrain reactions R5 and R6, but the simulations showed that they are tightly related to reactions R2 and R3, being both K_a and k_{off} of the same order of magnitude for reactions R2 and R3 (Fig. S19). Interestingly, when k_{off} of reactions R5 and R6 were larger than k_{off} for reactions R2 and R3, we observed a plateau in the exponential decay of the dsRNA melting curve (Fig. 6 *C*).

We also evaluated the kinetic model 2, in which a sandwich of 2 N-NTD and 1 dsRNA is necessary for the melting reaction. This stoichiometry for N-NTD melting activity should be considered, as the full-length N protein is a biologically functional dimer and recognition of the TRS duplex by the two N-NTD subunits for the melting activity is possible. In this model, a sandwich of two N-NTDs and one dsRNA is formed, and the final products are each N-NTD bound to TRS and cTRS ssRNA. To build a kinetic model that would exclusively produce ssRNA from the sandwiched dsRNA, we replaced reactions R5 and R6 of kinetic model 1. In this new model, reaction R5 forms the sandwiched dsRNA (C5; Fig. 6 *A*) and reaction R6 is the dissociation of C5 into the ssRNA-bound N-NTDs (C2 and C3; Fig. 6 *A*). To simulate N-NTD melting activity considering model 2, we used the same boundaries described earlier (B1, B2, B3, and B4), with reactions from R1 to R4 having almost the same constraints described for the model 1. We scanned all the kinetic space that led to the catalysis of melting activity and observed two contrasting situations. The first is when reaction R6 equilibrium is between 10^{-6} and 10^{7} M^{-1}, always having the dissociated forms C2 and C3 available and making the melting curve very stiff (model 2a). The second is the opposite situation, where equilibrium is skewed toward the sandwich state (C5) with $K_a > 10^{7}$ M^{-1} (model 2b). Fig. 6 *C* illustrates the melting curves obtained for the two situations.

Model 2a is characterized for the high efficiency in the dissociation of the dsRNA, k_{on} and k_{off} can assume any value (*n* and *m*, Fig. 6 *A*) as long as K_a is between 10^{-6} and 10^{7} M^{-1}. All simulated conditions led to the curve in red (Fig. 6 *C*), in which the minimal amount of N-NTD (10 nM) led to complete dissociation of the dsRNA (molar fraction of zero). Fig. S20 illustrates all the simulated boundaries. Note that for model 2a, there is never an accumulation of C5 (Fig. S20).

Model 2b corresponds to when the equilibrium of reaction R6 is shifted toward C5 ($K_a > 10^{7}$ M^{-1}). Fig. S21 illustrates the reaction boundaries. In this situation, we were able to observe a melting curve (Fig. 6 *C*, *blue*) with a near-exponential decay at a low concentration of N-NTD and a near-exponential rise at higher concentrations of N-NTD. This behavior is explained by the accumulation of C5 and N-NTD concentration-dependent mutual compensation of C5 and dsRNA. None of the situations simulated for model 2 are parallel to the experimental observation.

DISCUSSION

In this work, we used computational simulations to unravel the triggering event for the dsRNA melting activity of the isolated SARS-CoV-2 N-NTD. Our MD simulations showed the first steps that occurred in the nanosecond timescale. During interaction with dsRNA, protein dynamics drives the destabilization of hydrogen bonds involved in the WC dsRNA basepairing, probably in a 1:1 stoichiometry (N-NTD/dsRNA). We also showed that the capacity of the N-NTD to promote more permanent breaking events of the WC basepairing was sequence specific, being more efficient for dsTRS (5′-UCUAAAC-3′ and 5′-AGAUUUG-3′; sense and antisense) than for a nonspecific (dsNS) sequence (5′-CACUGAC-3′ and 5′-GUCAGUG-3′; sense and antisense). The MD simulation did not give information on the melting activity, which is an event that occurs in seconds. We probed the destabilization of the RNA duplex, which occurred in nanoseconds and only in the presence of N-NTD. To further explore the N-NTD/dsRNA stoichiometry, we constructed kinetic models based on the available experimental data (10). Remarkably, the model using a 1:1 stoichiometry greatly fits the experimental data, reinforcing the model we hypothesize here.

The strategy of performing 25 100 ns MD simulations with the same starting structure but different seeds of the random number generator provided a large sampling of

conformational space of each molecular system (N-NTD, dsRNAs, and N-NTD/dsRNA complexes). This set of theoretical data ensured a significant result showing that N-NTD destabilizes the WC basepairing, especially for dsTRS. Specifically, for the dsTRS, we observed an increase in formation of hydrogen bonds between N-NTD and the nitrogenous bases of each RNA strand, followed by a decrease in RNA-RNA hydrogen bonds between the dsRNA strands. The results also revealed that the rigid-body geometric parameters of the dsTRS WC basepairing were significantly changed because of N-NTD binding.

To map the main protein-RNA hydrogen bonds and salt bridges, we counted the most prevalent protein-RNA hydrogen bonds. The mapped regions are consistent with available experimental data of NMR titration with dsRNA (16). The main protein-RNA interactions are mediated by arginine residues, mainly at the finger and the C-terminal region. Although these regions are flexible (as observed from PCA), many hydrogen bonds were persistent and displayed a high percentage of persistency. R92 (finger) and R177 (C-terminal) form hydrogen bonds with the RNA phosphates, which are also persistent salt bridges for both dsTRS and dsNS. For dsTRS, we observed persistent hydrogen bonds and salt bridges with the RNA phosphates involving R95 and persistent hydrogen bonds with E174. The presence of hydrogen bonds involving E174 is remarkable because it involves a negatively charged residue and an interaction with a nitrogenous base. E174 may be a key residue responsible for the difference in N-NTD-induced destabilization of dsTRS and dsNS.

One notable N-NTD structural feature is the presence of a significant number of loops; only 32 out of 140 residues are involved in secondary structure (16,43). This is a typical feature of a dynamic protein. In fact, our results revealed that the N-NTD is a plastic protein, with the N- and C-termini and the β2-β3 loop (finger) as the most prominent dynamic regions. For the N-NTD/dsTRS interaction, a remarkable tweezer-like motion between the finger and the Δ2-β5 loop might be related to the sequence-specific WC basepairing destabilization. This information goes along with the observed transient protein-RNA hydrogen bonds within the timescale of tens of nanoseconds. Therefore, we hypothesized that after the formation of the N-NTD/dsTRS complex, the tweezer-like motion resulted from intrinsic protein dynamics might promote a steric effect causing a "compaction pressure" on the dsRNA strands. This might expose residues from the bottom of the palm (finger/Δ2-β5 cleft), allowing their interaction with the bases and leading to the destabilization of the WC basepairing (Fig. 7).

The naturally occurring canonical RNA double helices are short (not larger than 12 nucleotides in length), possibly linked to the tendency of RNAs to form tertiary structures because of their intrinsic mechanic properties. The extra 2′ hydroxyl group provides many possibilities of noncanonical non-WC basepairs (37). dsRNA tends to unwind upon elongation in a sequence-dependent manner. Alternating purine-pyrimidine (AC, GC, AU, GU) and pyrimidine-purine (CA, CG, UA, UC) are softer than purine-purine (AA, GG) sequences (38). We may speculate that the TRS specific sequence used here (5′-UCUAAAC-3′) contains the AAA motif that is hard, and consequently, the force-induced unwinding is more difficult. The regions flanking the consensus TRS are softer and prompter to bend. Consequently, the biologically relevant dsRNA presented to the N-NTD is probably short.

To confirm the model that emerged from the MD simulations, in which the dynamics of only one molecule of N-NTD was enough to trigger the dsRNA destabilization, we constructed kinetic models considering two possible scenarios: a stoichiometry of 1:1 or 2:1 for N-NTD and dsRNA. The 2:1 stoichiometry is more intuitive because N protein is dimeric in solution (44). However, the 1:1 stoichiometry produced dsRNA melting curves compatible with the available experimental data (10). It is important to mention that the simulations of the kinetic models were only possible by constraining the kinetic space, as the number of degrees of freedom for six reactions is quite large. This constrained kinetic space was created by imposing boundaries to the system. These simulations brought two important conclusions: 1) the 1:1 stoichiometry is enough to explain the experimental data and 2) the sandwich model 2 is less likely to

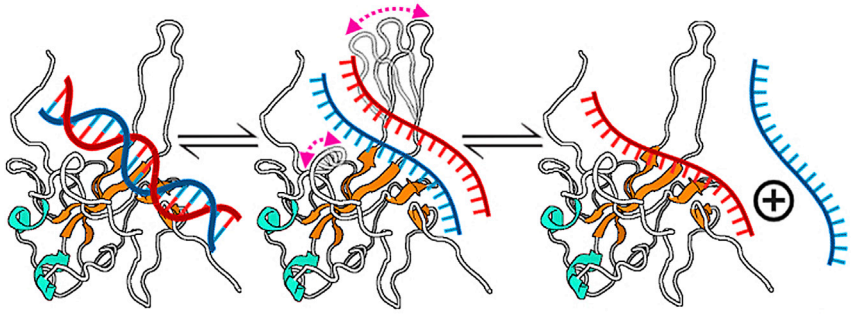

FIGURE 7 Summary of the proposed mechanism for dsRNA melting activity of N-NTD. The binding of one N-NTD to one dsRNA triggers the destabilization of WC basepairing of the dsRNA and consequently exposes the nitrogenous bases for interacting directly with the N-NTD. We suggest that this activity is a consequence of intrinsic dynamics of N-NTD, especially because of the tweezer-like motion between β2-β3 (finger) and Δ2-β5 loops. The protein is denoted as cartoon with the helix-Δ and β-strand secondary structures colored in cyan and orange, respectively. The dsRNA is showed as a line model with the complementary strands colored in red and blue. The tweezer-like motion between the finger and Δ2-β5 loop is indicated by bidirectional arrows colored in magenta. To see this figure in color, go online.

occur because simulations produced more complex melting curves, which are different from the experimental data.

Model 1 agrees with the previously proposed stoichiometry for the melting activity (10), which described that the formation of a sandwich (model 2) in diluted solution with the isolated domain is unlikely. Grossoehme et al. (10) modeled the system with four reactions (R1, R2, R3, and R4) and concluded that for the melting activity to occur, K_a for R4 would be $<1\ M^{-1}$, which suggests an almost absent interaction of the dsRNA with the N-NTD. We showed here that model 1 describes the melting curves, considering the affinity of the dsRNA similar to the ssRNAs, which is more compatible with recent experiments (16). These authors reported a binding affinity for the N-NTD/dsRNA complex in the range of micromolar, similar to the simulated conditions showed in Fig. 6.

Altogether, the results presented here support the idea that two N-NTDs of dimeric N protein would not be necessary to act on one dsRNA motif (dsTRS). Each N-NTD of the same dimer would work independently, leading to a gain in efficiency of full-length N when compared to the sandwich model. The observation that one N-NTD could be able to melt dsRNA opens two new, to our knowledge, avenues for the understanding of the role played by the N protein in the viral replication cycle. First, the two N-NTD arms of full-length N could bind to two different RNA sites, which could either be spatially or closely separated in the viral genome, making it possible to bridge and induce melting on two different regions in a cooperative manner. Second, if monomeric full-length protein is active, a regulatory event involving the dissociation of the N protein dimer should be considered. Indeed, for the N protein of bovine betacoronavirus, studies suggested that it acts as a bridge between distant motifs in the genome (45).

SUPPORTING MATERIAL

Supporting material can be found online at https://doi.org/10.1016/j.bpj.2021.06.003.

AUTHOR CONTRIBUTIONS

Í.P.C. performed the MD simulations and analysis. K.S. and F.C.L.A. modeled the kinetics of RNA melting and analysis. A.S.P., A.T.D.P., F.C.L.A., and Í.P.C. participated in the experimental design and analysis. All authors contributed to the writing.

ACKNOWLEDGMENTS

Í.P.C. gratefully acknowledges the financial support by postdoctoral fellowship from Fundação Carlos Chagas Filho de Amparo à Pesquisa do Estado do Rio de Janeiro (FAPERJ) and the Pró-Reitoria de Pesquisa da Universidade Estadual Paulista Júlio de Mesquita Filho (PROPe UNESP). The authors are grateful for the access to the Santos Dumont supercomputer at the National Laboratory of Scientific Computing, Brazil. FAPERJ, Brazil: Grant 255.940/2020, 202.279/2018, 239.229/2018, 210.361/2015, and 204.432/2014. Conselho Nacional de Desenvolvimento Científico e Tecnológico–CNPq, Brazil: 309564/2017-4 and 439306/2018-3.

SUPPORTING CITATIONS

References (46–48) can be found in the Supporting material.

REFERENCES

1. Zhu, N., D. Zhang, …, W. Tan; China Novel Coronavirus Investigating and Research Team. 2020. A novel coronavirus from patients with pneumonia in China, 2019. *N. Engl. J. Med.* 382:727–733.
2. Zhou, P., X. L. Yang, …, Z. L. Shi. 2020. A pneumonia outbreak associated with a new coronavirus of probable bat origin. *Nature.* 579:270–273.
3. Klein, S., M. Cortese, …, P. Chlanda. 2020. SARS-CoV-2 structure and replication characterized by in situ cryo-electron tomography. *Nat. Commun.* 11:5885.
4. Naqvi, A. A. T., K. Fatima, …, M. I. Hassan. 2020. Insights into SARS-CoV-2 genome, structure, evolution, pathogenesis and therapies: structural genomics approach. *Biochim. Biophys. Acta Mol. Basis Dis.* 1866:165878.
5. Fang, S. G., H. Shen, …, D. X. Liu. 2008. Proteolytic processing of polyproteins 1a and 1ab between non-structural proteins 10 and 11/12 of Coronavirus infectious bronchitis virus is dispensable for viral replication in cultured cells. *Virology.* 379:175–180.
6. Snijder, E. J., Y. van der Meer, …, A. M. Mommaas. 2006. Ultrastructure and origin of membrane vesicles associated with the severe acute respiratory syndrome coronavirus replication complex. *J. Virol.* 80:5927–5940.
7. Snijder, E. J., P. J. Bredenbeek, …, A. E. Gorbalenya. 2003. Unique and conserved features of genome and proteome of SARS-coronavirus, an early split-off from the coronavirus group 2 lineage. *J. Mol. Biol.* 331:991–1004.
8. Thiel, V., K. A. Ivanov, …, J. Ziebuhr. 2003. Mechanisms and enzymes involved in SARS coronavirus genome expression. *J. Gen. Virol.* 84:2305–2315.
9. Kuo, L., K. R. Hurst-Hess, …, P. S. Masters. 2016. Analyses of coronavirus assembly interactions with interspecies membrane and nucleocapsid protein chimeras. *J. Virol.* 90:4357–4368.
10. Grossoehme, N. E., L. Li, …, D. P. Giedroc. 2009. Coronavirus N protein N-terminal domain (NTD) specifically binds the transcriptional regulatory sequence (TRS) and melts TRS-cTRS RNA duplexes. *J. Mol. Biol.* 394:544–557.
11. Verheije, M. H., M. C. Hagemeijer, …, C. A. M. de Haan. 2010. The coronavirus nucleocapsid protein is dynamically associated with the replication-transcription complexes. *J. Virol.* 84:11575–11579.
12. Zúñiga, S., J. L. G. Cruz, …, L. Enjuanes. 2010. Coronavirus nucleocapsid protein facilitates template switching and is required for efficient transcription. *J. Virol.* 84:2169–2175.
13. Chang, C.-K., Y.-L. Hsu, …, T.-H. Huang. 2009. Multiple nucleic acid binding sites and intrinsic disorder of severe acute respiratory syndrome coronavirus nucleocapsid protein: implications for ribonucleocapsid protein packaging. *J. Virol.* 83:2255–2264.
14. Surjit, M., B. Liu, …, S. K. Lal. 2004. The nucleocapsid protein of the SARS coronavirus is capable of self-association through a C-terminal 209 amino acid interaction domain. *Biochem. Biophys. Res. Commun.* 317:1030–1036.
15. McBride, R., M. van Zyl, and B. C. Fielding. 2014. The coronavirus nucleocapsid is a multifunctional protein. *Viruses.* 6:2991–3018.
16. Dinesh, D. C., D. Chalupska, …, E. Boura. 2020. Structural basis of RNA recognition by the SARS-CoV-2 nucleocapsid phosphoprotein. *PLoS Pathog.* 16:e1009100.
17. Sola, I., F. Almazán, …, L. Enjuanes. 2015. Continuous and discontinuous RNA synthesis in coronaviruses. *Annu. Rev. Virol.* 2:265–288.

18. Zúñiga, S., I. Sola, …, L. Enjuanes. 2004. Sequence motifs involved in the regulation of discontinuous coronavirus subgenomic RNA synthesis. *J. Virol.* 78:980–994.
19. Chang, C. K., M. H. Hou, …, T. H. Huang. 2014. The SARS coronavirus nucleocapsid protein–forms and functions. *Antiviral Res.* 103:39–50.
20. van Zundert, G. C. P., J. P. G. L. M. Rodrigues, …, A. M. J. J. Bonvin. 2016. The HADDOCK2.2 web server: user-friendly integrative modeling of biomolecular complexes. *J. Mol. Biol.* 428:720–725.
21. Sheng, J., A. Larsen, …, J. W. Szostak. 2014. Crystal structure studies of RNA duplexes containing s(2)U:A and s(2)U:U base pairs. *J. Am. Chem. Soc.* 136:13916–13924.
22. Li, S., W. K. Olson, and X.-J. Lu. 2019. Web 3DNA 2.0 for the analysis, visualization, and modeling of 3D nucleic acid structures. *Nucleic Acids Res.* 47:W26–W34.
23. Olsson, M. H. M., C. R. Søndergaard, …, J. H. Jensen. 2011. PROPKA3: consistent treatment of internal and surface residues in empirical p K a predictions. *J. Chem. Theory Comput.* 7:525–537.
24. Linge, J. P., M. A. Williams, …, M. Nilges. 2003. Refinement of protein structures in explicit solvent. *Proteins.* 50:496–506.
25. de Vries, S. J., M. van Dijk, and A. M. J. J. Bonvin. 2010. The HADDOCK web server for data-driven biomolecular docking. *Nat. Protoc.* 5:883–897.
26. Lu, X.-J. 2020. DSSR-enabled innovative schematics of 3D nucleic acid structures with PyMOL. *Nucleic Acids Res.* 48:e74.
27. Abraham, M. J., T. Murtola, …, E. Lindah. 2015. Gromacs: high performance molecular simulations through multi-level parallelism from laptops to supercomputers. *SoftwareX.* 1–2:19–25.
28. Maier, J. A., C. Martinez, …, C. Simmerling. 2015. ff14SB: improving the accuracy of protein side chain and backbone parameters from ff99SB. *J. Chem. Theory Comput.* 11:3696–3713.
29. Zgarbová, M., M. Otyepka, …, P. Jurečka. 2011. Refinement of the Cornell et al. nucleic acids force field based on reference quantum chemical calculations of glycosidic torsion profiles. *J. Chem. Theory Comput.* 7:2886–2902.
30. Jorgensen, W. L., J. Chandrasekhar, …, M. L. Klein. 1983. Comparison of simple potential functions for simulating liquid water. *J. Chem. Phys.* 79:926–935.
31. Kumar, R., and H. Grubmüller. 2015. do_x3dna: a tool to analyze structural fluctuations of dsDNA or dsRNA from molecular dynamics simulations. *Bioinformatics.* 31:2583–2585.
32. Lu, X. J., and W. K. Olson. 2008. 3DNA: a versatile, integrated software system for the analysis, rebuilding and visualization of three-dimensional nucleic-acid structures. *Nat. Protoc.* 3:1213–1227.
33. Lemkul, A. J. 2018. Scripts and programs: OSF, web https://osf.io/bafn4/.
34. Delano, W. L. 2002. The PyMOL molecular graphics system. DeLano Scientific, San Carlos, CA.
35. Bunker, D. L., B. Garrett, …, G. S. Long. 1974. Discrete simulation methods in combustion kinetics. *Combust. Flame.* 23:373–379.
36. Gillespie, D. T. 1976. A general method for numerically simulating the stochastic time evolution of coupled chemical reactions. *J. Comput. Phys.* 22:403–434.
37. Šponer, J., G. Bussi, …, M. Otyepka. 2018. RNA structural dynamics as captured by molecular simulations: a comprehensive overview. *Chem. Rev.* 118:4177–4338.
38. Marin-Gonzalez, A., J. G. Vilhena, …, R. Perez. 2019. Sequence-dependent mechanical properties of double-stranded RNA. *Nanoscale.* 11:21471–21478.
39. Masliah, G., P. Barraud, and F. H. T. Allain. 2013. RNA recognition by double-stranded RNA binding domains: a matter of shape and sequence. *Cell. Mol. Life Sci.* 70:1875–1895.
40. Krug, R. M. 2014. Viral proteins that bind double-stranded RNA: countermeasures against host antiviral responses. *J. Interferon Cytokine Res.* 34:464–468.
41. Lu, X.-J., and W. K. Olson. 2003. 3DNA: a software package for the analysis, rebuilding and visualization of three-dimensional nucleic acid structures. *Nucleic Acids Res.* 31:5108–5121.
42. Keane, S. C., P. Liu, …, D. P. Giedroc. 2012. Functional transcriptional regulatory sequence (TRS) RNA binding and helix destabilizing determinants of murine hepatitis virus (MHV) nucleocapsid (N) protein. *J. Biol. Chem.* 287:7063–7073.
43. Kang, S., M. Yang, …, S. Chen. 2020. Crystal structure of SARS-CoV-2 nucleocapsid protein RNA binding domain reveals potential unique drug targeting sites. *Acta Pharm. Sin. B.* 10:1228–1238.
44. Zeng, W., G. Liu, …, T. Jin. 2020. Biochemical characterization of SARS-CoV-2 nucleocapsid protein. *Biochem. Biophys. Res. Commun.* 527:618–623.
45. Lo, C. Y., T. L. Tsai, …, H. Y. Wu. 2019. Interaction of coronavirus nucleocapsid protein with the 5′- and 3′-ends of the coronavirus genome is involved in genome circularization and negative-strand RNA synthesis. *FEBS J.* 286:3222–3239.
46. Larkin, M. A., G. Blackshields, and D. G. Higgins. 2007. Clustal W and Clustal X version 2.0. *Bioinformatics.* 23:2947–2948.
47. Baker, N. A., D. Sept, and J. A. McCammon. 2001. Electrostatics of nanosystems: Application to microtubules and the ribosome. *Proc. Natl. Acad. Sci. U S A.* 98:10037–10041.
48. Dolinsky, T. J., P. Czodrowski, and N. A. Baker. 2007. PDB2PQR: expanding and upgrading automated preparation of biomolecular structures for molecular simulations. *Nucl. Acids Res.* 35 (Web server issue):W522–W525.

Biophysical Journal, Volume *120*

Supplemental information

Dynamics of the SARS-CoV-2 nucleoprotein N-terminal domain triggers RNA duplex destabilization

Ícaro P. Caruso, Karoline Sanches, Andrea T. Da Poian, Anderson S. Pinheiro, and Fabio C.L. Almeida

Dynamics of the SARS-CoV-2 nucleoprotein N-terminal domain triggers RNA duplex destabilization

Ícaro P. Caruso[1,2,*], Karoline Sanches[1,2], Andrea T. Da Poian[2], Anderson S. Pinheiro[3], Fabio C. L. Almeida[2,*]

[1]Multiuser Center for Biomolecular Innovation (CMIB) and Department of Physics, Institute of Biosciences, Letters and Exact Sciences (IBILCE), São Paulo State University (UNESP), 15054-000, São José do Rio Preto, SP, Brazil;

[2]Institute of Medical Biochemistry Leopoldo de Meis (IBqM) and National Center for Structural Biology and Bioimaging (CENABIO), Federal University of Rio de Janeiro (UFRJ), 21941-590, Rio de Janeiro, RJ, Brazil;

[3]Department of Biochemistry, Institute of Chemistry, Federal University of Rio de Janeiro (UFRJ), 21941-590, Rio de Janeiro, RJ, Brazil.

[*]Corresponding authors e-mail address: falmeida@bioqmed.ufrj.br

icaro.caruso@unesp.br

Tel.: +55-21-31042326

Tel.: +55-17-32212828

SUPPLEMENTARY MATERIAL

Modeling the dsRNA melting activity

We used the software Kinetiscope (http://hinsberg.net/kinetiscope/), which is based on a stochastic algorithm developed by Bunker (1) and Gillespie (2). We used the elementary rate constants for individual chemical steps to produce an absolute time base (Figure 6A). The starting condition mimics exactly the experimental condition, varying the concentration of N-NTD over 50 nM dsRNA (dsTRS). The predictions were validated by direct comparison to the experimental data (3).

To simulate the melting curve, we had to constrain the kinetic space, which is large because each model is composed by 6 reactions and 12 individual rate constants, assuming the following boundaries: (B1) the kinetic model must be complete, complying all possible reactions for a given mechanism; (B2) the presence of N-NTD must lead to catalysis, with the melting of dsRNA being faster than the annealing reaction; (B3) the equilibrium of the annealing is shifted toward the dsRNA; and (B4) the equilibrium for the melting activity must be reached in less than 133 seconds, as described by Grossoehme et al. (3).

The criterion for choosing the rate constants for the annealing reaction (R1, Figure 6) was that it must be significantly slower than the melting activity (catalysis). As to our knowledge there is no experimental kinetic rate constant available for the annealing of dsTRS, we fixed a $k_{off} = 8\times10^{-4}\cdot s^{-1}$ for the simulations, which is the experimental value of the dissociation rate constant observed for the almost inactive Y127A N-NTD+SR mutant (3). This mutant has a melting activity of hours, 30 fold slower than the wild-type (3), while our simulation showed melting activities of tens of seconds (Figure 6B). To yield an equilibrium shifted toward the dsRNA, we used $k_{on} = 4\times10^{-1}\ M^{-}1\cdot s^{-1}$, which is true below

the melting temperature of the dsRNA. Any values of k_{off} < 1 s^{-1}, with an association constant K_a, gives the same molar fraction of dsRNA.

We constrained the binding reactions R2 and R3 of N-NTD to the sense (TRS) and antisense (cTRS) single-stranded RNA (ssRNA) (Figure 6A) based on the published experimental values for these association constants (3, 4). Since these values were very similar, to simplify the simulation, we used the same K_a for both reactions ($K_a = 4\times10^7$ M^{-1}). Note that $k_{on} < 10^6$ $M^{-1}\cdot s^{-1}$ makes the reaction too slow to reach equilibrium, violating the boundary B4 (Figures S14A and S16B).

For dsRNA (dsTRS) binding, there was no experimental data to constrain the simulation. However, simulations unambiguously showed that K_a for reaction R4 must be of the same order of that for ssRNAs, leading to the allowed ranges depicted in Figure 6A. We also determined k_{on} based on the simulations, taking boundaries B2 and B4 into consideration, which were also considered for reactions from R1 to R3 (Figure S16B, S17A and S18B). All the constraints applied to reactions from R1 to R4 are valid for both kinetic models (models 1 and 2). Conversely, reactions R5 and R6 are specific for each kinetic model, being essential to comply with boundary B1.

For model 1, there is no experimental data available to constrain reactions R5 and R6, but the simulations showed that they are tightly related to reactions R2 and R3, being both K_a and k_{off} of the same order of magnitude for reactions R2 and R3 (Figure S16C). Note that there is an intricate relationship between the formation of ssRNA-bound states (C2 and C3) and the decrease of free or bound dsRNA (dsTRS and C4). To illustrate this relationship, Figure 6B shows the kinetics at three concentrations of N-NTD. The simulated melting curves for model 1 resembled the near exponential decay observed experimentally (Figure 6C, left). Interestingly, when k_{off} of reactions R5 and R6 were bigger than k_{off} for

reactions R2 and R3, we observed a plateau in the exponential decay of the dsRNA melting curve (Figure 6C). Remarkably, melting curves that either decayed to zero or reached a plateau was observed experimentally, as mentioned before (3). It is worth mentioning that the kinetic model 1 is fully compatible with the experimental data by Grossoehme et al. (2009) (3), as well as with the triggering event suggested by the MD simulations, in which one N-NTD can initiate dsRNA melting, destabilizing the WC base-pairing.

We also evaluated the kinetic model 2, in which a sandwich of 2 N-NTD and 1 dsRNA is necessary for the melting reaction. This stoichiometry for N-NTD melting activity should be considered, since the full-length N protein is a biologically functional dimer and the recognition of the TRS duplex by the two N-NTD subunits for the melting activity is possible. In this model, a sandwich of two N-NTDs and one dsRNA is formed, and the final products are each N-NTD bound to TRS and cTRS ssRNA.

To build a kinetic model that would exclusively produce ssRNA from the sandwiched dsRNA, we had to replace reactions R5 and R6 of kinetic model 1. In this new model, reaction R5 forms the sandwiched dsRNA (C5, Figure 6A) and reaction R6 is the dissociation of C5 into the ssRNA-bound N-NTDs (C2 and C3, Figure 6A). To simulate N-NTD melting activity considering model 2, we used the same boundaries described earlier (B1, B2, B3 and B4), with reactions from R1 to R4 having almost the same constraints described for the model 1.

Reaction R5 and R6 of the model 2 has no parallel to any other reaction. We scanned all the kinetic space that led to the catalysis of melting activity and observed two contrasting situations. The first is when reaction R6 equilibrium is between 10^{-6} and 10^{7} M^{-1}, always having the dissociated forms C2 and C3 available and making the melting curve very stiff (model 2a). The second is the opposite situation, where equilibrium is skewed

toward the sandwich state (C5) with $K_a > 10^7$ M^{-1} (model 2b). Figure 6C illustrates the melting curves obtained for the two situations.

Model 2a is characterized for the high efficiency in the dissociation of the dsRNA, k_{on} and k_{off} can assume any value (*n* and *m*, Figure 6A) as long as K_a is between 10^{-6} to 10^7 M^{-1}. Particularly for model 2a, the kinetic of dsRNA melting is also independent of k_{on} for reactions R2 and R3, at fixed concentrations of N-NTD. For R5, the equilibrium should be shifted toward C5, to keep up with boundaries B2 and B4 ($K_a > 1$, Figure S17B). All simulated conditions led to the curve in red (Figure 6C), in which, the minimal amount of N-NTD (10 nM) led to complete dissociation of the dsRNA (molar fraction of zero). Figure S17 illustrates all the simulated boundaries. Note that for the model 2a there is never an accumulation of C5 (Figure S17C).

Model 2b corresponds to when the equilibrium of reaction R6 is shifted toward C5 ($K_a > 10^7$ M^{-1}). For R5, we determined that k_{on} has to be $> 10^7$ s^{-1} to keep up with boundaries B2 and B4. For the melting activity to take place, the equilibrium of reaction R5 was skilled toward C5 ($K_a > 10^7$ M^{-1}, Figure S18C). Figure S18 illustrates the reaction boundaries. In this situation, we were able to observe a melting curve (Figure 6C, blue) with a near exponential decay at a low concentration of N-NTD and a near exponential rise at higher concentrations of N-NTD. This behavior is explained by the accumulation of C5 and N-NTD concentration-dependent mutual compensation of C5 and dsRNA. Note how K_a modulates the accumulation of C5, transitioning between models 2a and 2b (Figure S18D). The increase in the concentration of N-NTD led to a decrease in dsRNA forming C2, C3 and free ssRNA. Further increase in N-NTD led to a decrease in dsRNA and a compensating increase in C5. None of the situations simulated for model 2 are parallel to the experimental observation.

TRS-L	**UUCUC-UAAACGAAC**
TRS-B S	ACAAC-UAAACGAAC
TRS-B ORF3a	UACACAUAAACGAAC
TRS-B E	UUGUA-AGCACAAGC
TRS-B M	UGGUC-UAAACGAAC
TRS-B ORF6	UACAG-UAAGUGACA
TRS-B ORF7a	UUGAU-UAAACGAAC
TRS-B ORF7b	CACUC-AAAAGAAAG
TRS-B ORF8	ACGCC-UAAACGAAC
TRS-B N	UCAUC-UAAACGAAC
TRS-B ORF9b	CAAAC-UAAAAUGUC
TRS-B ORF14	UACAC-CAAAAGAUC
TRS-B ORF10	AGGCC-UAAACUCAU

Figure S1. Pairwise alignment of the TRS-B sequences of each SARS-CoV-2 ORF (NCBI reference: NC_045512.3) with that of TRS-L performed by ClustalW2 (5). The bold sequence denotes the sequence used in this work.

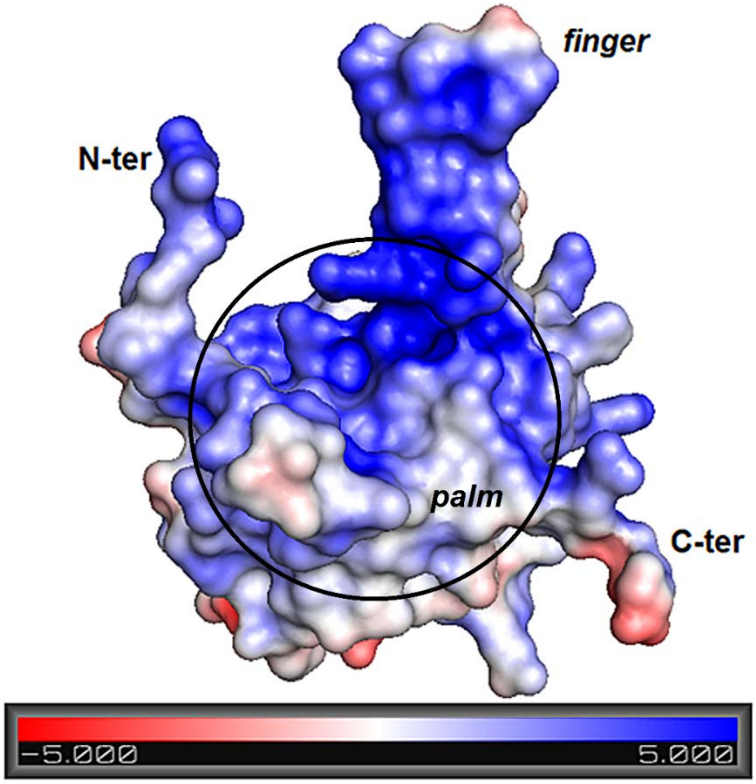

Figure S2. Electrostatic potential surface of SARS-CoV-2 N-NTD calculated from APBS software (6) using charge values and protonation states determined by PDB2PQR server (7) along with PROPKA program (pH 7.0, 50 mM NaCl, 25 °C) (8). The bar denotes the electrostatic potential range from –5 (red) to +5 kTe^{-1} (blue). The electrostatic potential surface of N-NTD was displayed using PyMOL (9).

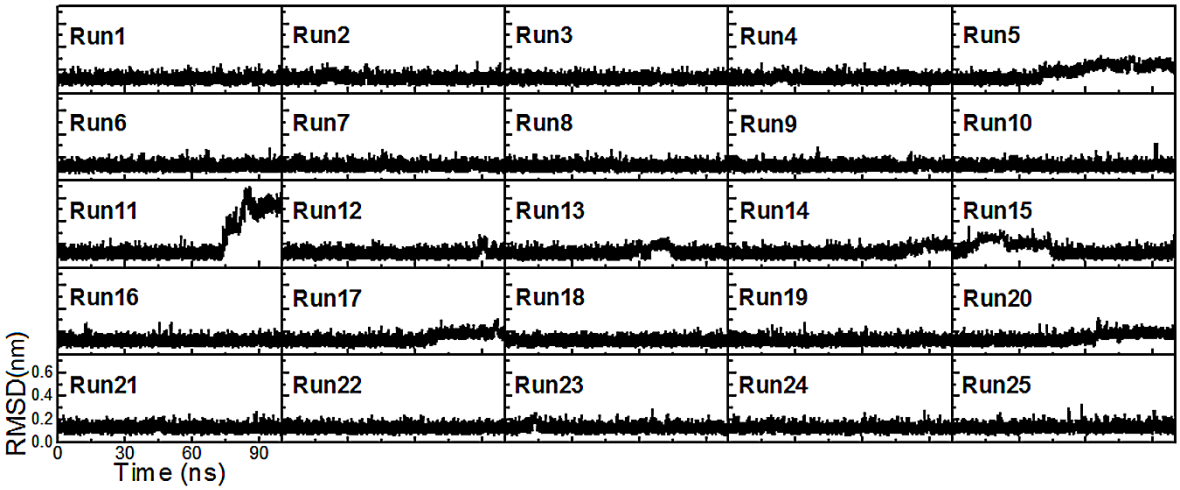

Figure S3. RMSD values of the backbone atoms of free dsTRS for the 25 replicas of 100 ns MD simulations.

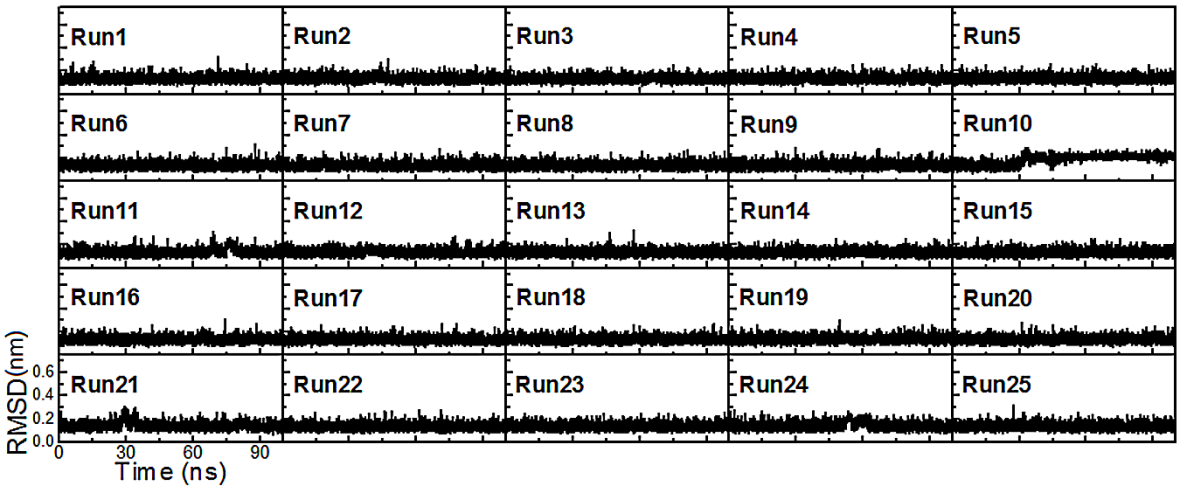

Figure S4. RMSD values of the backbone atoms of free dsNS for the 25 replicas of 100 ns MD simulations.

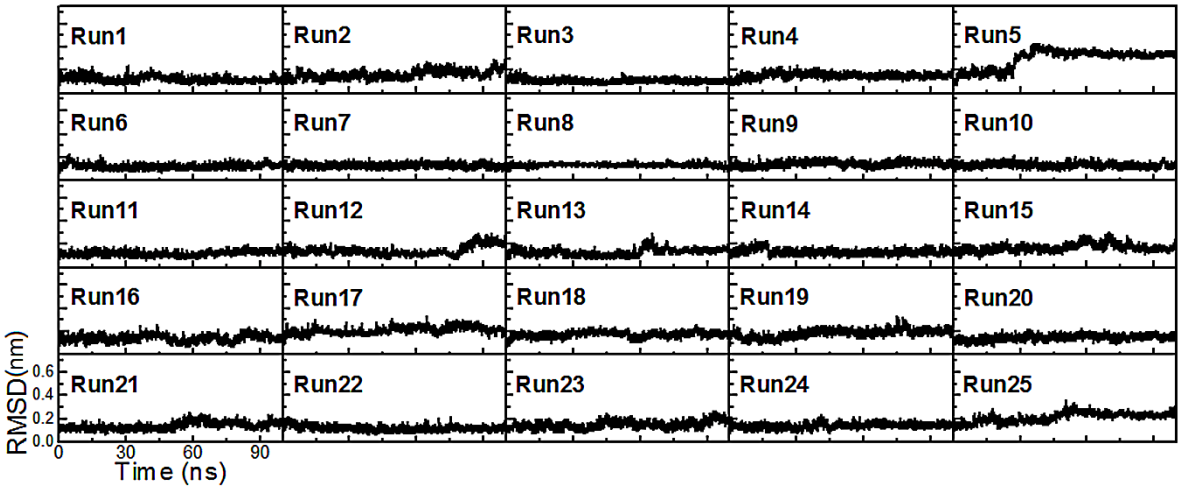

Figure S5. RMSD values of the backbone atoms of N-NTD-bound dsTRS for the 25 replicas of 100 ns MD simulations.

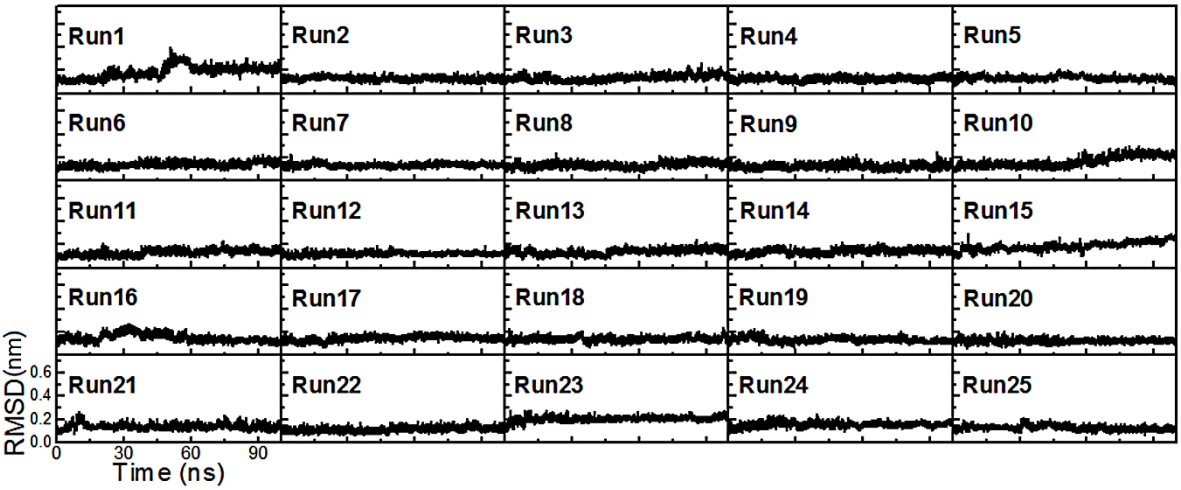

Figure S6. RMSD values of the backbone atoms of N-NTD-bound dsNS for the 25 replicas of 100 ns MD simulations.

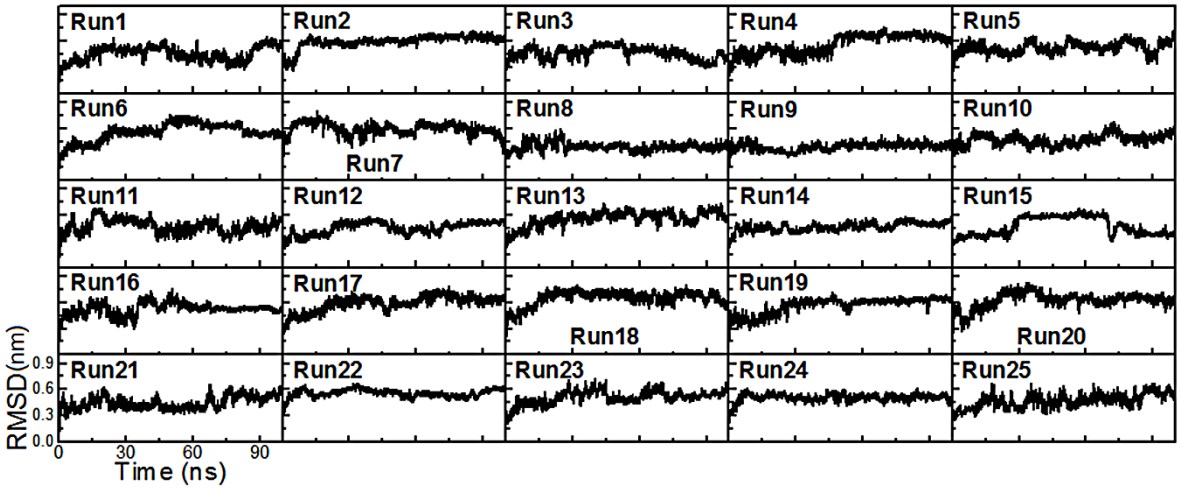

Figure S7. RMSD values of the backbone atoms of free N-NTD for the 25 replicas of 100 ns MD simulations.

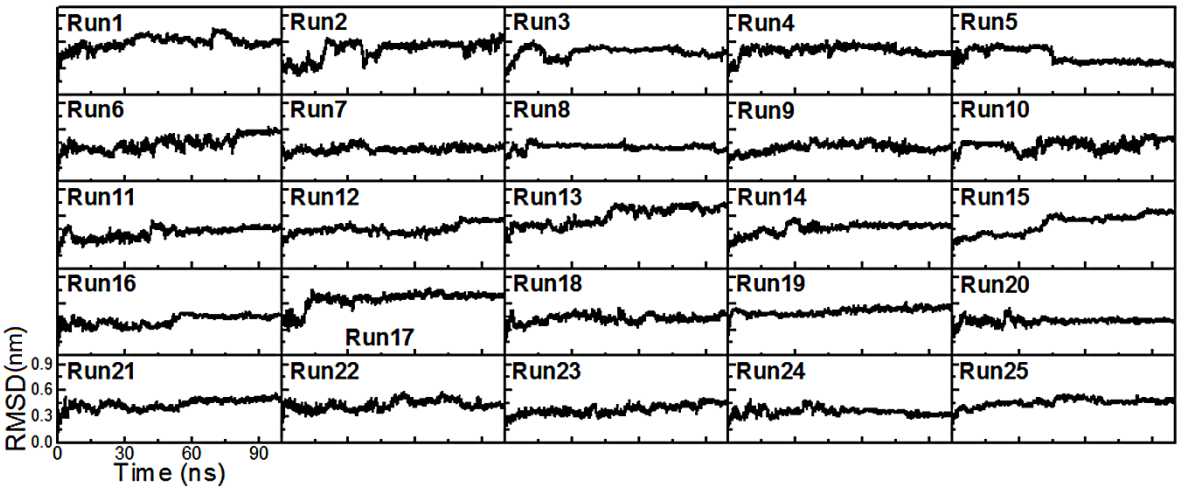

Figure S8. RMSD values of the backbone atoms of dsTRS-bound N-NTD for the 25 replicas of 100 ns MD simulations.

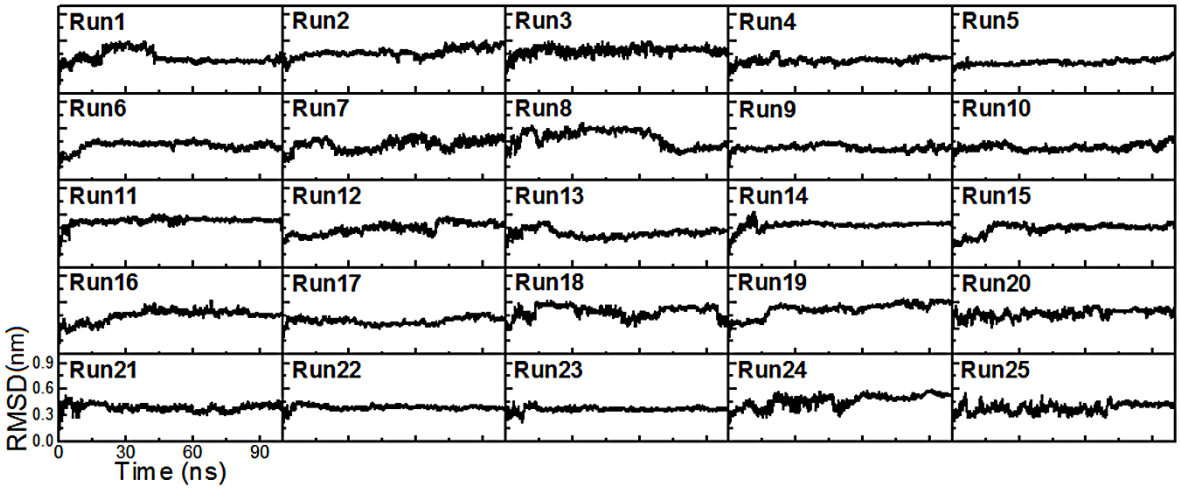

Figure S9. RMSD values of the backbone atoms of dsNS-bound N-NTD for the 25 replicas of 100 ns MD simulations.

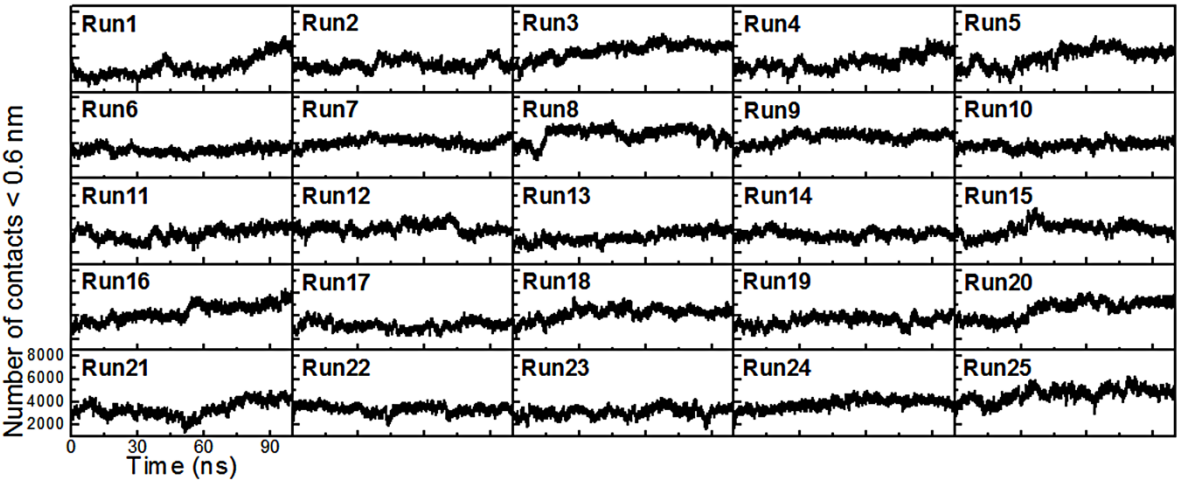

Figure S10. Number of contacts < 0.6 nm between the N-NTD and dsTRS atoms for the 25 replicas of 100 ns MD simulations.

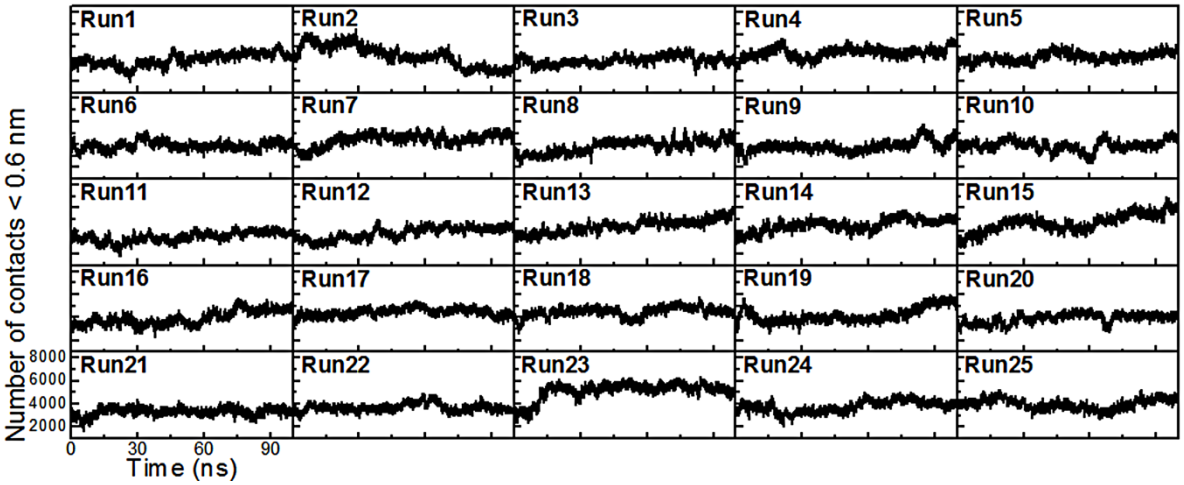

Figure S11. Number of contacts < 0.6 nm between the N-NTD and dsNS atoms for the 25 replicas of 100 ns MD simulations.

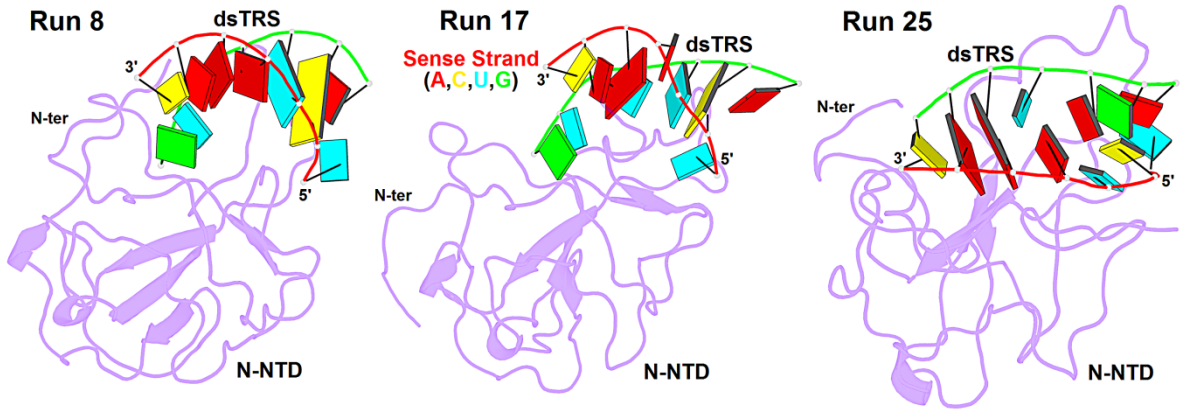

Figure S12. Structural model of the N-NTD:dsTRS complex representative of the MD simulation for runs 8, 17, and 25. The protein is shown as purple cartoon and dsTRS is denoted as ribbon model with nitrogenous bases and base-pairing as colored squares and rectangles, respectively. The color of the squares corresponds to the type of nitrogenous base, being A: red, C: yellow, U: cyan, and G: green. The color of the rectangles refers to the color of the nitrogenous base of the sense RNA strand.

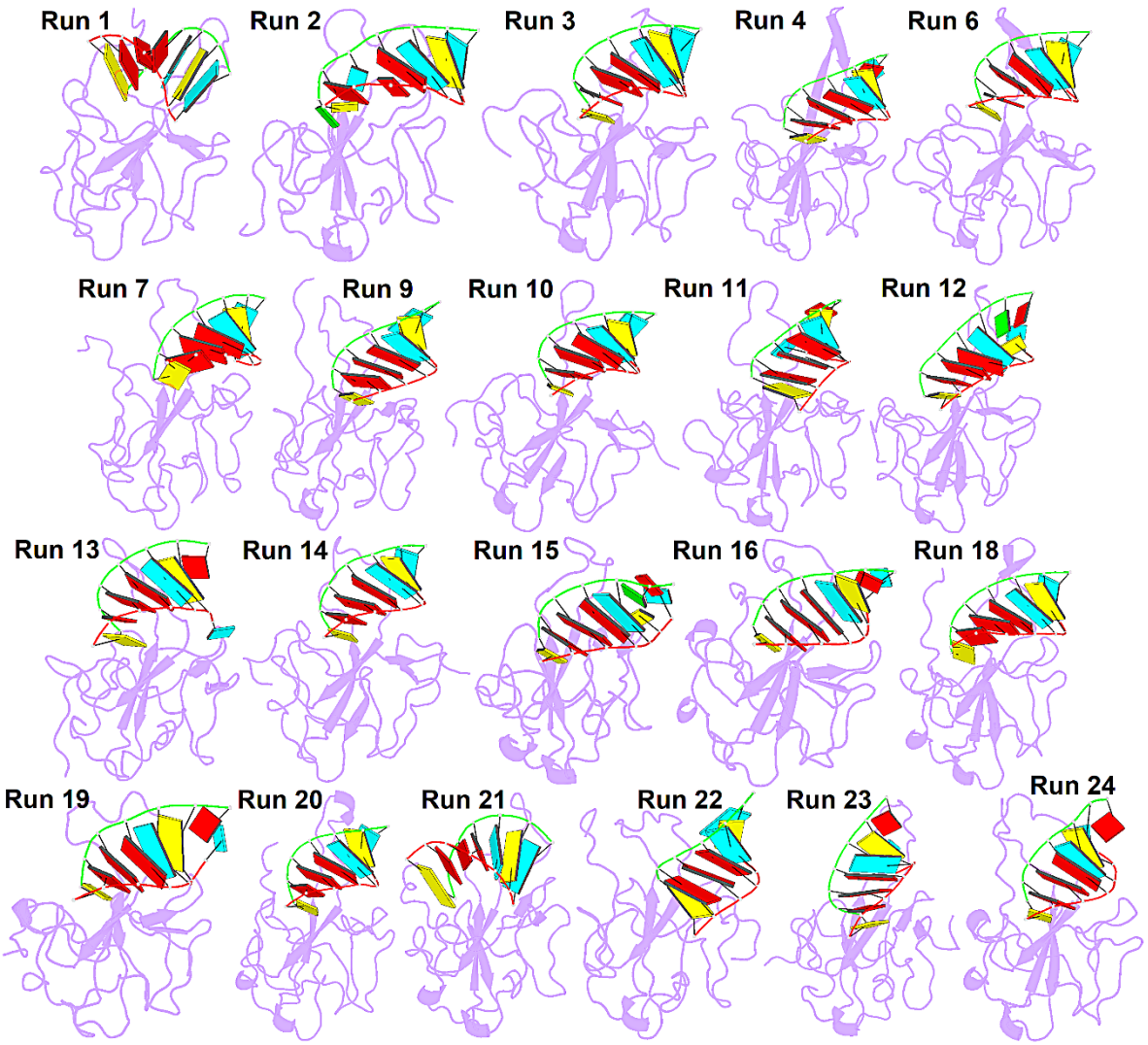

Figure S13. Structural model of the N-NTD:dsTRS complex of the MD simulations (last frames) for the runs that had no significant break of protein-nitrogenous base hydrogen bonds. The protein is shown as purple cartoon and dsTRS is denoted as ribbon model with nitrogenous bases and base-pairing as colored squares and rectangles, respectively. The color of the squares corresponds to the type of nitrogenous base, being A: red, C: yellow, U: cyan, and G: green. The color of the rectangles refers to the color of the nitrogenous base of the sense RNA strand. The protein structure representation is equally oriented in all runs, placing the N- and C-termini to the left and right, respectively, and the finger at the top.

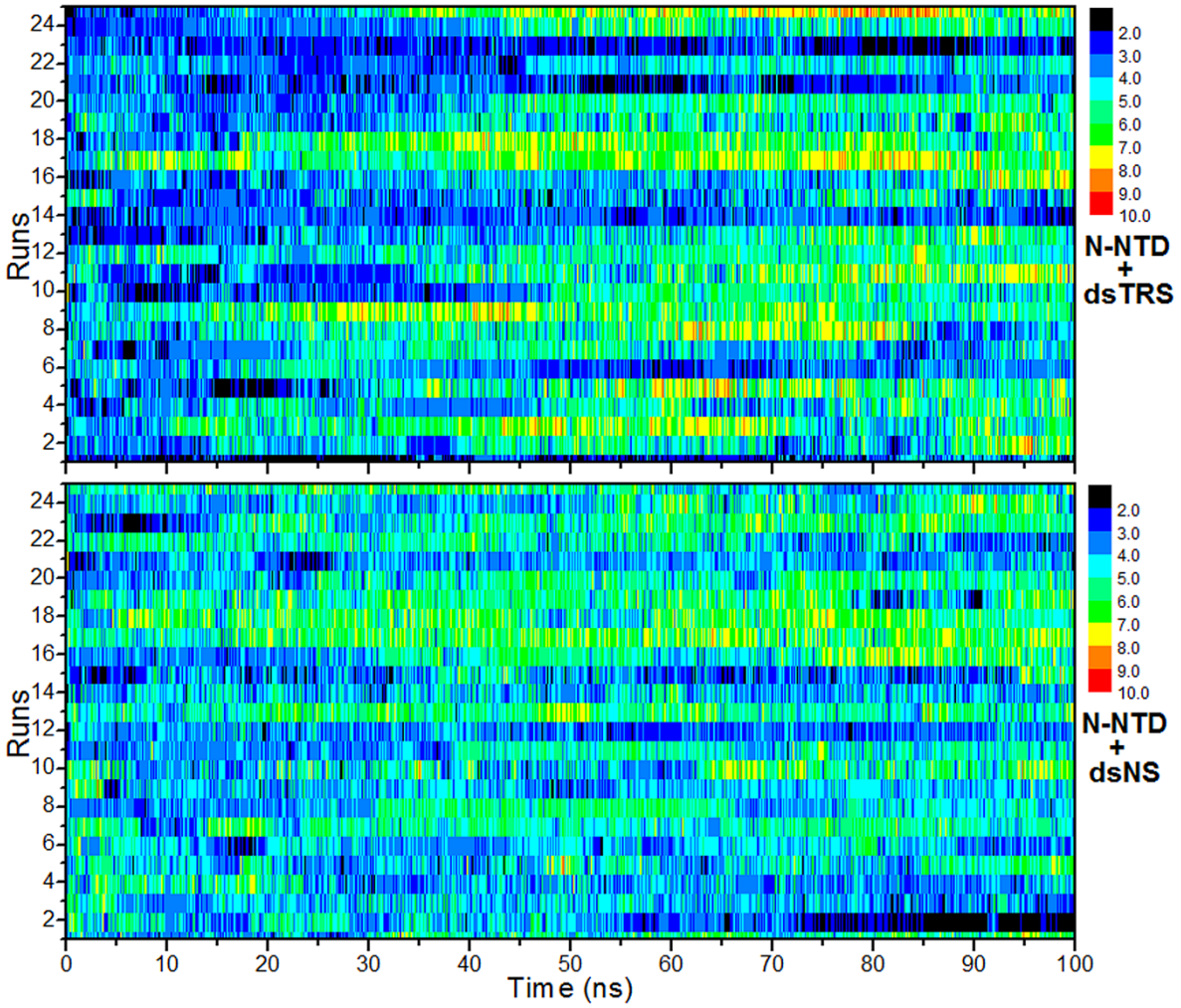

Figure S14. Number of intermolecular hydrogen bonds formed between the nitrogenous bases of the dsRNAs (dsTRS in top and dsNS in bottom) and N-NTD over the 100 ns simulations for the 25 MD replicas. The color bar denotes the correspondence between the color code and the number of intermolecular hydrogen bonds.

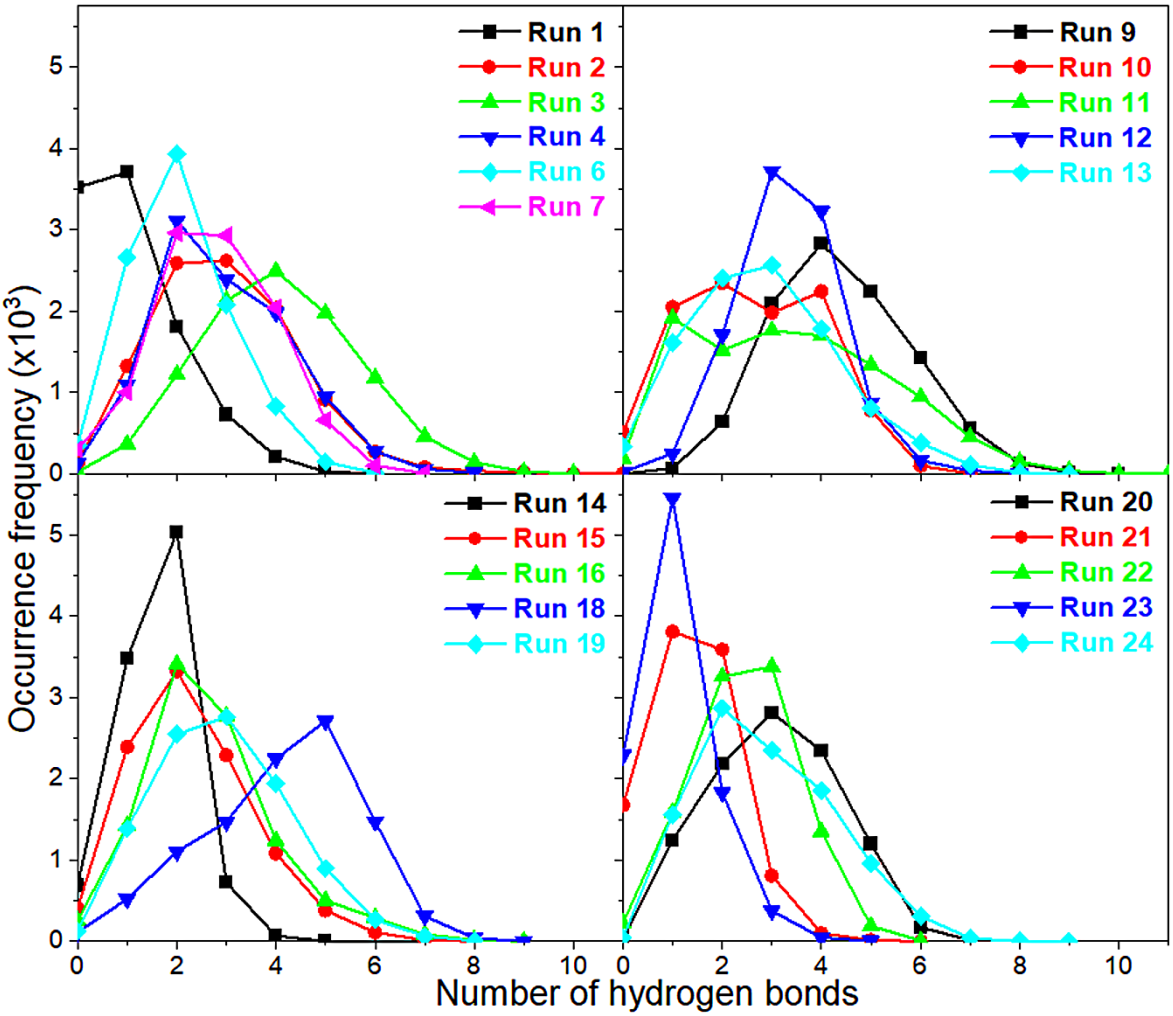

Figure S15. Distribution of the occurrence frequency of the number of hydrogen bonds between the nitrogenous bases of dsTRS and N-NTD along the 100 ns MD simulations.

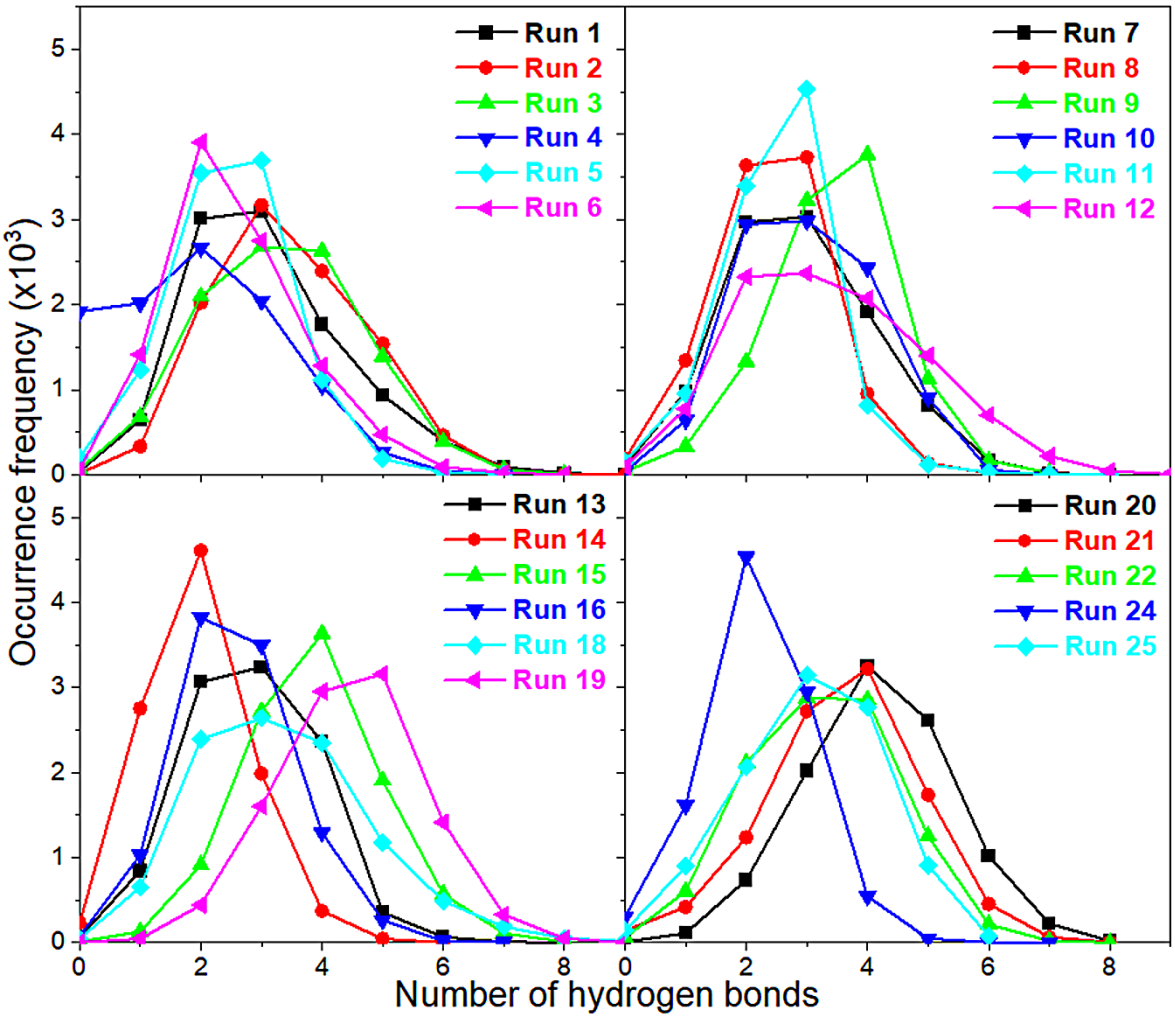

Figure S16. Distribution of the occurrence frequency of the number of hydrogen bonds between the nitrogenous bases of dsNS and N-NTD along the 100 ns MD simulations.

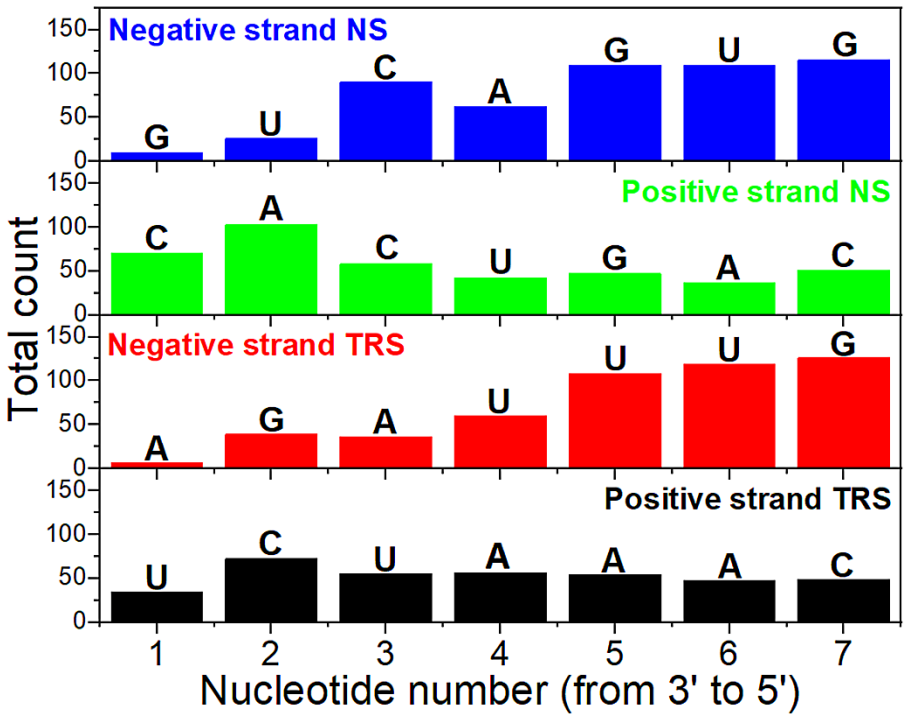

Figure S17. Total count of protein-RNA hydrogen bonds with persistency higher than 10% as a function of the residue number for 25 replicas along the 100 ns MD simulations.

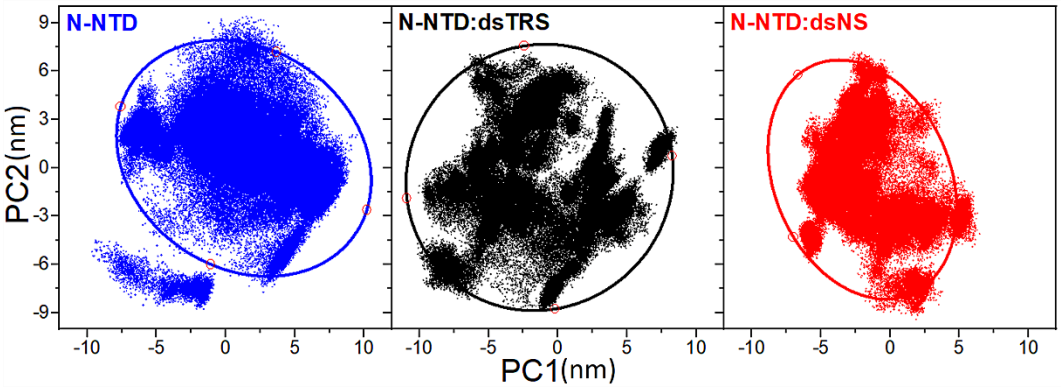

Figure S18. PCA scatter plots PC1 and PC2 for free N-NTD (blue dots – *left*) and for N-NTD complexed with either TRS (black dots – *middle*) or NS (red dots – *right*) dsRNAs, using the trajectories of all 25 replicas of free N-NTD concatenated with its bound states. The extent of the conformational space for each scatter plot was measured by fitting an elliptical shell (solid lines) that contains 95% of the density.

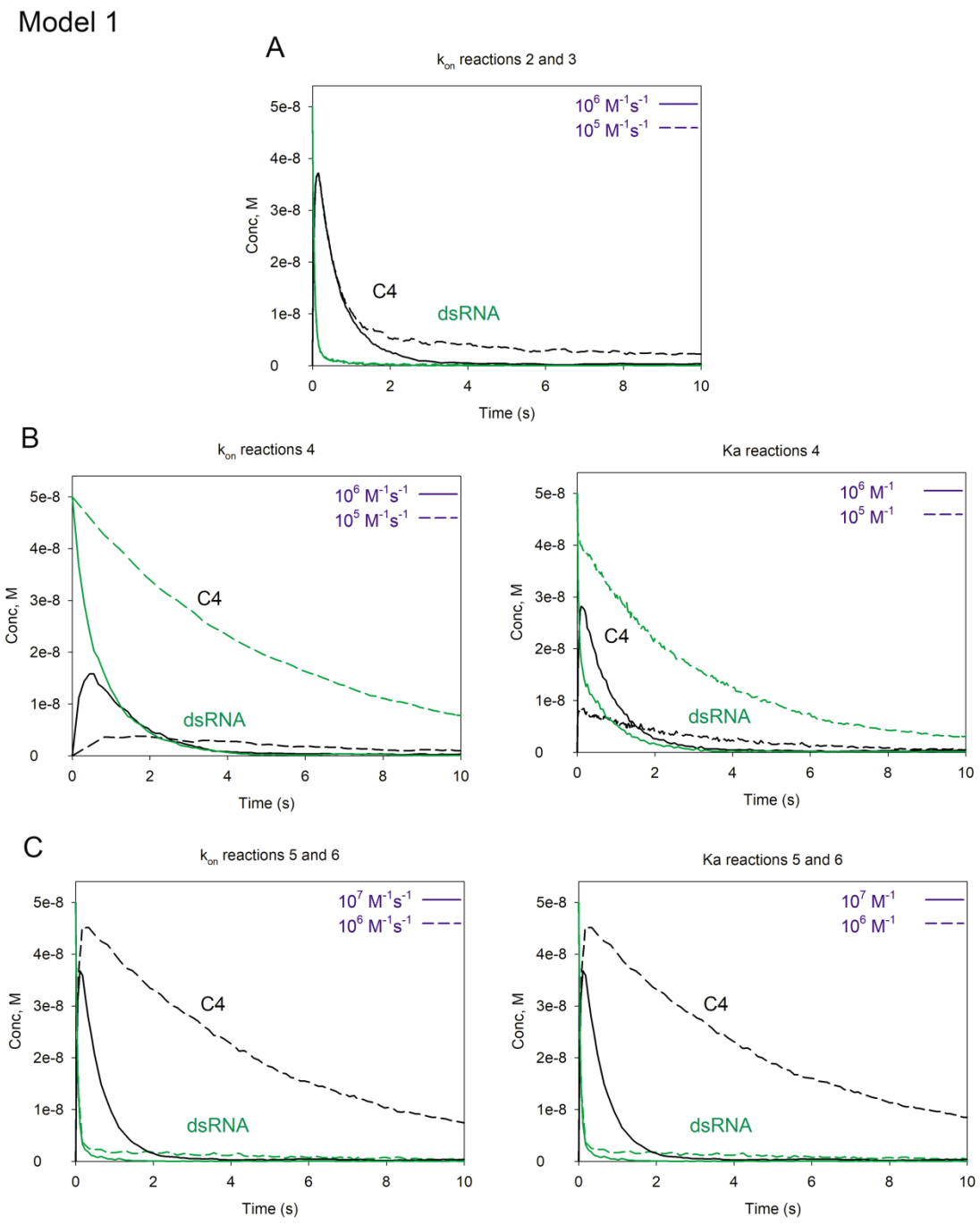

Figure S19. Simulations of the reactions progression for the validation of the ranges described in Figure 6A for model 1. A) Effect of the variation of k_{on} in reaction R2 and R3. Note that $k_{on} < 10^6$ $M^{-1}s^{-1}$ makes the reaction too slow to reach equilibrium, violating boundary B4. B) Effect of the variation of k_{on} (left) and K_a (right) in reaction R4. Note that $k_{on} < 10^6$ $M^{-1}s^{-1}$ or $K_a < 10^6$ M^{-1} make the reaction too slow to reach equilibrium, violating boundary B4. C) Effect of the variation of k_{on} (left) and K_a (right) in reactions R5 and R6. Note that $k_{on} < 10^6$ $M^{-1}s^{-1}$ or $K_a < 10^6$ M^{-1} make the reaction too slow to reach equilibrium, violating boundary B4. For model 1 simulations, we used the following reaction rates:

(R1) k_{on} = 4×10^{-1} M^{-1}s^{-1} and k_{off} = 8×10^{-4} s^{-1}; (R2, R3) k_{on} = 4×10^{7} M^{-1}s^{-1} and k_{off} = 1 s^{-1}; (R4) k_{on} = 1×10^{7} M^{-1}s^{-1} and k_{off} = 1 s^{-1}; (R5, R6) k_{on} = 4×10^{7} M^{-1}s^{-1} and k_{off} = 1 s^{-1} (red).

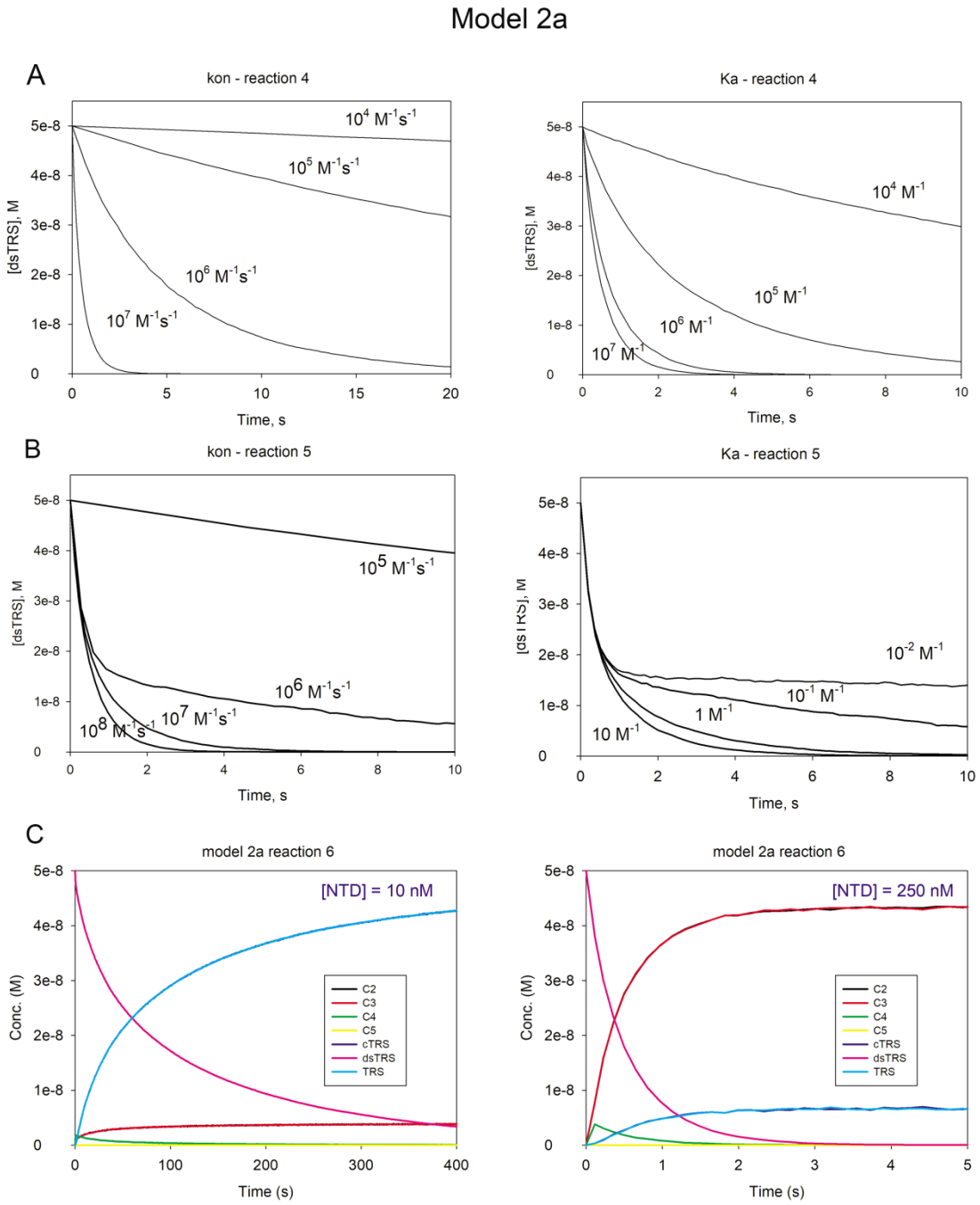

Figure S20. Simulations of the reactions progression for the validation of the ranges described in Figure 6A for model 2a. A) Effect of the variation of k_{on} (left) and K_a (right) in reaction R4. Note that k_{on} < 10^{6} M^{-1}s^{-1} or K_a < 10^{5} M^{-1} make the reaction too slow to reach equilibrium, violating boundary B4. B) Effect of the variation of k_{on} (left) and K_a (right) in reaction R5. Note that k_{on} < 10^{7} M^{-1}s^{-1} or K_a < 1 M^{-1} make the reaction too slow to reach

equilibrium, violating boundary B4. C) Time course of the reaction R6 for each of the components. For model 2a, for $10^{7} > K_a > 10^{-6}$ M^{-1}, there is never accumulation of C5, resulting in a kinetic of dsRNA melting independent of k_{on} and k_{off} at fixed concentrations of N-NTD. The kinetics changes considerably with the [N-NTD] as showed in the figure. For values of $K_a > 10^{7}$ M^{-1} we observed the transition to model 2b with accumulation of C5. Note that for reactions R2 and R3, K_a was determined experimentally (4×10^{7} M^{-1}). Particularly for model 2a, the kinetic of dsRNA melting is independent of k_{on} and k_{off} of reactions R2 and R3, at fixed concentrations of N-NTD. For model 2a simulations, we used the following reaction rates: (R1) $k_{on} = 4\times10^{-1}$ $M^{-1}s^{-1}$ and $k_{off} = 8\times10^{-4}$ s^{-1}; (R2, R3) $k_{on} = 4\times10^{7}$ $M^{-1}s^{-1}$ and $k_{off} = 1$ s^{-1}; (R4) $k_{on} = 1\times10^{7}$ $M^{-1}s^{-1}$ and $k_{off} = 1$ s^{-1}; (R5) $k_{on} = 1\times10^{8}$ $M^{-1}s^{-1}$ and $k_{off} = 1$ s^{-1} and (R6) $k_{on} = 1\times10^{8}$ $M^{-1}s^{-1}$ and $k_{off} = 1\times10^{-1}$ s^{-1}.

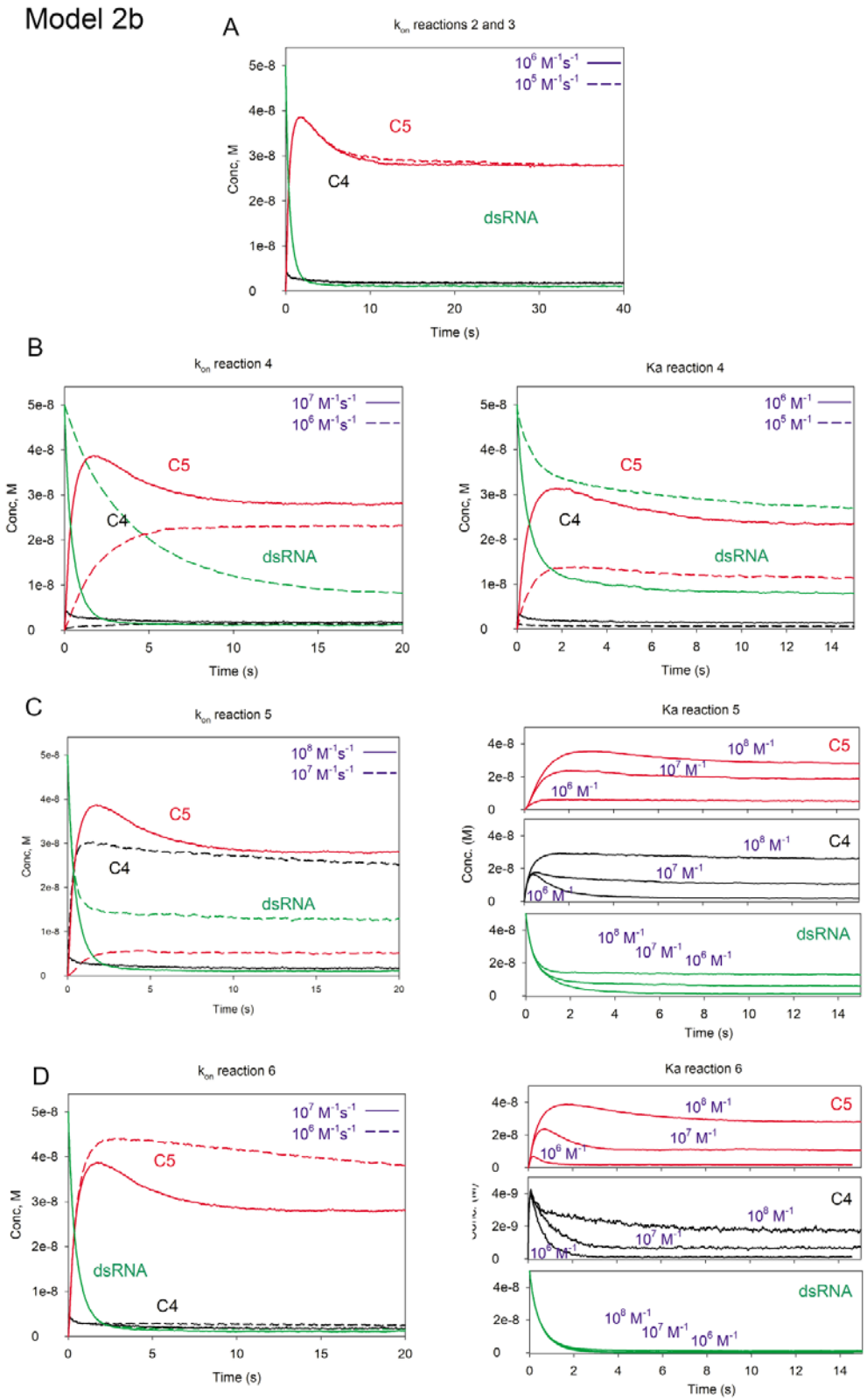

Figure S21. Simulations of the reactions progression for the validation of the ranges described in Figure 6A for model 2b. A) Effect of the variation of k_{on} in reactions R2 and

R3. Note that $k_{on} < 10^6$ $M^{-1}s^{-1}$ makes the reaction too slow to reach equilibrium, violating boundary B4. B) Effect of the variation of k_{on} (left) and K_a (right) in reaction R4. Note that $k_{on} < 10^7$ $M^{-1}s^{-1}$ or $K_a < 10^6$ M^{-1} make the reaction too slow to reach equilibrium, violating boundary B4. C) Effect of the variation of k_{on} (left) and K_a (right) in reaction R5. Note that $k_{on} < 10^7$ $M^{-1}s^{-1}$ or $K_a < 10^7$ M^{-1} make the reaction too slow to reach equilibrium, violating boundary B4. D) Effect of the variation of k_{on} (left) and K_a (right) in reaction R6. Note that $k_{on} < 10^6$ $M^{-1}s^{-1}$ or $K_a < 10^7$ M^{-1} make the reaction too slow to reach equilibrium, violating boundary B4. For model 2b simulations, we used the following reaction rates: (R1) $k_{on} = 4\times10^{-1}$ $M^{-1}s^{-1}$ and $k_{off} = 8\times10^{-4}$ s^{-1}; (R2, R3) $k_{on} = 4\times10^7$ $M^{-1}s^{-1}$ and $k_{off} = 1$ s^{-1}; (R4) $k_{on} = 1\times10^7$ $M^{-1}s^{-1}$ and $k_{off} = 1$ s^{-1}; (R5) $k_{on} = 1\times10^8$ $M^{-1}s^{-1}$ and $k_{off} = 1$ s^{-1} and (R6) $k_{on} = 1\times10^8$ $M^{-1}s^{-1}$ and $k_{off} = 1\times10^{-1}$ s^{-1}.

Table S1. Protein-RNA hydrogen bonds with percentage of persistence higher than 10% for run 1 of the N-NTD:dsTRS complex.

Donor		Acceptor		
Amino acid residue	**Atom**	**Nucleotide residue**	**Atom**	**%Persistence**
TYR69	OH	U9	O1P	89.971
ARG67	NH1	U10	O2P	86.851
ARG67	NH1	U9	O1P	86.201
ARG55	NE	U11	O1P	76.722
ARG67	NH2	U10	O2P	71.003
ARG55	NH2	U11	O1P	69.833
ARG52	NH2	U10	O1P	59.824
GLY59	N	A12	O1P	55.144
ARG52	NH1	U10	O1P	51.005
ARG137	NH2	A5	O2P	48.495
SER11	N	G8	O5'	41.626
GLY57	N	U11	O2P	39.596
ARG137	NH2	A4	O2P	38.366
ARG109	NH2	G8	N7	26.437
ASP58	N	U11	O3'	26.107
G8	O5'	PHE13	O	25.667
LYS60	NZ	G13	O2P	23.258
ARG55	NH2	U10	O3'	23.198
ARG137	NH2	A6	O2P	22.958
ARG137	NH1	A6	O2P	18.528
ARG137	NH1	A5	O2P	18.168
SER136	N	C2	O2P	17.718
ASP58	N	A12	O1P	17.248
U1	O5'	ALA133	O	17.078
GLY57	N	U11	O1P	17.008
ASP58	N	A12	O2P	16.048
ARG137	NH2	U3	O2P	12.999
ARG52	NH1	U9	O3'	12.499
U1	O5'	PHE131	O	11.629
LEU5	N	U9	O2'	11.319
G8	N2	PRO6	O	11.269

LYS60	NZ	A12	O2P	10.889
ARG137	NH2	C2	O1P	10.809
ARG137	NH1	A4	O2P	10.649

Table S2. Protein-RNA hydrogen bonds with percentage of persistence higher than 10% for run 2 of the N-NTD:dsTRS complex.

Donor		**Acceptor**		
Amino acid residue	**Atom**	**Nucleotide residue**	**Atom**	**%Persistence**
ARG137	NH2	A4	O2P	86.341
TYR69	OH	U9	O2P	66.413
TYR132	OH	U3	O2P	65.723
TYR71	OH	G8	O5'	58.024
ARG137	NH2	U3	O1P	57.834
ARG52	NH2	U10	O1P	51.605
ARG52	NE	U10	O2P	49.785
ARG67	NH2	U10	O4	46.965
GLY20	N	C2	O1P	46.155
LYS62	NZ	G13	O6	45.335
SER65	OG	C2	O2P	43.236
ARG67	NH1	U10	O4	38.716
SER11	N	G8	O5'	37.536
ARG137	NH1	U3	O1P	35.976
ARG52	NH1	U9	O1P	35.806
A5	N6	GLU134	OE2	33.877
ARG137	NE	A4	O2P	32.117
SER11	N	G8	O4'	29.037
ARG52	NH2	U10	O2P	25.507
ARG137	NH2	U3	O5'	23.388
LYS60	NZ	G13	O2P	23.138
A5	N6	GLU134	OE1	22.968
ARG52	NH2	U9	O2P	19.138
GLY57	N	U11	O2P	17.598
ARG52	NH1	U9	O2P	16.108
ARG137	NE	A4	O1P	15.588
ARG137	NH2	U3	O2P	15.048
ARG137	NH1	U3	O2P	14.099
ALA15	N	G8	O6	14.009
GLY57	N	U11	O1P	13.279
LYS62	NZ	G13	N7	13.209
SER65	OG	U1	O5'	11.659
ARG52	NH2	U9	O1P	10.929
SER11	N	G8	N7	10.819
ARG52	NH2	U9	O5'	10.499
A6	N6	GLU134	OE2	10.199

Table S3. Protein-RNA hydrogen bonds with percentage of persistence higher than 10% for run 3 of the N-NTD:dsTRS complex.

Donor		Acceptor		
Amino acid residue	**Atom**	**Nucleotide residue**	**Atom**	**%Persistence**
ARG137	NH2	A4	O2P	91.731
G8	N2	PRO111	O	88.321
ARG67	NH2	C2	O2P	84.022
U1	O5'	SER65	O	76.312
ARG52	NH1	U10	O2P	75.722
ARG52	NH1	U9	O1P	69.693
ARG137	NH2	U3	O1P	63.674
SER11	N	G8	O4'	62.444
ARG109	NH1	G8	N3	60.694
ARG52	NH2	U10	O2P	60.364
ARG137	NH1	U3	O1P	57.674
ARG67	NE	C2	O2P	56.654
ARG109	NH2	G8	N2	51.885
TYR132	OH	U3	O2P	49.315
GLY57	N	G13	N7	48.295
ARG55	NH2	U9	O2P	39.746
GLY57	N	G13	O6	35.236
ARG55	NH2	U10	O2P	30.607
ARG55	NH1	U10	O2P	28.607
ASN114	N	C7	O2'	25.517
ARG137	NE	A4	O2P	25.027
ARG55	NH1	U9	O2P	24.278
ALA116	N	G8	O6	23.448
C7	O2'	ALA112	O	22.748
LYS62	NZ	U1	O4	19.228
ARG137	NH2	U3	O5'	18.558
C2	N4	ARG55	O	18.248
ARG67	NH2	C2	O5'	16.658
ASN8	ND2	U9	O1P	14.839
TYR71	OH	G8	O5'	14.509
A12	N6	ARG55	O	14.279
ARG137	NH2	U3	O2P	12.839
SER11	N	G8	O5'	12.339
SER140	OG	A5	O1P	11.689
ARG52	NH2	U9	O1P	10.969
ARG52	NH1	U9	O2P	10.769

Table S4. Protein-RNA hydrogen bonds with percentage of persistence higher than 10% for run 4 of the N-NTD:dsTRS complex.

Donor		Acceptor		
Amino acid residue	**Atom**	**Nucleotide residue**	**Atom**	**%Persistence**
TYR69	OH	U9	O2P	73.193
GLY20	N	C2	O1P	54.375

SER11	N	G8	O5'	52.735
ARG137	NH2	A5	O2P	51.935
A6	N6	GLU134	OE1	51.705
ARG52	NH2	U11	O2P	41.666
ARG137	NH2	A4	O2P	38.346
TYR71	OH	G8	O5'	36.966
ARG137	NE	A5	O2P	36.126
HIS19	NE2	U3	O2P	32.097
ARG67	NH2	U9	O2P	32.037
SER11	N	G8	O4'	31.597
SER65	OG	C2	O2P	30.627
A6	N6	GLU134	OE2	30.107
LYS62	NZ	A14	N7	29.667
U1	O5'	ASP63	O	27.647
A14	N6	ASP63	O	27.547
C7	N4	GLU134	OE2	26.977
GLY20	N	C2	O2P	25.517
HIS19	NE2	U3	O1P	25.117
C7	N4	GLU134	OE1	23.288
SER140	N	A6	O1P	21.028
GLY139	N	A5	O1P	21.008
ARG52	NE	U10	O2P	19.868
ARG67	NE	U9	O2P	19.368
G8	N2	MET3	O	18.938
ARG52	NH1	U11	O2P	18.268
SER140	OG	A6	O1P	18.168
ARG137	NH1	A4	O2P	16.888
ARG52	NH2	U10	O2P	16.198
GLY57	N	G13	O2P	15.368
U9	O2'	ALA2	O	13.789
ARG52	NH1	U10	O2P	13.439
ARG137	NH2	A4	O1P	13.109
ARG67	NH2	U9	O1P	12.069
GLY139	N	A6	O1P	11.709
ARG52	NH2	U10	O1P	10.989
SER140	OG	A5	O1P	10.679
SER140	N	A5	O1P	10.539

Table S5. Protein-RNA hydrogen bonds with percentage of persistence higher than 10% for run 5 of the N-NTD:dsTRS complex.

Donor		**Acceptor**		
Amino acid residue	**Atom**	**Nucleotide residue**	**Atom**	**%Persistence**
A12	N6	ARG53	O	49.125
ARG55	NH2	A12	O2P	45.235
ARG53	NH1	U10	O2P	43.846
GLY138	N	C2	O2P	33.467
ASN8	ND2	G8	O2'	32.547
C2	N4	GLU134	OE2	26.847

ARG55	NH1	U11	O2P	26.437
ARG53	NH2	U11	O2P	26.187
GLY1	N	C7	O2	25.087
ARG53	NH2	U9	O2P	23.678
TYR69	OH	U9	O4	21.638
ARG55	NH2	U11	O5'	21.528
ARG55	NH2	A12	O1P	19.128
C2	N4	GLU134	OE1	19.128
ARG137	NH2	U3	O2P	18.888
ARG137	NH1	U3	O2P	18.668
ARG53	NH1	U9	O5'	18.318
GLY135	N	U3	O4	17.818
ASN8	N	G8	N2	17.578
U3	N3	GLU134	OE1	17.448
U1	O5'	ALA133	O	16.808
ARG55	NH2	U11	O2P	16.268
G8	N2	ASN7	OD1	15.448
ARG53	NH1	U9	O2P	15.418
A4	N6	GLU134	OE1	14.829
U1	O5'	SER136	O	13.989
ARG137	NE	C2	O2P	13.969
ARG137	NH1	C2	O2P	13.769
SER11	N	G8	O4'	13.479
ARG55	NH2	U11	O1P	13.169
SER140	OG	C2	O1P	12.949
ARG53	NH2	U10	O2P	12.749
TYR69	OH	U9	O2P	12.669
U3	N3	GLU134	OE2	12.539
ARG53	NH2	U9	O1P	11.959
GLY1	N	U9	O2'	11.909
ARG55	NH1	A12	O2P	11.419
ASN7	ND2	G8	O2'	10.639
ARG137	NH2	C2	O2P	10.619
ARG67	NH2	A4	N1	10.469
LEU5	N	C7	O2	10.379

Table S6. Protein-RNA hydrogen bonds with percentage of persistence higher than 10% for run 6 of the N-NTD:dsTRS complex.

Donor		**Acceptor**		
Amino acid residue	**Atom**	**Nucleotide residue**	**Atom**	**%Persistence**
G8	N2	PRO111	O	86.671
ARG67	NH2	C2	O2P	69.403
ARG52	NH1	U9	O2P	67.093
ASN8	ND2	U9	O1P	61.044
SER11	N	G8	O4'	58.784
ARG137	NH2	U3	O2P	56.054
ARG137	NH1	U3	O1P	54.095
ARG52	NH2	U9	O2P	53.275

G8	O2'	ASN8	OD1	53.085
SER65	N	U1	O5'	48.425
ARG67	NH1	C2	O2P	48.105
LYS62	NZ	G13	O6	44.366
ARG137	NH2	A4	O2P	25.317
C7	O2'	ALA112	O	24.528
ARG109	NH2	G8	N3	23.758
ARG137	NH2	U3	O1P	20.458
TYR69	OH	G8	O5'	17.708
GLY57	N	A12	O2P	16.808
ALA116	N	G8	O6	14.799
ARG137	NH1	C2	O1P	14.039
TYR132	OH	C2	O1P	13.669
LYS60	NZ	A12	O2P	13.179
ARG137	NE	A4	O1P	12.799
U1	O5'	ASP63	O	11.019
LYS60	NZ	U11	O1P	10.039

Table S7. Protein-RNA hydrogen bonds with percentage of persistence higher than 10% for run 7 of the N-NTD:dsTRS complex.

Donor		**Acceptor**		
Amino acid residue	**Atom**	**Nucleotide residue**	**Atom**	**%Persistence**
ARG137	NH2	A4	O2P	97.16
ARG67	NH2	C2	O2P	89.071
ARG67	NH1	C2	O2P	80.562
SER11	N	G8	O4'	79.992
LYS62	NZ	G13	O6	76.422
ARG52	NH2	U10	O1P	75.512
SER65	N	U1	O5'	75.422
ARG52	NH1	U9	O1P	61.304
ASN8	ND2	U9	O1P	58.334
ARG52	NE	U10	O2P	53.455
ARG137	NE	A4	O1P	49.365
ARG137	NH2	U3	O2P	49.315
LYS60	NZ	A12	O2P	44.816
G8	O2'	ASN8	OD1	42.886
ARG137	NE	A4	O2P	41.996
SER140	N	A6	O2P	39.916
SER140	OG	A6	O1P	37.576
A5	N6	GLU134	OE1	37.456
A5	N6	GLU134	OE2	35.466
ARG109	NH1	G8	N3	33.557
ARG137	NH2	U3	O1P	32.707
ARG137	NH1	U3	O1P	31.147
GLY139	N	A5	O1P	23.978
ASN113	ND2	U9	O2'	23.348
ASP58	N	U11	O1P	20.628
ARG109	NH2	G8	N3	18.708

ALA116	N	C7	N4	17.628
ARG52	NE	U10	O1P	17.258
G8	N2	ASN113	OD1	16.218
ASN113	ND2	C7	O2	15.648
LYS60	NZ	U11	O1P	15.118
ASN8	ND2	G8	O3'	11.479
LYS60	NZ	A12	O1P	10.109

Table S8. Protein-RNA hydrogen bonds with percentage of persistence higher than 10% for run 8 of the N-NTD:dsTRS complex.

Donor		**Acceptor**		
Amino acid residue	**Atom**	**Nucleotide residue**	**Atom**	**%Persistence**
ARG137	NH2	A4	O2P	82.132
G8	N2	PRO111	O	80.852
ARG137	NH1	U3	O2P	76.952
ARG52	NH2	U10	O2P	64.894
ARG52	NH1	U10	O2P	62.964
GLY57	N	A12	O2P	61.324
A14	N6	LYS62	O	56.154
GLY135	N	C2	O1P	54.405
ARG137	NH2	U3	O2P	53.525
MET3	N	U9	O2'	51.275
SER65	N	U1	O4'	50.005
GLY135	N	C2	O2P	43.826
TYR71	OH	G8	O5'	41.916
ARG52	NH1	U9	O1P	41.696
LYS62	NZ	G13	N7	38.956
LYS62	NZ	G13	O6	37.396
C7	O3'	ALA112	O	35.906
ARG109	NH2	G8	N3	35.036
SER11	N	G8	O5'	27.037
SER11	N	G8	O4'	24.868
HIS19	NE2	U1	O2'	23.508
ARG137	NH2	U3	O5'	22.778
HIS19	NE2	C2	O1P	20.788
ARG109	NH2	G8	N2	20.388
ARG52	NH2	U9	O1P	20.178
ARG109	NH1	G8	N2	16.878
U9	O2'	MET3	O	16.308
ARG52	NH2	U10	O1P	16.038
ARG67	NH1	U9	O4	15.498
C7	O2'	ALA112	O	15.158
C7	O2'	ASN114	O	15.128
ARG109	NH1	G8	N3	14.399
ASN8	ND2	G8	O2'	13.289
ASN8	ND2	G8	O3'	11.999
LYS60	NZ	G13	O2P	11.669
SER65	N	U1	O2	11.479

ARG52	NH1	U9	O2P	11.309
ARG52	NE	U9	O2P	10.269

Table S9. Protein-RNA hydrogen bonds with percentage of persistence higher than 10% for run 9 of the N-NTD:dsTRS complex.

Donor		Acceptor		
Amino acid residue	**Atom**	**Nucleotide residue**	**Atom**	**%Persistence**
G8	N2	PRO111	O	99.08
ASN8	ND2	U9	O1P	86.611
ARG109	NH1	G8	N3	85.681
SER11	N	G8	O4'	79.372
ARG67	NH2	C2	O2P	77.212
ARG52	NH2	U11	O2P	76.132
ARG52	NE	U10	O2P	71.663
C7	O2'	ALA112	O	61.164
ARG109	NH2	G8	N2	59.704
G8	O2'	ASN8	OD1	58.664
ARG137	NH1	A5	O2P	54.065
LYS62	NZ	G13	O6	48.295
ARG52	NH2	U10	O2P	45.505
ARG55	NH2	U11	O1P	42.186
ARG137	NH2	A4	O1P	42.006
ARG55	NH1	U11	O2P	35.626
ARG52	NH2	U10	O5'	35.026
ARG137	NH1	A4	O5'	33.207
A6	N6	SER136	OG	32.387
TYR132	OH	U3	O2P	31.307
ARG137	NH2	A4	O2P	28.827
ARG137	NH1	A4	O1P	25.097
ARG55	NH1	U10	O1P	24.578
ARG53	N	U9	O1P	23.738
C7	N4	GLY138	O	22.288
SER136	OG	A6	N7	22.028
ARG67	NH1	C2	O2P	20.618
ARG53	NH2	U10	O1P	19.758
LYS60	NZ	A12	O2P	18.438
ARG55	NH2	U11	O2P	17.558
ARG137	N	A5	O1P	16.428
SER136	OG	A6	O2P	16.028
LYS62	NZ	U1	O4	14.489
ARG53	NE	U10	O1P	14.299
ARG52	NH1	U10	O2P	14.199
ARG137	NH1	A4	O2P	14.149
ARG55	NH2	A12	O2P	13.959
ARG55	NH1	U11	O1P	12.549
ARG52	NH1	U11	O2P	11.389

Table S10. Protein-RNA hydrogen bonds with percentage of persistence higher than 10% for run 10 of the N-NTD:dsTRS complex.

Donor		Acceptor		
Amino acid residue	**Atom**	**Nucleotide residue**	**Atom**	**%Persistence**
ASN8	ND2	U9	O1P	95.73
SER11	N	G8	O4'	85.051
G8	O2'	ASN8	OD1	81.052
ARG52	NH1	U9	O2P	68.343
ARG52	NH1	U10	O2P	67.613
ARG52	NH2	U10	O2P	61.284
G8	N2	ALA112	O	50.995
LYS62	NZ	G13	O6	43.876
ASN113	ND2	U9	O2	39.476
GLY139	N	A4	O1P	34.637
ARG67	NH2	C2	O2P	34.177
SER65	OG	C2	O2P	33.887
SER140	N	A5	O1P	32.147
THR14	OG1	G8	O6	31.217
G8	N2	PRO111	O	28.877
SER140	OG	A5	O1P	27.357
ARG53	NE	U9	O1P	27.327
ARG53	NH2	U9	O1P	22.408
ASN113	ND2	U10	O4'	22.008
ARG52	NH1	U9	O1P	21.678
ARG137	NH2	A4	O2P	19.688
ASN114	N	G8	N2	17.608
ARG67	NH1	C2	O2P	17.388
ARG53	NH2	G8	O3'	17.348
ARG55	NH1	U11	O2P	16.328
ARG55	NH2	A12	O2P	14.249
C7	O2'	ALA112	O	13.959
ASN114	N	C7	O2	13.819
SER140	OG	A4	O3'	13.199
U1	O5'	ASP63	O	12.209
ARG137	NH1	A4	O2P	11.969
SER65	OG	U1	O5'	11.059
C7	O3'	ASN113	O	10.749
GLY139	N	A5	O1P	10.439

Table S11. Protein-RNA hydrogen bonds with percentage of persistence higher than 10% for run 11 of the N-NTD:dsTRS complex.

Donor		Acceptor		
Amino acid residue	**Atom**	**Nucleotide residue**	**Atom**	**%Persistence**
ARG137	NH1	A5	O2P	74.893
C7	O2'	ALA116	O	44.726
ARG137	NH2	A4	O2P	43.476
ARG67	NH2	C2	O2P	42.776

ARG137	NH2	A4	O1P	42.736
ARG109	NH2	G8	N3	41.366
SER65	OG	C2	O2P	38.096
A6	N6	GLU134	OE2	38.036
TYR69	OH	G8	N7	32.767
ARG137	NH1	A4	O5'	31.467
C2	N4	ASP63	O	31.467
LYS62	NZ	G13	O6	30.467
ARG137	NH1	A4	O1P	29.627
A6	N6	GLU134	OE1	28.987
ARG52	NH1	U9	O1P	28.437
ALA116	N	C7	O2	23.388
ARG137	NH1	A4	O2P	23.288
ARG52	NH2	U10	O1P	23.018
SER11	N	G8	O4'	21.028
ARG52	NH2	U10	O2P	19.338
ARG53	N	U9	O2P	17.758
ARG52	NE	U10	O2P	16.358
ARG67	NH1	C2	O2P	16.128
LYS62	NZ	G13	N7	14.779
G8	O5'	THR51	O	14.299
ASN8	ND2	U9	O1P	14.059
A5	N6	GLU134	OE2	13.409
GLY139	N	C7	O2P	12.949
LYS60	NZ	A12	O2P	12.929
A5	N6	GLU134	OE1	12.629
ARG52	NE	U9	O2P	12.349
ARG53	NH1	U9	O1P	11.029
ARG137	NH2	A5	O2P	11.019
LYS60	NZ	U11	O1P	10.119

Table S12. Protein-RNA hydrogen bonds with percentage of persistence higher than 10% for run 12 of the N-NTD:dsTRS complex.

Donor		**Acceptor**		
Amino acid residue	**Atom**	**Nucleotide residue**	**Atom**	**%Persistence**
SER11	N	G8	O4'	91.081
ALA15	N	G8	O6	88.661
ASN8	ND2	U9	O1P	64.134
ARG52	NH1	U9	O2P	62.854
ARG52	NH2	U10	O2P	58.784
SER65	OG	C2	O2P	52.505
LYS62	NZ	G13	O6	47.575
SER136	OG	C7	O2P	45.715
C7	N4	GLU134	O	43.316
ARG52	NH1	U10	O2P	42.966
C7	O2'	ALA116	O	42.726
G8	O2'	ASN8	OD1	28.927
A5	N6	GLU134	OE1	24.328

U1	O5'	ASP63	O	17.968
ARG137	NH2	A5	O2P	15.468
TYR69	OH	U9	O4	15.458
ARG52	NH2	U9	O2P	14.889
A5	N6	GLU134	OE2	13.379
A5	N6	GLU134	O	12.609
ARG137	NH1	A5	O2P	12.079
ARG109	NH2	G8	O2'	11.109
ARG137	NH2	A4	O2P	10.899
ARG137	NH2	A6	O1P	10.629
GLY1	N	U10	O1P	10.449
ARG52	NH2	U10	O5'	10.449
U1	O5'	LYS62	O	10.239

Table S13. Protein-RNA hydrogen bonds with percentage of persistence higher than 10% for run 13 of the N-NTD:dsTRS complex.

Donor		**Acceptor**		
Amino acid residue	**Atom**	**Nucleotide residue**	**Atom**	**%Persistence**
ARG52	NH2	U10	O2P	65.473
ARG52	NH1	U10	O2P	56.324
ARG48	NH2	U9	O1P	49.485
THR9	OG1	G8	N2	46.625
LYS62	NZ	U11	O4	45.025
SER65	OG	C2	O2P	42.236
ARG52	NH1	U9	O1P	41.726
LYS62	NZ	U10	O4	35.426
THR9	OG1	G8	N3	35.096
LYS60	NZ	A12	O2P	34.437
ASN110	ND2	C7	O3'	30.657
C2	N4	LYS62	O	30.057
G8	N2	ASN8	O	29.557
ARG67	NH2	C2	O2P	27.337
TYR71	OH	G8	O5'	25.507
LYS60	NZ	G13	O2P	24.828
U1	O5'	ASP63	OD1	23.708
THR9	OG1	G8	O2'	21.988
ARG137	NH2	A4	O2P	20.918
ARG52	NH2	U10	O1P	18.808
ARG67	NH2	C2	O1P	16.548
C7	O2'	ASN110	OD1	15.298
SER140	OG	A4	O2P	14.269
ARG52	NH1	U9	O2P	14.109
ARG48	NH1	U9	O1P	12.929
C7	O2'	ASN8	OD1	12.719
ARG52	NE	U10	O2P	12.429
ARG52	NH2	U9	O2P	12.109
ARG52	NE	U9	O2P	11.909
ARG137	NH2	U3	O2P	11.179

ARG137	NH1	U3	O2P	10.049

Table S14. Protein-RNA hydrogen bonds with percentage of persistence higher than 10% for run 14 of the N-NTD:dsTRS complex.

Donor		Acceptor		
Amino acid residue	**Atom**	**Nucleotide residue**	**Atom**	**%Persistence**
ASN8	ND2	U9	O1P	88.451
SER11	N	G8	O4'	79.162
ARG67	NH2	C2	O2P	77.662
G8	N2	PRO111	O	75.962
G8	O2'	ASN8	OD1	73.253
ARG137	NH2	A4	O2P	60.934
ARG52	NH1	U9	O1P	52.525
ARG52	NH2	U10	O1P	45.295
LYS60	NZ	A12	O2P	44.456
ARG52	NE	U10	O2P	43.366
ARG137	NH2	U3	O1P	33.547
ARG137	NH2	A5	O2P	33.437
LYS62	NZ	G13	O6	30.797
ARG137	NH1	U3	O1P	25.287
ARG67	NH1	C2	O2P	24.208
ARG137	NH1	A4	O1P	23.128
ARG137	NH1	A4	O2P	17.528
LYS60	NZ	U11	O1P	16.218
ARG137	NH2	A4	O1P	15.778
C7	O2'	ALA112	O	14.879
LYS62	NZ	U11	O4	14.739
LYS62	NZ	U10	O4	14.309
ARG52	NH2	U11	O2P	12.049
ARG137	NE	A5	O2P	11.019
ARG53	N	U9	O1P	10.179
ARG137	NE	A4	O1P	10.179

Table S15. Protein-RNA hydrogen bonds with percentage of persistence higher than 10% for run 15 of the N-NTD:dsTRS complex.

Donor		Acceptor		
Amino acid residue	**Atom**	**Nucleotide residue**	**Atom**	**%Persistence**
ARG52	NH2	U10	O1P	90.731
SER11	N	G8	O4'	87.771
ARG52	NE	U10	O2P	81.122
ASN8	ND2	G8	O5'	70.823
SER65	OG	C2	O2P	63.744
ARG52	NH1	U9	O1P	56.774
ASP58	N	U11	O1P	51.925
ARG137	NH2	A6	O1P	47.055

LYS62	NZ	U11	O2P	46.425
A6	N6	GLU134	OE1	46.375
ASN7	N	U9	O1P	45.345
ALA15	N	G8	O6	44.186
A6	N6	GLU134	OE2	40.856
LYS60	NZ	A12	O2P	36.106
GLY4	N	U9	O2'	35.266
ARG137	NH2	C7	O2P	31.617
A5	N6	GLU134	OE2	31.057
ARG137	NE	A6	O2P	30.077
A5	N6	GLU134	OE1	29.237
ASN8	N	U9	O1P	23.178
GLY138	N	A5	O2P	22.298
ARG137	NE	A6	O1P	21.658
GLY57	N	U10	O3'	21.088
U1	O5'	ASP63	O	17.488
GLY57	N	U10	O1P	15.608
ARG137	NH1	C7	O2P	15.258
GLY57	N	U11	O1P	15.168
GLY20	N	U3	O1P	14.579
ARG137	NH2	A6	O2P	13.939
ARG109	NH2	G8	N3	12.389
ASN8	ND2	U9	O1P	11.059
GLY138	N	A5	O1P	11.039

Table S16. Protein-RNA hydrogen bonds with percentage of persistence higher than 10% for run 16 of the N-NTD:dsTRS complex.

Donor		**Acceptor**		
Amino acid residue	**Atom**	**Nucleotide residue**	**Atom**	**%Persistence**
ARG52	NH2	U10	O1P	90.731
SER11	N	G8	O4'	87.771
ARG52	NE	U10	O2P	81.122
ASN8	ND2	G8	O5'	70.823
SER65	OG	C2	O2P	63.744
ARG52	NH1	U9	O1P	56.774
ASP58	N	U11	O1P	51.925
ARG137	NH2	A6	O1P	47.055
LYS62	NZ	U11	O2P	46.425
A6	N6	GLU134	OE1	46.375
ASN7	N	U9	O1P	45.345
ALA15	N	G8	O6	44.186
A6	N6	GLU134	OE2	40.856
LYS60	NZ	A12	O2P	36.106
GLY4	N	U9	O2'	35.266
ARG137	NH2	C7	O2P	31.617
A5	N6	GLU134	OE2	31.057
ARG137	NE	A6	O2P	30.077
A5	N6	GLU134	OE1	29.237

ASN8	N	U9	O1P	23.178
GLY138	N	A5	O2P	22.298
ARG137	NE	A6	O1P	21.658
GLY57	N	U10	O3'	21.088
U1	O5'	ASP63	O	17.488
GLY57	N	U10	O1P	15.608
ARG137	NH1	C7	O2P	15.258
GLY57	N	U11	O1P	15.168
GLY20	N	U3	O1P	14.579
ARG137	NH2	A6	O2P	13.939
ARG109	NH2	G8	N3	12.389
ASN8	ND2	U9	O1P	11.059
GLY138	N	A5	O1P	11.039

Table S17. Protein-RNA hydrogen bonds with percentage of persistence higher than 10% for run 17 of the N-NTD:dsTRS complex.

Donor		**Acceptor**		
Amino acid residue	**Atom**	**Nucleotide residue**	**Atom**	**%Persistence**
TYR69	OH	U9	O2P	85.441
ALA15	N	G8	O6	82.052
ARG52	NH1	U11	O2P	71.533
ARG137	NE	U3	O2P	67.643
ARG67	NH1	U9	O4	62.614
ARG52	NH2	U11	O2P	60.224
A6	N6	SER140	OC1	42.976
ARG52	NH1	U10	O2P	41.026
A6	N6	GLU134	OE2	36.776
A6	N6	GLU134	OE1	36.396
ARG52	NH1	U10	O1P	31.967
C7	N4	SER140	OC2	30.957
ARG137	NH1	A4	O2P	27.637
ARG55	NH1	U11	O1P	25.507
ARG137	NH2	U3	O2P	24.318
ARG55	NH2	A12	O1P	21.748
THR51	OG1	U9	O1P	20.888
C7	N4	SER140	OC1	18.278
THR51	N	U9	O2P	17.678
A6	N6	SER140	OC2	17.328
ARG52	NH2	U10	O1P	16.808
ARG55	NH1	A12	O2P	16.218
ARG55	NH2	A12	O2P	15.908
LYS60	NZ	G13	N7	13.709
SER11	N	G8	O4'	12.919
MET61	N	G13	O2P	12.719
ARG55	NH2	U11	O1P	12.459
ARG52	NE	U10	O2P	12.159
TYR71	OH	G8	O5'	11.879
LYS60	NZ	G13	O2P	11.549

LYS60	NZ	G13	O6	10.849
ARG109	NH1	C7	O2	10.399

Table S18. Protein-RNA hydrogen bonds with percentage of persistence higher than 10% for run 18 of the N-NTD:dsTRS complex.

Donor		Acceptor		
Amino acid residue	**Atom**	**Nucleotide residue**	**Atom**	**%Persistence**
SER65	OG	C2	O2P	92.471
SER65	OG	U1	O5'	86.661
GLY20	N	C2	O1P	78.272
LYS62	NZ	G13	O6	72.413
A6	N6	GLU134	OE1	67.753
SER11	N	G8	O4'	61.564
ARG67	NH2	U10	O4	55.734
ARG52	NH2	U11	O2P	50.715
A5	N6	GLU134	OE2	45.525
ARG52	NH2	U10	O2P	44.046
ARG52	NE	U10	O2P	41.696
ASN8	ND2	U9	O1P	41.566
ARG67	NH1	U9	O4	35.296
SER136	OG	C7	O2P	33.277
ARG137	NE	A6	O1P	32.447
ARG137	N	A6	O2P	30.087
SER11	N	G8	O5'	29.657
TYR69	OH	U9	O2P	28.207
ARG67	NH1	U10	O4	25.857
C7	N4	GLY135	O	24.758
TYR71	OH	G8	O5'	22.798
ARG52	NH2	U9	O1P	21.968
C7	N4	GLU134	OE1	21.908
ARG137	NH2	A6	O1P	21.708
TYR132	OH	A5	O2P	20.948
ARG137	NH2	A5	O1P	20.238
ARG137	NE	A6	O2P	19.918
LYS21	NZ	U1	O5'	19.888
HIS19	NE2	U3	O1P	19.878
HIS19	NE2	U3	O2P	17.838
ARG137	NH2	A6	O2P	17.218
ARG52	NH1	U10	O2P	15.668
ARG137	NH2	A5	O2P	15.108
ARG52	NH2	U10	O1P	14.939
C7	O2'	SER140	OC1	14.319
ARG55	NH1	U11	O1P	13.819
A6	N6	GLU134	OE2	13.519
ARG52	NH1	U9	O2P	13.379
ARG52	NH2	U10	O5'	13.139
LYS62	NZ	G13	N7	12.699
ARG52	NH1	U9	O1P	11.539

ARG55	NH2	A12	O1P	11.409
ARG55	NH2	U11	O1P	11.279
C7	O3'	SER140	OC1	10.769
GLY20	N	C2	O2P	10.349
ARG55	NE	A12	O1P	10.059

Table S19. Protein-RNA hydrogen bonds with percentage of persistence higher than 10% for run 19 of the N-NTD:dsTRS complex.

Donor		**Acceptor**		
Amino acid residue	**Atom**	**Nucleotide residue**	**Atom**	**%Persistence**
TYR69	OH	U9	O2P	59.374
ARG137	NH2	A6	O2P	56.354
TYR71	OH	G8	O5'	56.334
SER11	N	G8	O4'	53.535
A6	N6	GLU134	OE1	43.586
LYS62	NZ	G13	O6	43.226
ARG137	NE	A6	O2P	42.416
ARG52	NH2	U11	O2P	41.616
SER11	N	G8	O5'	40.796
ARG52	NH2	U10	O1P	40.716
ARG52	NE	U10	O2P	40.426
HIS19	NE2	U3	O1P	36.456
A5	N6	GLU134	OE2	36.376
HIS19	NE2	U3	O2P	29.877
GLY20	N	C2	O1P	27.647
TYR132	OH	U3	O2P	27.377
GLY20	N	C2	O2P	26.717
A5	N6	GLU134	OE1	25.167
ARG53	NE	U9	O1P	25.097
ARG67	NH1	U10	O4	24.988
ARG67	NH2	U10	O4	24.598
ARG52	NH1	U11	O2P	23.338
ARG53	NH2	G8	O3'	22.058
LYS62	NZ	G13	N7	16.408
A6	N6	GLU134	OE2	15.398
ARG137	NH1	A5	O2P	15.048
LYS60	NZ	A12	O2P	14.909
TYR132	OH	C2	O2P	14.329
SER65	OG	C2	O2P	13.099
LYS60	NZ	A12	O1P	12.779
ARG137	NH2	A4	O2P	12.659
ARG52	NE	U10	O1P	11.229
SER65	OG	U1	O5'	11.089
ARG52	NH1	U10	O1P	11.069
LYS60	NZ	G13	O2P	10.569

Table S20. Protein-RNA hydrogen bonds with percentage of persistence higher than 10% for run 20 of the N-NTD:dsTRS complex.

Donor		Acceptor		
Amino acid residue	**Atom**	**Nucleotide residue**	**Atom**	**%Persistence**
G8	N2	PRO111	O	98.31
ARG137	NH1	A4	O2P	94.911
SER11	N	G8	O4'	84.882
ARG137	NH2	U3	O1P	78.582
ARG55	NH1	U11	O2P	66.813
ARG55	NH2	U10	O1P	65.853
ARG53	NH1	U10	O2P	60.174
C7	O2'	ALA112	O	54.205
ARG109	NH1	G8	N3	53.995
ARG109	NH2	G8	N2	53.295
ARG137	NH1	U3	O1P	52.145
ARG55	NH1	U10	O1P	50.505
ARG137	NH1	U3	O5'	49.945
ARG53	NH1	U9	O1P	39.996
ARG55	NH1	U10	O5'	37.486
ARG53	NH2	U9	O1P	33.637
GLY4	N	U9	O2'	31.537
ARG52	NH1	C2	O2P	31.067
LYS60	NZ	G13	N7	30.737
LYS60	NZ	A12	N7	27.197
SER65	N	U1	O5'	24.268
GLY4	N	U9	O3'	23.618
ARG67	NH2	C2	O1P	23.098
ARG53	NH1	U9	O2P	20.328
ARG55	NH2	U11	O2P	15.928
ARG52	NH2	C2	O2P	15.418
SER65	N	C2	O2P	15.338
ARG109	NH2	G8	N3	15.168
ARG53	NH1	U9	O5'	14.229
ARG55	NH1	U10	O2P	12.899
ARG137	NH1	U3	O2P	11.879
GLY1	N	U10	O2'	10.909
ARG55	NH2	U10	O2P	10.119
C7	O3'	ASN113	O	10.009

Table S21. Protein-RNA hydrogen bonds with percentage of persistence higher than 10% for run 21 of the N-NTD:dsTRS complex.

Donor		Acceptor		
Amino acid residue	**Atom**	**Nucleotide residue**	**Atom**	**%Persistence**
ARG52	NH1	U10	O2P	49.675

GLY138	N	C2	O1P	41.006
TYR69	OH	U9	O2P	38.796
ASN8	ND2	U9	O1P	36.816
ARG52	NH2	U10	O2P	34.217
ARG52	NH2	U9	O1P	33.167
G8	O2'	ASN8	OD1	32.797
ARG137	NH1	C2	O1P	31.787
ARG55	NH1	U11	O2P	31.477
GLY57	N	G13	O2P	30.967
THR51	OG1	U9	O1P	29.627
SER11	N	G8	O5'	27.787
U1	O5'	GLU134	OE1	26.817
TYR132	OH	C2	O1P	26.797
ARG137	NH2	U3	O2P	26.057
G8	N2	ASN7	OD1	25.907
THR51	N	U9	O1P	21.248
ARG52	NH1	U10	O1P	19.548
G8	N2	MET3	O	17.318
U1	O2'	SER136	O	17.008
ARG55	NH2	A12	O2P	16.418
ARG137	NH2	C2	O1P	15.888
ASP58	N	A12	O1P	15.038
LYS62	NZ	U1	O4	14.049
LEU5	N	C7	O2	13.909
TYR132	OH	C2	O2P	13.239
TYR71	OH	G8	O5'	12.999
G8	O2'	ASN7	O	12.699
ARG52	NH1	U9	O1P	12.669
LYS62	NZ	G13	O6	11.849
ARG137	NH2	U3	O1P	10.969
U1	O5'	SER65	O	10.599
ARG137	NH1	U3	O1P	10.179

Table S22. Protein-RNA hydrogen bonds with percentage of persistence higher than 10% for run 22 of the N-NTD:dsTRS complex.

Donor		**Acceptor**		
Amino acid residue	**Atom**	**Nucleotide residue**	**Atom**	**%Persistence**
LYS62	NZ	G13	O6	50.245
C7	O2'	ALA116	O	47.445
SER65	OG	C2	O2P	44.936
SER11	N	G8	O4'	42.196
ALA116	N	C7	O2	40.356
ARG52	NH1	U9	O1P	40.036
G8	N2	PRO111	O	32.907
ASN8	ND2	U9	O1P	32.897
ARG67	NH2	C2	O1P	31.247
LYS60	NZ	U10	O2P	30.787
ARG137	NH2	A4	O2P	28.767

G8	O2'	ASN8	OD1	26.877
G8	N2	ASN114	O	25.787
G8	N2	ASN114	OD1	25.467
ARG67	NH2	C2	O2P	23.338
ARG137	NE	A4	O2P	22.998
ARG52	NH2	U9	O1P	20.988
ARG52	NH1	U9	O2P	19.938
ASN114	ND2	G8	O2'	18.718
C7	O2'	ALA112	O	18.438
ASN114	N	U9	O2'	17.608
ARG137	NH2	U3	O2P	17.498
ARG52	NH2	U10	O1P	17.478
LYS60	NZ	U11	O2P	15.528
LYS60	NZ	U10	O1P	15.468
ALA116	N	G8	N2	14.709
ASN114	ND2	G8	N3	14.419
ARG52	NE	U10	O2P	14.129
U1	O5'	ASP63	O	14.029
TYR69	OH	G8	N7	13.439
G8	O2'	PRO111	O	12.699
ARG137	NH1	A5	O2P	12.589
SER65	N	C2	O2P	12.099
ARG137	NH2	A4	O1P	11.649
ARG52	NH1	U10	O2P	10.929
ARG52	NH2	U10	O2P	10.619
LYS60	NZ	U9	O1P	10.159

Table S23. Protein-RNA hydrogen bonds with percentage of persistence higher than 10% for run 23 of the N-NTD:dsTRS complex.

Donor		**Acceptor**		
Amino acid residue	**Atom**	**Nucleotide residue**	**Atom**	**%Persistence**
SER11	N	G8	O4'	54.355
LYS62	NZ	G13	O6	48.635
ASN114	ND2	C7	O2P	33.217
ARG52	NH2	C2	O2P	31.087
ARG137	NH1	U3	O1P	29.857
C7	O2'	PRO111	O	28.787
SER65	N	U1	O5'	23.648
ARG137	NH2	U3	O2P	21.728
SER11	N	G8	O2'	21.238
ARG137	NH2	U3	O1P	20.988
ASN8	ND2	U9	O1P	18.028
G8	O2'	ASN8	OD1	17.018
LYS60	NZ	G13	O2P	16.008
C7	O3'	ALA112	O	14.299
GLY57	N	A12	O2P	13.759
C7	O3'	PRO111	O	12.569
TYR71	OH	G8	O5'	12.389

GLY57	N	U11	O1P	11.369
GLY57	N	U11	O2P	10.819

Table S24. Protein-RNA hydrogen bonds with percentage of persistence higher than 10% for run 24 of the N-NTD:dsTRS complex.

Donor		Acceptor		
Amino acid residue	**Atom**	**Nucleotide residue**	**Atom**	**%Persistence**
ARG52	NH2	U10	O1P	91.581
SER11	N	G8	O4'	90.611
ARG52	NE	U10	O2P	82.912
ARG55	NH1	U11	O2P	69.443
ARG137	NH1	A5	O2P	69.293
ARG137	NH2	A4	O1P	63.614
SER65	OG	C2	O2P	57.664
A6	N6	GLU134	OE1	54.195
LYS62	NZ	G13	O6	44.756
LYS60	NZ	A12	O2P	42.686
ARG55	NH2	U11	O2P	39.826
ASN8	ND2	U9	O2P	39.646
LYS60	NZ	U11	O1P	39.366
ARG137	NH1	A4	O5'	38.486
A6	N6	GLU134	OE2	38.146
ARG137	NH1	A4	O1P	36.986
ARG55	NH2	U11	O1P	27.577
ARG67	NH2	U9	O4	25.517
ARG52	NH1	U9	O1P	25.327
ARG137	NH2	A5	O2P	22.408
ASN8	ND2	U9	O1P	21.488
C2	N4	LYS62	O	20.548
LYS62	NZ	G13	N7	18.388
ARG55	NH1	U10	O1P	18.348
ARG137	NH2	A4	O2P	16.678
U1	O5'	ASP63	O	16.028
A14	N6	MET61	O	15.338
ARG137	NE	A5	O2P	14.089
SER65	N	C2	O2P	13.929
GLY139	N	A6	O1P	13.419
ARG109	NH2	G8	N3	12.049
C2	N4	ASP63	O	12.019
ARG52	NE	U10	O1P	11.889
LYS62	NZ	A12	N7	11.069
ARG67	NH2	C2	O2P	10.939
ARG137	NH1	A4	O2P	10.769
TYR132	OH	U3	O2P	10.509

Table S25. Protein-RNA hydrogen bonds with percentage of persistence higher than 10% for run 25 of the N-NTD:dsTRS complex.

Donor		Acceptor		
Amino acid residue	**Atom**	**Nucleotide residue**	**Atom**	**%Persistence**
TYR132	OH	A4	O2P	67.043
SER11	N	G8	O4'	41.796
A5	N6	GLU134	OE1	39.956
ARG67	NH1	U10	O4	32.547
TYR69	OH	U9	O2P	31.887
A5	N6	GLU134	OE2	30.637
A4	N6	GLU134	OE1	30.497
ARG67	NH2	U11	O4	29.777
ARG137	NH2	A5	O2P	29.407
ARG67	NH2	U10	O4	27.757
G8	N2	MET3	O	26.987
ARG52	NH2	U10	O1P	26.267
ARG55	NH2	U10	O1P	25.857
ARG52	NH1	U10	O2P	23.388
LYS60	NZ	A14	O2P	23.098
A4	N6	GLU134	OE2	23.058
ARG55	NH1	U10	O1P	22.818
TYR71	OH	G8	O5'	22.448
ARG52	NH2	U9	O1P	22.358
ARG52	NE	U9	O1P	21.988
ARG52	NH1	U9	O1P	21.898
ARG137	NH1	A5	O2P	21.748
ARG137	NH2	A5	O1P	21.608
LYS60	NZ	G13	O2P	21.158
ARG55	NH2	U11	O2P	20.478
ARG55	NH1	U11	O2P	20.018
G8	N2	ALA2	O	17.898
ARG137	NH1	A4	O1P	17.678
ARG52	NH1	U10	O1P	17.248
SER11	N	G8	N7	17.088
A6	N6	GLU134	OE2	16.428
ARG55	NH2	U11	O1P	15.848
LYS62	NZ	G13	O6	15.848
ARG55	NE	U11	O1P	15.178
LYS60	NZ	G13	O1P	14.659
ARG55	NH1	U10	O2P	14.359
THR51	N	U9	O1P	14.309
THR51	OG1	U9	O1P	13.749
ARG137	NH2	A4	O2P	13.599
ARG55	NE	U11	O2P	13.359
ARG52	NE	U10	O2P	13.199
ARG67	NH1	U9	O4	13.139
GLY20	N	U1	O4	12.489
LYS60	NZ	A12	O1P	12.019
LYS62	NZ	A14	N7	11.619

ARG137	NH1	U3	O1P	11.459
ARG55	NH2	U10	O2P	11.429
ARG137	NE	A5	O1P	11.269
ASN8	ND2	G8	N3	10.629
ARG55	NH1	U10	O5'	10.579
TYR132	OH	C2	O2P	10.129
ARG52	NH2	U10	O2P	10.019

Table S26. Protein-RNA hydrogen bonds with percentage of persistence higher than 10% for run 1 of the N-NTD:dsNS complex.

Donor		**Acceptor**		
Amino acid residue	**Atom**	**Nucleotide residue**	**Atom**	**%Persistence**
SER11	N	G8	O4'	80.052
ARG52	NH1	C10	O2P	66.783
ALA15	N	G8	O6	65.313
C7	N4	GLU134	O	63.594
ARG52	NH1	U9	O2P	58.534
ARG52	NH2	C10	O2P	53.675
LYS62	NZ	G12	O6	44.126
C7	O2'	ALA116	O	39.106
GLY57	N	G12	O2P	35.286
ARG137	NH2	A6	O1P	29.577
ARG52	NH2	C10	O1P	29.367
ASN8	ND2	U9	O1P	28.597
ARG137	NE	A6	O1P	27.877
LYS62	NZ	G12	N7	26.697
C1	N4	ASP63	O	24.568
ARG137	N	A6	O2P	24.008
G8	O2'	ASN8	OD1	22.768
C1	N4	LYS62	O	22.198
GLY138	N	G5	O2P	20.618
HIS19	NE2	C3	O2P	20.468
ARG52	NE	C10	O2P	20.368
GLY138	N	G5	O1P	20.228
ARG137	NH2	G5	O1P	20.098
A2	N6	ASP63	O	19.428
SER65	OG	A2	O2P	17.948
GLY1	N	C10	O1P	15.998
ARG67	NH2	A2	O2P	14.829
ARG137	NH1	A6	O2P	13.939
ARG137	NH2	A6	O2P	13.249
HIS19	NE2	A2	O1P	11.719

Table S27. Protein-RNA hydrogen bonds with percentage of persistence higher than 10% for run 2 of the N-NTD:dsNS complex.

Donor		Acceptor		
Amino acid residue	**Atom**	**Nucleotide residue**	**Atom**	**%Persistence**
ARG52	NH2	C10	O1P	97.35
SER65	OG	A2	O2P	92.141
ARG52	NE	C10	O2P	90.011
THR17	OG1	A2	O1P	75.832
ARG67	NE	A2	O2P	65.743
C1	N4	ASP63	O	57.924
ARG67	NH2	A2	O1P	57.474
GLY57	N	A11	O1P	53.715
ARG67	NH2	C3	O2P	44.626
ARG137	NH1	U4	O2P	42.476
LYS62	NZ	A11	O2P	40.876
G8	N2	ASN8	OD1	34.557
LYS62	NZ	G12	O2P	33.557
ARG137	NH2	C3	O2P	30.877
ARG67	NH2	A2	O5'	28.617
GLY4	N	U9	O2'	27.887
ARG137	NH2	U4	O2P	26.877
LYS60	NZ	U13	O2P	20.118
ARG67	NE	A2	O1P	19.818
ARG137	NH1	G5	O2P	18.848
ARG137	NH1	C3	O5'	17.648
GLN18	N	A2	O1P	16.838
LYS62	NZ	G12	O6	15.048
ARG52	NE	C10	O1P	14.859
LYS62	NZ	G12	N7	14.419
C7	O3'	GLY139	O	13.549
C10	O2'	GLY1	O	10.639
LYS60	NZ	G12	O1P	10.189

Table S28. Protein-RNA hydrogen bonds with percentage of persistence higher than 10% for run 3 of the N-NTD:dsNS complex.

Donor		Acceptor		
Amino acid residue	**Atom**	**Nucleotide residue**	**Atom**	**%Persistence**
C1	N4	LYS62	O	75.152
C7	O2'	ASN8	OD1	52.695
ALA112	N	C7	O2'	50.375
LYS60	NZ	U13	O2P	48.035
LYS62	NZ	G12	O6	44.036
LYS62	NZ	G12	N7	42.216
ARG48	NH1	G8	O5'	41.666
G8	N2	ASN8	O	37.676
ARG52	NH2	C10	O2P	35.856

ASN8	ND2	C7	O3'	32.877
ARG55	NH2	C10	O1P	32.407
ARG52	NH2	C10	O1P	31.027
SER140	OG	U4	O1P	29.037
ARG67	NH2	A2	O2P	28.627
LYS60	N	G12	O2P	27.587
ARG67	NH1	A2	O2P	26.297
GLY59	N	A11	O1P	25.217
SER140	N	U4	O1P	24.618
ARG52	NH1	U9	O1P	23.948
LYS60	NZ	G12	O1P	23.848
GLY139	N	C3	O1P	23.708
ARG52	NH1	C10	O2P	20.408
HIS19	NE2	A2	O1P	20.158
ARG48	NH1	U9	O1P	18.688
ARG55	NH1	C10	O1P	17.008
THR51	OG1	U9	O1P	15.308
ARG52	NH2	U9	O1P	15.248
ARG67	NH2	A2	O1P	14.889
TYR132	OH	A2	O2P	13.599
ASN8	ND2	C7	O2'	13.289
TYR132	OH	A2	O1P	12.439
ALA2	N	C7	O1P	12.159
ARG52	NE	C10	O2P	11.749
SER65	OG	A2	O2P	11.579
GLY59	N	A11	O2P	10.569
SER65	OG	C1	O5'	10.529
GLY139	N	C3	O2P	10.169

Table S29. Protein-RNA hydrogen bonds with percentage of persistence higher than 10% for run 4 of the N-NTD:dsNS complex.

Donor		**Acceptor**		
Amino acid residue	**Atom**	**Nucleotide residue**	**Atom**	**%Persistence**
SER65	OG	A2	O2P	87.161
ARG52	NH2	C10	O1P	85.651
SER11	N	G8	O4'	85.191
C1	N4	LYS62	O	84.532
ARG52	NE	C10	O2P	77.712
SER65	OG	C1	O5'	64.964
ARG137	NE	G5	O2P	61.854
ASN8	N	U9	O1P	61.204
ARG137	NH2	G5	O2P	55.274
GLY59	N	A11	O1P	46.975
LYS60	N	G12	O2P	43.696
LYS62	NZ	G12	O6	39.706
G8	O2'	ASN8	O	36.476
ARG52	NH1	U9	O1P	34.137
ASN8	ND2	G8	O5'	32.617

SER140	OG	G5	O1P	32.057
SER140	N	G5	O1P	30.537
ARG137	NH1	U4	O2P	26.187
LYS62	NZ	G12	N7	25.167
G8	N2	PRO111	O	23.588
ASN8	ND2	U9	O2P	21.268
ARG109	NH2	G8	N3	19.318
GLY139	N	U4	O1P	17.508
TYR132	OH	C3	O2P	13.129
C7	O2'	ALA112	O	12.299
LYS60	NZ	U13	O2P	12.229
LYS62	NZ	A11	N7	12.219
GLY138	N	U4	O1P	10.289

Table S30. Protein-RNA hydrogen bonds with percentage of persistence higher than 10% for run 5 of the N-NTD:dsNS complex.

Donor		**Acceptor**		
Amino acid residue	**Atom**	**Nucleotide residue**	**Atom**	**%Persistence**
SER65	OG	A2	O2P	90.501
SER11	N	G8	O4'	85.341
ARG52	NH1	C10	O2P	83.422
ARG52	NH2	C10	O2P	80.322
GLY20	N	A2	O1P	76.402
C1	N4	ASP63	O	71.983
ARG52	NH1	U9	O2P	55.694
SER65	OG	C1	O5'	49.405
ARG137	NH2	A6	O1P	42.396
A6	N6	GLU134	OE1	37.476
ARG137	NH2	C7	O2P	36.096
A6	N6	GLU134	OE2	35.756
ARG137	NE	A6	O2P	35.056
ASN7	ND2	U9	O1P	25.607
GLY138	N	G5	O2P	22.628
ALA116	N	G8	N2	19.938
ARG137	NH2	A6	O2P	17.718
ARG137	NE	A6	O1P	17.378
ASN7	ND2	G8	O3'	16.648
ARG52	NH2	C10	O5'	16.338
ARG53	NH2	U9	O1P	16.178
G8	N2	ASN114	O	15.098
ARG137	NH2	A6	O5'	14.009
LYS62	NZ	G14	N7	13.939
C7	O2'	ALA116	O	12.509
ALA2	N	C10	O1P	12.079
G8	O2'	PRO111	O	11.719
ALA116	N	C7	O2	11.639
GLY1	N	A11	O2P	11.489
ASN7	N	U9	O1P	11.129

GLY1	N	A11	O1P	11.049
G8	O5'	SER11	OG	11.039
C1	N4	LYS62	O	11.009
ARG137	NH1	G5	O1P	10.269

Table S31. Protein-RNA hydrogen bonds with percentage of persistence higher than 10% for run 6 of the N-NTD:dsNS complex.

Donor		Acceptor		
Amino acid residue	**Atom**	**Nucleotide residue**	**Atom**	**%Persistence**
C1	N4	LYS62	O	81.532
ASN8	ND2	G8	N3	77.432
GLY4	N	C7	O2'	74.993
ARG67	NH1	A2	O2P	69.213
ARG67	NH2	A2	O2P	53.765
ARG52	NH1	C10	O2P	50.635
ARG52	NH2	C10	O2P	46.675
GLY57	N	G12	O2P	37.316
ARG67	NH2	A2	O1P	37.126
ARG137	NH2	U4	O2P	33.547
LYS62	NZ	G12	O6	27.497
ARG52	NH2	C10	O1P	23.258
ARG137	NH1	U4	O2P	22.898
ARG52	NE	U9	O2P	20.518
LYS62	NZ	G12	N7	18.668
ARG52	NE	C10	O2P	17.618
ARG137	NH1	C3	O2P	16.658
ARG52	NH2	A11	O2P	15.928
ARG52	NH1	A11	O2P	15.648
ARG52	NH2	U9	O2P	14.789
GLY1	N	C10	O2'	12.559
GLY57	N	A11	O1P	12.439
ARG137	NH1	C3	O1P	11.769
ALA2	N	U9	O2'	11.669
TYR132	OH	C3	O1P	11.439
HIS19	NE2	A2	O1P	10.949
THR17	OG1	A2	O1P	10.909
ARG137	NH2	C3	O1P	10.169
ARG55	NH2	A11	O1P	10.059

Table S32. Protein-RNA hydrogen bonds with percentage of persistence higher than 10% for run 7 of the N-NTD:dsNS complex.

Donor		Acceptor		
Amino acid residue	**Atom**	**Nucleotide residue**	**Atom**	**%Persistence**
SER11	N	G8	O4'	94.851
SER65	OG	A2	O2P	89.031

ALA15	N	G8	O6	85.081
C1	N4	ASP63	O	65.333
ARG52	NE	C10	O2P	58.954
ARG52	NH2	C10	O2P	55.604
SER136	OG	A6	O1P	54.115
ARG52	NH2	A11	O2P	42.076
GLY57	N	A11	O1P	38.496
GLY20	N	A2	O2P	36.296
A6	N6	GLU134	OE2	33.337
LYS21	N	A2	O1P	32.847
SER136	N	C7	O2P	31.717
A6	N6	GLU134	OE1	26.887
SER65	OG	C1	O5'	26.517
HIS19	NE2	C3	O1P	26.407
LYS60	NZ	U13	O2P	23.858
C1	N4	LYS62	O	22.278
C7	O2'	ALA116	O	22.188
LYS60	NZ	G12	O1P	21.778
LYS62	NZ	G12	N7	18.798
LYS21	NZ	A2	O1P	18.258
ARG137	N	A6	O1P	15.528
TYR69	OH	U9	O4	15.248
ASN8	ND2	U9	O1P	15.058
LYS62	NZ	G14	N7	15.018
ARG67	NH1	A2	O2P	13.569
HIS19	NE2	C3	O2P	13.299
LYS62	NZ	G12	O6	12.959
ARG109	NH2	G8	O2'	12.859
GLY20	N	A2	O1P	12.519
ARG137	NH2	G5	O2P	11.169
LYS62	NZ	G12	O2P	11.059
ARG137	NH2	U4	O2P	10.319
TYR132	OH	C3	O2P	10.009

Table S33. Protein-RNA hydrogen bonds with percentage of persistence higher than 10% for run 8 of the N-NTD:dsNS complex.

Donor		**Acceptor**		
Amino acid residue	**Atom**	**Nucleotide residue**	**Atom**	**%Persistence**
C1	N4	LYS62	O	94.421
ARG67	NH2	A2	O2P	84.162
ARG52	NH2	C10	O2P	64.974
LYS62	NZ	G12	O6	49.995
ARG52	NH1	U9	O2P	47.625
ARG52	NH2	U9	O2P	39.396
LYS62	NZ	G12	N7	39.256
LYS60	NZ	U13	O2P	35.936
ARG137	NH2	G5	O6	32.387
GLY138	N	C3	O1P	32.077

TYR132	OH	A2	O1P	30.667
GLY57	N	A11	O1P	29.957
ARG137	NE	U4	O2P	29.657
ARG52	NE	C10	O2P	28.397
ARG52	NH2	U9	O5'	28.317
ARG137	NH1	G5	N7	28.047
LYS60	NZ	G12	O1P	25.647
TYR71	OH	G8	O5'	23.838
ASN8	ND2	C7	O2'	23.358
ARG137	NH1	C3	O2P	22.248
SER65	OG	C1	O5'	21.838
ARG137	NH2	U4	O2P	21.828
ARG137	NH2	G5	O2P	20.568
ARG137	NH2	A2	O1P	19.948
G8	N2	ASN7	O	18.928
LYS60	NZ	G12	O2P	18.888
ARG137	NH1	A2	O5'	16.138
ARG52	NH2	U9	O1P	15.088
LYS62	NZ	U13	O4	14.099
ARG52	NH2	C10	O1P	13.889
ARG137	NH2	U4	O5'	11.729

Table S34. Protein-RNA hydrogen bonds with percentage of persistence higher than 10% for run 9 of the N-NTD:dsNS complex.

Donor		**Acceptor**		
Amino acid residue	**Atom**	**Nucleotide residue**	**Atom**	**%Persistence**
C1	N4	LYS62	O	77.592
G8	N2	ASN8	O	67.913
TYR132	OH	A2	O1P	65.993
GLY57	N	G12	O2P	53.935
ARG52	NH2	C10	O2P	53.765
LYS62	NZ	G12	O6	49.075
ARG52	NH1	U9	O1P	43.576
ARG52	NH2	U9	O5'	40.466
SER65	N	C1	O5'	38.166
ARG67	NH2	A2	O2P	37.606
G8	O2'	ASN8	OD1	32.927
SER65	OG	A2	O2P	32.407
ARG67	NH1	A2	O2P	31.167
LYS62	NZ	G12	N7	30.567
ARG48	NH2	U9	O1P	30.207
ARG137	NH2	C3	O1P	28.887
ARG52	NE	C10	O1P	24.328
LYS60	NZ	U13	O2P	22.848
ARG137	NH1	C3	O1P	22.838
ARG52	NH2	C10	O1P	20.548
THR51	N	U9	O2P	19.478
SER65	OG	C1	O5'	16.548

ARG137	NH2	C3	O2P	15.628
ARG137	NH2	A2	O1P	12.159
ARG52	NH2	U9	O1P	11.999
ARG52	N	U9	O1P	11.639
ARG137	NH1	A2	O1P	11.369
ARG137	NH1	C3	O2P	11.009
LYS60	NZ	G12	O1P	10.539

Table S35. Protein-RNA hydrogen bonds with percentage of persistence higher than 10% for run 10 of the N-NTD:dsNS complex.

Donor		**Acceptor**		
Amino acid residue	**Atom**	**Nucleotide residue**	**Atom**	**%Persistence**
ARG52	NE	C10	O2P	59.434
C1	N4	LYS62	O	51.655
ARG52	NH2	A11	O2P	51.415
LYS62	NZ	G12	O6	44.436
ARG137	NH2	A6	O2P	40.586
ARG137	NH1	G5	O2P	34.097
ARG67	NH2	A2	O2P	32.607
ARG137	NE	A6	O2P	32.007
ALA15	N	G8	O6	30.957
LYS62	NZ	G12	N7	30.847
ARG52	NH2	C10	O1P	30.037
C7	N4	GLU134	O	29.597
TYR69	OH	U9	O2P	28.787
TYR71	OH	G8	O5'	28.197
SER11	N	G8	O4'	27.007
ARG52	NH2	C10	O2P	25.327
LYS60	NZ	G12	O2P	24.708
C1	N4	MET61	O	23.698
ARG67	NH1	A2	O2P	22.938
C7	O2'	PRO111	O	21.648
SER11	N	G8	O5'	21.168
GLY57	N	A11	O1P	20.968
SER11	N	G8	O2'	20.908
TYR69	OH	U9	O4	18.098
ARG137	NH2	G5	O2P	17.918
C7	O3'	ALA112	O	17.388
SER65	OG	A2	O2P	17.278
ARG137	NE	G5	O2P	17.138
LYS62	NZ	U13	O4	14.229
HIS19	NE2	U4	O2P	13.739
A2	N6	LYS62	O	13.639
ASP58	N	A11	O1P	13.509
ARG109	NH1	G8	N2	12.599
ARG52	NH1	A11	O2P	11.409
C1	O5'	ASP63	OD2	10.829
ARG109	NH2	G8	N3	10.779

Table S36. Protein-RNA hydrogen bonds with percentage of persistence higher than 10% for run 11 of the N-NTD:dsNS complex.

Donor		Acceptor		
Amino acid residue	**Atom**	**Nucleotide residue**	**Atom**	**%Persistence**
SER11	N	G8	O4'	84.352
ARG137	NH1	G5	O2P	59.954
GLY57	N	G12	O2P	57.064
ARG137	NH1	U4	O2P	55.964
SER65	OG	A2	O2P	55.254
ARG52	NH1	C10	O2P	53.945
C1	N4	LYS62	O	51.805
ARG52	NH2	C10	O2P	47.335
ARG52	NH1	U9	O1P	47.105
LYS62	NZ	G12	O6	45.005
A6	N6	GLU134	OE2	44.966
ARG137	NH2	U4	O2P	41.006
ARG67	NH2	U9	O4	37.746
C1	N4	ASP63	O	37.196
GLY20	N	A2	O1P	33.237
ARG52	NH2	C10	O1P	30.407
SER65	OG	C1	O5'	25.917
ARG137	NH1	U4	O5'	24.278
LYS62	NZ	G12	N7	23.878
ARG137	NH2	C3	O1P	22.468
LYS60	NZ	U13	O2P	19.898
A6	N6	GLU134	OE1	19.738
ARG137	NH1	C3	O1P	19.578
ARG52	NE	U9	O1P	18.948
ARG137	NH1	C3	O5'	18.388
HIS19	NE2	A2	O1P	17.738
ARG137	NH2	U4	O1P	17.058
ARG52	NH2	U9	O1P	15.328
LYS60	NZ	G12	O1P	15.128
C7	O3'	ASN114	OD1	11.779
ARG52	NH1	U9	O2P	11.379
SER11	OG	G8	O5'	11.029
ARG137	NH2	C3	O2P	10.489
SER65	N	C1	O5'	10.339

Table S37. Protein-RNA hydrogen bonds with percentage of persistence higher than 10% for run 12 of the N-NTD:dsNS complex.

Donor		Acceptor		
Amino acid residue	**Atom**	**Nucleotide residue**	**Atom**	**%Persistence**
SER11	N	G8	O4'	90.121

SER65	OG	A2	O2P	86.841
ARG67	NE	A2	O2P	72.663
C1	N4	ASP63	O	69.323
ARG67	NH2	C3	O2P	65.713
ARG67	NH2	A2	O5'	62.534
GLY138	N	G5	O2P	60.444
ARG137	NH2	C7	O2P	60.184
ARG137	NH1	A6	O2P	59.494
ARG137	NH1	C7	O2P	53.185
THR17	OG1	A2	O1P	50.225
GLN18	N	A2	O1P	44.686
ARG52	NH2	U9	O1P	43.566
LYS60	NZ	G12	O2P	36.716
LYS60	NZ	A11	O1P	35.616
ARG52	NH2	C10	O2P	33.627
LYS62	NZ	G12	O6	33.317
LYS62	NZ	G12	N7	32.647
GLY57	N	A11	O1P	28.327
ARG52	NH1	U9	O1P	27.307
ARG67	NH2	A2	O2P	25.587
ARG52	NH2	C10	O1P	23.158
C1	N4	LYS62	O	20.938
ARG52	NE	U9	O1P	20.088
ARG52	NH1	C10	O2P	18.368
GLY139	N	G5	O1P	16.468
ALA116	N	G8	N2	15.638
ARG52	NH1	C10	O1P	15.428
GLY139	N	U4	O1P	13.639
SER65	OG	C1	O5'	13.279
ARG52	NE	C10	O2P	12.309
LYS60	NZ	U13	O2P	11.779
ARG52	NE	U9	O2P	10.259
ARG137	NH2	A6	O2P	10.029

Table S38. Protein-RNA hydrogen bonds with percentage of persistence higher than 10% for run 13 of the N-NTD:dsNS complex.

Donor		**Acceptor**		
Amino acid residue	**Atom**	**Nucleotide residue**	**Atom**	**%Persistence**
SER11	N	G8	O4'	94.141
SER65	OG	A2	O2P	90.081
C1	N4	LYS62	O	79.142
ARG52	NH2	C10	O2P	78.582
ASN8	ND2	U9	O1P	77.602
ARG55	NH2	U9	O1P	68.813
ALA15	N	G8	O6	59.944
ARG137	NH2	U4	O2P	45.035
ARG52	NH2	A11	O2P	42.596
ASN8	N	U9	O1P	39.386

A6	N6	GLU134	OE1	39.266
ARG52	NE	C10	O2P	38.106
ARG55	NE	C10	O1P	37.796
SER65	OG	C1	O5'	35.796
GLY138	N	G5	O1P	35.566
G8	O2'	ASN7	OD1	34.527
C7	N4	GLU134	OE2	33.887
ARG137	NE	G5	O2P	33.797
ARG137	NH2	C3	O1P	32.777
LYS62	NZ	G12	O6	30.677
ARG137	N	G5	O1P	30.557
ARG67	NH2	U4	O4	29.047
ARG137	NE	U4	O2P	24.238
LYS60	NZ	G12	O1P	23.598
ARG52	NE	U9	O2P	23.488
ARG137	NH2	G5	O2P	21.958
LYS62	NZ	U13	O4	20.248
LYS62	NZ	G12	N7	20.148
ARG52	NH2	U9	O5'	17.938
ARG52	NH1	A11	O2P	17.488
ARG137	NH1	C3	O1P	16.348
ASN8	N	G8	O3'	16.258
LYS60	NZ	G12	O2P	15.518
TYR132	OH	C3	O2P	15.328
HIS19	NE2	C3	O1P	15.208
ARG137	NH1	U4	O2P	14.689
C1	N4	ASP63	O	14.029
SER136	OG	G5	O1P	13.599
G8	O5'	ASN8	O	13.299
LYS60	NZ	U13	O2P	13.269
ARG52	NH2	C10	O1P	13.039
LYS62	NZ	G12	O2P	13.009
ARG137	N	G5	O2P	12.949
ARG52	NH2	U9	O2P	12.559
A6	N6	GLU134	OE2	12.129
SER136	OG	G5	O2P	10.989
GLY20	N	A2	O1P	10.769
ARG55	NH1	U9	O1P	10.259

Table S39. Protein-RNA hydrogen bonds with percentage of persistence higher than 10% for run 14 of the N-NTD:dsNS complex.

Donor		**Acceptor**		
Amino acid residue	**Atom**	**Nucleotide residue**	**Atom**	**%Persistence**
C1	N4	LYS62	O	85.271
THR51	OG1	U9	O1P	65.843
TYR132	OH	A2	O1P	61.974
ARG67	NH2	A2	O2P	61.804
GLY57	N	G12	O2P	56.314

ARG137	NH1	G5	O2P	46.915
ARG137	NH2	G5	O2P	46.875
LYS62	NZ	U13	O4	44.666
ARG48	NH1	G8	O5'	34.477
THR51	N	U9	O2P	33.817
ARG137	NH1	U4	O2P	32.597
ARG55	NH2	C10	O1P	31.437
ARG48	NH1	U9	O1P	31.087
THR51	N	U9	O1P	30.937
ARG55	NH1	C10	O2P	29.287
ARG52	NH2	A11	O2P	27.697
ARG52	NE	C10	O2P	27.427
ASN8	ND2	C7	O2'	26.007
ARG52	NH2	C10	O1P	25.537
ARG137	NH2	U4	O2P	23.198
ARG52	NH2	C10	O2P	22.958
LYS62	NZ	G12	O6	22.758
ARG52	NE	C10	O1P	22.028
ARG52	NH1	C10	O1P	21.588
ARG48	NH2	U9	O1P	20.328
LYS62	NZ	G12	N7	17.198
HIS19	NE2	A2	O1P	16.858
ARG52	NH2	C10	O5'	16.528
G8	N2	ASN8	O	16.348
C7	O2'	ASN8	OD1	14.249
GLY1	N	A6	N3	13.079
GLY139	N	A6	O2P	13.069
C7	O3'	ALA2	O	12.889

Table S40. Protein-RNA hydrogen bonds with percentage of persistence higher than 10% for run 15 of the N-NTD:dsNS complex.

Donor		**Acceptor**		
Amino acid Residue	**Atom**	**Nucleotide residue**	**Atom**	**%Persistence**
ARG52	NH1	U9	O2P	91.581
ARG52	NH1	U9	O2P	91.581
C7	O2'	ALA116	O	91.461
C7	O2'	ALA116	O	91.461
ARG52	NH2	C10	O2P	89.651
ARG52	NH2	C10	O2P	89.651
ASN8	ND2	U9	O1P	88.301
ASN8	ND2	U9	O1P	88.301
ARG53	N	U9	O2P	82.602
ARG53	N	U9	O2P	82.602
ARG52	NH1	C10	O2P	80.812
ARG52	NH1	C10	O2P	80.812
G8	O2'	ASN8	OD1	60.344
G8	O2'	ASN8	OD1	60.344
ALA116	N	C7	O2	54.385

ALA116	N	C7	O2	54.385
ARG137	NH2	A6	O2P	50.195
ARG137	NH2	A6	O2P	50.195
GLY56	N	C10	O1P	45.425
GLY56	N	C10	O1P	45.425
ARG55	NH2	G12	O2P	43.026
ARG55	NH2	G12	O2P	43.026
ARG55	NE	A11	O2P	39.736
ARG55	NE	A11	O2P	39.736
ARG53	NH1	U9	O1P	37.546
ARG53	NH1	U9	O1P	37.546
C1	O5'	GLN18	O	34.197
C1	O5'	GLN18	O	34.197
ARG53	NE	U9	O1P	33.367
ARG53	NE	U9	O1P	33.367
ARG55	NH2	A11	O2P	30.387
ARG55	NH2	A11	O2P	30.387
ARG109	NH2	G8	N3	29.577
ARG109	NH2	G8	N3	29.577
SER65	OG	A2	O1P	27.427
SER65	OG	A2	O1P	27.427
ARG137	NE	A6	O2P	26.677
ARG137	NE	A6	O2P	26.677
GLY57	N	C10	O1P	26.017
GLY57	N	C10	O1P	26.017
ARG137	NH2	G5	O1P	24.388
ARG137	NH2	G5	O1P	24.388
GLY4	N	U9	O2'	22.428
GLY4	N	U9	O2'	22.428
ARG67	NH2	C3	O2P	18.848
ARG67	NH2	C3	O2P	18.848
ARG55	NH1	A11	O2P	18.828
ARG55	NH1	A11	O2P	18.828
GLY20	N	C1	O4'	18.308
GLY20	N	C1	O4'	18.308
ARG137	NH1	A6	O2P	18.048
ARG137	NH1	A6	O2P	18.048
ARG55	NH1	G12	O2P	17.798
ARG55	NH1	G12	O2P	17.798
ARG53	NH2	U9	O1P	17.678
ARG53	NH2	U9	O1P	17.678
ARG67	NH2	A2	O2P	16.618
ARG67	NH2	A2	O2P	16.618
ALA116	N	G8	N2	16.078
ALA116	N	G8	N2	16.078
ARG55	NH2	A11	O1P	15.898
ARG55	NH2	A11	O1P	15.898
SER65	OG	A2	O2P	15.688
SER65	OG	A2	O2P	15.688
ARG53	NH2	G8	O3'	15.648
ARG53	NH2	G8	O3'	15.648

ARG67	NE	A2	O2P	14.859
ARG67	NE	A2	O2P	14.859
G8	O5'	THR51	O	13.269
G8	O5'	THR51	O	13.269
SER65	N	C1	O4'	13.249
SER65	N	C1	O4'	13.249
ARG137	NH1	G5	O2P	12.739
ARG137	NH1	G5	O2P	12.739
MET3	N	U9	O2'	11.389
MET3	N	U9	O2'	11.389
LYS62	NZ	G14	O6	11.079
LYS62	NZ	G14	O6	11.079
ARG55	NH2	A11	O5'	10.919
ARG55	NH2	A11	O5'	10.919
SER65	N	A2	O2P	10.809
SER65	N	A2	O2P	10.809
LYS21	NZ	C1	N3	10.759
LYS21	NZ	C1	N3	10.759
GLY1	N	A11	O1P	10.669
GLY1	N	A11	O1P	10.669

Table S41. Protein-RNA hydrogen bonds with percentage of persistence higher than 10% for run 16 of the N-NTD:dsNS complex.

Donor		**Acceptor**		
Amino acid residue	**Atom**	**Nucleotide residue**	**Atom**	**%Persistence**
SER11	N	G8	O4'	81.732
ARG53	NH2	C10	O2P	54.775
ARG137	NH1	U4	O2P	53.725
ARG53	NH2	U9	O1P	49.395
SER65	N	C1	O5'	47.995
ARG137	NH2	C3	O1P	40.626
C7	N4	SER140	OC1	36.076
ARG137	NH1	C3	O5'	33.497
ARG137	NH2	C3	O2P	32.997
ARG55	NH2	G12	O2P	29.737
ASP58	N	G14	N7	28.777
ARG137	NH2	U4	O2P	28.397
C1	N4	LYS62	O	26.667
ARG137	NH1	C3	O1P	26.637
SER11	OG	G8	O5'	26.347
SER140	OG	C7	N4	25.727
A6	N6	SER140	OC2	24.278
ARG52	NH1	G12	O6	23.868
ARG55	NH2	U13	O2P	22.728
ARG52	NH2	G12	N7	22.538
GLY57	N	U13	O4	22.468
LYS60	NZ	U13	O2P	22.428
ARG53	NH1	C10	O2P	21.958

ARG52	NH2	C10	O2P	21.528
ARG137	NH1	C3	O2P	21.158
ARG109	NH1	G8	N3	20.918
ARG55	NE	G12	O2P	20.818
LYS60	NZ	G12	O1P	19.168
ARG137	NE	U4	O2P	17.498
ARG53	NH1	U9	O1P	15.188
GLY57	N	A11	O1P	15.018
MET3	N	C10	O1P	14.939
SER65	OG	A2	O2P	13.849
C7	O3'	ASN113	O	13.759
ARG53	NE	C10	O2P	13.439
ARG55	NH2	G12	O5'	12.899
LYS62	NZ	G12	N7	11.509
LYS62	NZ	G12	O6	10.489
ARG52	NH1	C10	O2P	10.319
G14	O2'	ASP58	OD2	10.129

Table S42. Protein-RNA hydrogen bonds with percentage of persistence higher than 10% for run 17 of the N-NTD:dsNS complex.

Donor		**Acceptor**		
Amino acid residue	**Atom**	**Nucleotide residue**	**Atom**	**%Persistence**
G8	N2	PRO111	O	97.34
SER65	OG	A2	O2P	82.622
ARG137	NH1	U4	O2P	79.712
ARG109	NH1	G8	N3	78.762
ARG52	NH2	C10	O2P	77.772
SER11	N	G8	O4'	65.673
ASN8	ND2	U9	O1P	65.143
SER65	OG	C1	O5'	63.294
C1	N4	LYS62	O	60.894
GLY57	N	G12	O2P	60.054
ARG52	NH1	C10	O2P	55.254
ARG109	NH2	G8	N2	54.205
LYS62	NZ	G12	O6	51.615
ARG137	NH2	C3	O1P	46.275
ARG52	NH2	U9	O1P	46.015
ARG137	NH1	C3	O5'	45.555
C7	O2'	ALA112	O	44.966
ARG137	NH2	C3	O2P	40.306
G8	O2'	ASN8	OD1	36.596
HIS19	NE2	C3	O2P	30.307
ARG137	NH1	C3	O2P	29.527
ARG137	NH1	C3	O1P	28.217
ARG52	NH2	U9	O2P	26.247
C1	N4	ASP63	O	25.577
ARG109	NH2	G8	N3	25.277
ARG55	NH1	A11	O2P	22.828

ARG55	NH2	C10	O1P	22.258
TYR71	OH	G8	O5'	21.258
LYS62	NZ	G12	N7	19.948
ARG52	NE	U9	O1P	18.228
ARG55	NH1	C10	O1P	15.788
SER11	N	G8	O5'	14.829
TYR69	OH	U9	O2P	14.709
ARG55	NH1	C10	O5'	14.509
SER140	N	G5	O1P	13.659
ARG52	NH1	U9	O2P	12.209
HIS19	NE2	A2	O3'	11.559
SER140	OG	G5	O1P	10.809
LYS62	NZ	U13	O4	10.629

Table S43. Protein-RNA hydrogen bonds with percentage of persistence higher than 10% for run 18 of the N-NTD:dsNS complex.

Donor		**Acceptor**		
Amino acid residue	**Atom**	**Nucleotide residue**	**Atom**	**%Persistence**
ARG52	NE	C10	O2P	78.612
ARG52	NH2	A11	O2P	76.252
SER65	OG	A2	O2P	76.152
TYR132	OH	C3	O2P	73.163
SER11	N	G8	O4'	66.063
ARG109	NH2	G8	N3	55.014
G8	N2	PRO111	O	53.575
ARG52	NH2	C10	O2P	44.926
G8	N2	ALA112	O	41.006
C1	N4	LYS62	O	38.826
ARG137	NE	A6	O2P	38.556
ARG67	NH1	A2	O2P	35.286
ARG137	NH1	G5	O2P	31.697
C1	N4	ASP63	O	31.647
ASN113	ND2	U9	O2	30.457
A6	N6	GLU134	OE1	28.527
C7	O2'	ALA112	O	24.938
ARG67	NH2	A2	O2P	23.898
ARG137	NH2	A6	O2P	21.548
LYS62	NZ	G12	O6	21.368
GLY57	N	A11	O1P	20.888
HIS19	NE2	C3	O2P	19.948
LYS62	NZ	G12	N7	18.438
ARG52	NH1	A11	O2P	17.968
LYS60	NZ	G12	O2P	17.888
ARG109	NH1	G8	N2	16.308
LYS62	NZ	U13	O4	16.128
SER65	OG	C1	O5'	15.988
ARG52	NH2	C10	O5'	15.678
SER140	OG	C3	O1P	15.318

C7	O2'	ASN113	O	14.229
C7	O3'	ASN113	O	13.809
A6	N6	GLU134	OE2	13.059
ARG53	N	U9	O1P	11.899
TYR71	OH	G8	O5'	11.769
ARG137	NH2	G5	O2P	11.299
ARG137	NH1	G5	O1P	10.919
ARG53	NE	U9	O1P	10.879
SER11	OG	G8	O5'	10.859
GLY138	N	G5	O1P	10.359

Table S44. Protein-RNA hydrogen bonds with percentage of persistence higher than 10% for run 19 of the N-NTD:dsNS complex.

Donor		**Acceptor**		
Amino acid residue	**Atom**	**Nucleotide residue**	**Atom**	**%Persistence**
TYR132	OH	A2	O1P	76.752
C1	O5'	GLU134	OE2	72.473
ARG52	NH1	C10	O2P	53.155
ARG52	NH2	A11	O2P	51.675
TYR69	OH	U9	O2P	50.255
ARG137	NH1	G5	O6	48.125
GLY4	N	C7	O2'	44.836
ARG137	NH2	G5	N7	39.486
ARG52	NH1	A11	O2P	38.716
GLY135	N	A2	O1P	35.696
THR51	N	U9	O1P	32.567
SER11	N	G8	O5'	30.147
LYS62	NZ	G14	O6	28.587
THR51	OG1	U9	O1P	27.747
ARG137	NH2	G5	O6	26.887
G8	N2	GLY1	O	25.927
ARG52	NH2	C10	O2P	20.238
TYR69	OH	U9	O1P	19.758
G8	N2	MET3	O	19.108
ARG52	N	U9	O1P	17.948
LYS60	NZ	G12	O2P	17.948
ARG52	NH2	C10	O1P	17.498
TYR71	OH	G8	O5'	17.138
ARG52	NE	C10	O2P	16.828
ARG52	NH1	U9	O1P	15.878
ARG55	NH1	G12	O2P	15.438
ARG109	NH2	G8	N7	14.989
G8	N2	ALA2	O	14.899
ARG67	NH1	U9	O2P	14.739
ARG137	NE	G5	O2P	13.109
C1	N4	LYS62	O	12.789
ASN8	ND2	G8	N3	12.689
TYR132	OH	A2	O2P	12.689

GLY4	N	C7	O2	12.619
MET3	N	U9	O2'	12.009
SER11	N	G8	O4'	11.649
ARG137	NH2	U9	O4	11.589
ARG52	NH2	C10	O5'	10.949
ARG52	NH1	C10	O1P	10.919
LYS60	NZ	G12	O1P	10.479
ARG137	NH1	U4	O4	10.409
ARG55	NH2	G12	O2P	10.379
ALA2	N	U9	O2'	10.339
ARG55	NH2	U13	O2P	10.089

Table S45. Protein-RNA hydrogen bonds with percentage of persistence higher than 10% for run 20 of the N-NTD:dsNS complex.

Donor		**Acceptor**		
Amino acid residue	**Atom**	**Nucleotide residue**	**Atom**	**%Persistence**
ARG52	NH2	C10	O1P	88.831
SER65	OG	A2	O2P	81.802
ARG52	NE	C10	O2P	78.032
ARG55	NH1	A11	O2P	66.743
G8	N2	ALA112	O	63.204
ARG55	NH1	C10	O1P	57.404
ASN113	ND2	C10	O4'	55.464
C1	N4	ASP63	O	55.424
ASN113	ND2	U9	O2	54.895
ASN8	ND2	U9	O1P	54.775
ARG55	NH2	A11	O1P	54.015
ALA115	N	C7	O2'	50.875
ARG67	NE	A2	O2P	49.375
SER11	N	G8	O4'	47.975
ARG67	NH2	C3	O2P	46.015
ARG67	NH2	A2	O5'	36.316
ARG67	NH2	A2	O2P	35.066
LYS60	NZ	G12	O2P	33.277
LYS62	NZ	G12	O6	32.757
C1	N4	LYS62	O	31.927
ARG55	NH2	A11	O2P	31.167
LYS62	NZ	G12	N7	31.117
C7	O3'	ASN113	O	29.147
ARG52	NH1	U9	O1P	26.737
SER65	OG	C1	O5'	25.917
SER11	N	G8	O5'	24.298
G8	O2'	ASN8	OD1	21.378
ARG55	NH2	C10	O1P	17.498
ARG109	NH2	G8	N3	16.208
THR17	OG1	A2	O1P	15.918
LYS60	NZ	G12	O1P	15.218
ARG55	NH1	A11	O1P	12.719

LYS60	NZ	U13	O2P	11.939
ASN114	N	G8	N2	11.179
U9	O2'	ASN113	OD1	10.729
TYR71	OH	G8	O5'	10.349

Table S46. Protein-RNA hydrogen bonds with percentage of persistence higher than 10% for run 21 of the N-NTD:dsNS complex.

Donor		Acceptor		
Amino acid residue	**Atom**	**Nucleotide residue**	**Atom**	**%Persistence**
GLY4	N	U9	O2'	64.064
C1	O5'	GLU134	OE1	55.134
ARG52	NH2	G12	N7	54.915
ARG52	NH1	G12	O6	54.275
ARG109	NH2	G8	O2'	39.316
ARG109	NH1	G8	O2'	38.976
ARG53	NH2	A11	O2P	34.387
ARG53	NH2	C10	O1P	33.097
ARG109	NH2	G8	O3'	32.647
C1	O5'	GLU134	OE2	32.137
ARG137	NH1	A2	O1P	31.657
C10	O2'	GLY1	O	29.727
ARG137	NH1	C3	O2P	29.297
LYS62	NZ	G14	N7	28.667
ASN8	ND2	C10	O1P	28.547
ARG109	NH2	U9	O1P	28.547
ARG67	NH2	C1	O5'	25.867
ARG55	NH2	G12	O1P	21.828
ALA116	N	G8	O5'	21.818
ARG55	NH1	U13	O2P	20.368
ARG109	NH1	G8	O3'	19.888
ARG137	NH2	C3	O2P	19.288
ARG67	NH2	C1	O4'	19.028
G8	O2'	PRO111	O	18.628
ARG55	NH1	G12	O5'	15.438
GLY1	N	A11	O1P	14.509
ARG53	NH1	C10	O1P	13.299
ARG137	NH2	C3	O1P	12.809
ALA116	N	G8	O4'	12.619
ASN8	ND2	U9	O3'	12.349
ARG53	NE	A11	O1P	11.749
ARG52	NH2	G12	O6	11.469
ARG55	NH1	G12	O1P	11.319

Table S47. Protein-RNA hydrogen bonds with percentage of persistence higher than 10% for run 22 of the N-NTD:dsNS complex.

Donor		Acceptor		
Amino acid residue	**Atom**	**Nucleotide residue**	**Atom**	**%Persistence**
SER11	N	G8	O4'	95.21
ARG137	NH1	C3	O2P	89.761
G8	N2	PRO111	O	72.873
ARG52	NH1	C10	O2P	69.073
C1	N4	LYS62	O	68.413
ARG52	NH2	C10	O2P	65.023
ASN8	ND2	U9	O1P	62.944
ALA116	N	G8	O6	55.934
ARG137	NH2	A2	O1P	48.615
ARG137	NH1	A2	O1P	44.976
ARG52	NH2	U9	O1P	41.226
LYS60	NZ	A11	O1P	33.247
ARG67	NH2	A2	O2P	31.587
ARG137	NH1	A2	O5'	30.007
G8	O2'	PRO111	O	29.657
ARG137	NH2	A2	O2P	28.747
LYS62	NZ	G12	O6	27.487
LYS60	NZ	A11	O2P	24.818
LYS62	NZ	U13	O4	23.478
GLY139	N	G5	O2P	23.418
C1	O5'	ASP63	O	22.408
SER65	N	C1	O5'	19.758
LYS62	NZ	G12	N7	17.238
ALA115	N	C7	O2'	15.408
C7	O3'	ASN113	O	15.118
ASN114	N	G8	N2	14.609
C7	O2'	ASN113	O	14.409
ASN8	ND2	G8	O3'	13.799
GLY1	N	C10	O1P	11.769
GLY139	N	U4	O1P	11.409
ASN8	ND2	G8	O5'	11.079
ARG137	NH1	A2	O2P	10.899
GLY138	N	U4	O2P	10.219

Table S48. Protein-RNA hydrogen bonds with percentage of persistence higher than 10% for run 23 of the N-NTD:dsNS complex.

Donor		Acceptor		
Amino acid residue	**Atom**	**Nucleotide residue**	**Atom**	**%Persistence**
G8	N2	ASN8	OD1	75.812
C10	N4	TYR69	OH	75.362
TYR69	OH	U9	O2P	71.933
ARG52	NH2	A11	O1P	71.273

GLY4	N	U9	O2	67.373
ARG137	NH2	G5	O2P	59.624
TYR71	OH	G8	O5'	53.325
GLY138	N	C3	O2P	51.675
SER11	N	G8	N7	47.645
ARG48	NH1	G8	O5'	47.445
ARG137	NE	U4	O2P	45.095
LYS60	NZ	G12	O2P	42.006
U9	O2'	ALA2	O	39.826
ARG137	NE	G5	O2P	38.326
C7	O2'	GLY4	O	35.136
C1	O5'	GLY130	O	26.087
ARG55	NH2	C10	O1P	23.328
ARG52	NH1	C10	O1P	22.938
ARG137	NH2	U4	O2P	22.538
ARG52	NE	A11	O1P	20.118
GLY139	N	A2	O1P	19.608
ARG109	NH2	G8	O6	19.448
GLY138	N	U4	O2P	19.388
ARG52	NE	A11	O2P	19.048
ARG53	N	C10	O2P	18.818
LYS60	NZ	A11	O1P	17.508
ARG52	NH1	A11	O2P	17.038
ARG109	NH2	C7	N4	16.718
ARG53	NE	C10	O1P	15.108
GLY138	N	U4	O1P	13.869
ARG55	NH1	C10	O1P	13.409
LYS60	NZ	G12	O1P	12.189
C1	O5'	PHE131	O	11.189
SER140	OG	A2	O1P	10.789
SER140	N	A2	O1P	10.669
ARG53	NE	U9	O1P	10.569
ARG53	NH2	U9	O1P	10.129

Table S49. Protein-RNA hydrogen bonds with percentage of persistence higher than 10% for run 24 of the N-NTD:dsNS complex.

Donor		**Acceptor**		
Amino acid residue	**Atom**	**Nucleotide residue**	**Atom**	**%Persistence**
C1	N4	LYS62	O	92.081
ARG67	NH2	A2	O2P	85.931
ARG48	NH1	U9	O2P	80.262
TYR71	OH	G8	O5'	70.093
ARG67	NH1	A2	O2P	63.084
SER65	N	C1	O5'	62.294
ARG52	NH2	A11	O2P	58.334
LYS62	NZ	G12	N7	44.626
ARG52	NH1	A11	O2P	42.696
LYS62	NZ	G12	O6	40.986

LYS60	NZ	G12	O1P	40.606
ARG52	NH1	C10	O2P	27.947
C7	O3'	LEU5	O	26.477
LYS60	NZ	U13	O2P	25.807
LEU5	N	C7	O1P	24.118
ARG52	NH1	C10	O1P	23.208
LYS62	NZ	U13	O4	22.538
ARG48	NH2	U9	O1P	21.428
ARG137	NH1	C3	O1P	21.408
SER11	N	G8	N7	20.958
TYR69	OH	U9	O4	19.518
ARG137	NH1	U4	O2P	19.388
ARG137	NH2	C3	O1P	18.128
ARG52	NH2	A11	N7	17.498
ARG137	NH2	U4	O2P	15.308
ASN8	ND2	G8	O2'	15.058
LYS60	NZ	G12	O2P	14.219
ARG52	NH2	A11	O1P	12.489
ARG137	NE	C3	O1P	11.559
ARG137	NH2	C3	O2P	10.329
LEU5	N	C7	O3'	10.239

Table S50. Protein-RNA hydrogen bonds with percentage of persistence higher than 10% for run 25 of the N-NTD:dsNS complex.

Donor		**Acceptor**		
Amino acid residue	**Atom**	**Nucleotide residue**	**Atom**	**%Persistence**
ARG137	NH2	C3	O1P	62.784
G8	N2	PRO111	O	56.434
ARG137	NH2	U4	O2P	55.394
ARG109	NH2	G8	N3	47.505
ASN8	ND2	U9	O1P	46.525
ARG137	NH1	C3	O1P	46.165
SER65	OG	A2	O2P	45.435
ARG52	NH1	U9	O2P	45.155
ARG67	NH2	A2	O2P	34.107
C1	N4	MET61	O	33.597
ARG52	NH1	C10	O2P	33.027
ARG137	NH1	U4	O2P	30.437
C7	O2'	ALA112	O	30.327
LYS62	NZ	G12	O6	25.967
ARG52	NH2	C10	O2P	25.237
ARG109	NH1	G8	N2	24.838
C1	N4	LYS62	O	24.578
ARG52	NH1	U9	O1P	24.388
TYR69	OH	G8	O6	24.098
ARG137	NE	U4	O1P	23.738
ARG52	NH2	C10	O1P	23.168
SER65	OG	A2	O1P	22.858

SER65	N	A2	O2P	21.338
LYS60	NZ	G12	O2P	20.268
C7	O2'	PRO111	O	19.308
C1	N4	ASP63	O	19.068
U9	O2'	GLY1	O	18.958
ARG67	NH1	A2	O2P	18.708
ARG52	NE	C10	O2P	18.658
LYS62	NZ	G12	N7	18.168
ARG137	NE	U4	O2P	18.018
C1	O5'	ASP63	O	17.768
SER11	N	G8	O4'	16.948
GLY1	N	C10	O1P	16.118
G8	O2'	ASN8	OD1	15.058
GLY57	N	A11	O2P	14.589
ARG67	NH2	A2	O1P	14.099
SER140	N	G5	O1P	13.819
LYS60	NZ	U13	O2P	13.209
SER65	OG	C1	O5'	12.529
LYS60	NZ	G14	N7	12.159
ARG137	NH1	C3	O5'	11.939
TYR69	OH	G8	N7	10.979
ARG67	NE	A2	O2P	10.179

REFERENCES

1. Bunker, D.L., B. Garrett, T. Kleindienst, and G.S. Long. 1974. Discrete simulation methods in combustion kinetics. *Combust. Flame*. 23:373–379.
2. Gillespie, D.T. 1976. A general method for numerically simulating the stochastic time evolution of coupled chemical reactions. *J. Comput. Phys.* 22:403–434.
3. Grossoehme, N.E., L. Li, S.C. Keane, P. Liu, C.E. Dann, J.L. Leibowitz, and D.P. Giedroc. 2009. Coronavirus N Protein N-Terminal Domain (NTD) Specifically Binds the Transcriptional Regulatory Sequence (TRS) and Melts TRS-cTRS RNA Duplexes. *J. Mol. Biol.* 394:544–557.
4. Keane, S.C., P. Lius, J.L. Leibowitzs, and D.P. Giedroc. 2012. Functional Transcriptional Regulatory Sequence (TRS) RNA binding and helix destabilizing determinants of Murine Hepatitis Virus (MHV) Nucleocapsid (N) protein. *J. Biol.*

Chem. 287:7063–7073.

5. Larkin, M.A., G. Blackshields, N.P. Brown, R. Chenna, P.A. Mcgettigan, H. McWilliam, F. Valentin, I.M. Wallace, A. Wilm, R. Lopez, J.D. Thompson, T.J. Gibson, and D.G. Higgins. 2007. Clustal W and Clustal X version 2.0. *Bioinformatics*. 23:2947–2948.
6. Baker, N.A., D. Sept, S. Joseph, M.J. Holst, and J.A. McCammon. 2001. Electrostatics of nanosystems: Application to microtubules and the ribosome. *Proc. Natl. Acad. Sci. U. S. A.* 98:10037–10041.
7. Dolinsky, T.J., P. Czodrowski, H. Li, J.E. Nielsen, J.H. Jensen, G. Klebe, and N.A. Baker. 2007. PDB2PQR: expanding and upgrading automated preparation of biomolecular structures for molecular simulations. *Nucleic Acids Res.* 35:W522-5.
8. Olsson, M.H.M., C.R. SØndergaard, M. Rostkowski, and J.H. Jensen. 2011. PROPKA3: Consistent treatment of internal and surface residues in empirical p K a predictions. *J. Chem. Theory Comput.* 7:525–537.
9. Delano, W.L. 2002. The PyMOL Molecular Graphics System. DeLano Scientific, San Carlos, CA, USA. .